Nuclear Magnetic Resonance Studies of the Rare-Earth Nickel Oxide Perovskites

DISS. ETH NO. 26170

Nuclear Magnetic Resonance Studies of the Rare-Earth Nickel Oxide Perovskites

A thesis submitted to attain the degree of
DOCTOR OF SCIENCES of ETH ZURICH
(Dr. sc. ETH Zurich)

presented by

LUKAS ALEXANDER KOROSEC

MSc ETH Physics, ETH Zürich

born on 20.03.1993

citizen of
Austria

accepted on the recommendation of

Prof. Dr. J. F. Mesot, examiner
Prof. em. Dr. H.-R. Ott, co-examiner
Prof. Dr. J.-M. Triscone, co-examiner

2019

Abstract

The rare-earth nickel oxide perovskites $RE\mathrm{NiO_3}$ are a well-known family of materials with strong electronic correlations. While $\mathrm{LaNiO_3}$ is a paramagnetic metal down to at least liquid helium temperatures, all other stoichiometric compounds in this class show a metal–insulator transition (MIT) at a composition-dependent temperature T_{MI} between 0 and 600 K. Within the insulating phase, antiferromagnetic order occurs below the Néel temperature $T_\mathrm{N} \approx 130 - 221\,\mathrm{K}$. Both T_{MI} and T_N depend continuously on the radius of the RE^{3+} ion.

This thesis discusses a series of experiments using local-probe techniques, mainly nuclear magnetic resonance (NMR) but also muon spin rotation (μSR) and nuclear quadrupolar resonance (NQR), performed in different regions of the temperature–composition phase diagram of $RE\mathrm{NiO_3}$.

In chapter 1, a brief introduction places this thesis in the context of the physics of materials with strongly correlated electrons. An introduction to the experimental techniques is given in chapter 2. The physical properties of $RE\mathrm{NiO_3}$ are shortly reviewed in chapter 3.

Chapter 4 contains a mathematical discussion of the relaxation of nuclear spins greater than 1/2 in systems which are relevant to solid state physics. After some known formulae are re-derived, new results, such as a functional form for longitudinal relaxation in antiferromagnetically ordered powders, are obtained. These theoretical results will be used for data analysis in the subsequent chapters.

A series of ^{17}O-NMR experiments in ten different $RE\mathrm{NiO_3}$ materials is presented in chapter 5. The variation of the electric field gradient at the ^{17}O nucleus across the $RE\mathrm{NiO_3}$ series is shown to be likely inconsistent with complete charge disproportionation ($2\,\mathrm{Ni^{3+}} \longrightarrow \mathrm{Ni^{2+}} + \mathrm{Ni^{4+}}$). Temperature-dependent experiments in $\mathrm{LaNiO_3}$ from room temperature down to 5 K show paramagnetic Fermi liquid behaviour, thus disproving a recent controversial claim of antiferromagnetic order in this material. Measurements in $\mathrm{YNiO_3}$ reveal a gapped magnetic excitation spectrum in the antiferromagnetic phase. In $\mathrm{SmNiO_3}$, variable-temperature experiments were performed both below and above room temperature, in order to access both T_N and T_{MI}. Here, the relaxation behaviour above T_{MI} is inconsistent with a Fermi liquid picture, and instead seems to imply the presence of localised spins in

the NiO_6 octahedra. No maximum of the NMR relaxation rate T_1^{-1} is found at T_{MI}, ruling out that the MIT is driven by magnetic fluctuations. Instead, T_1^{-1} is enhanced only below T_{MI}, demonstrating that the insulating phase is required by the magnetic fluctuations which cause the antiferromagnetic transition at lower temperature. Finally, $PrNiO_3$ is studied as an example for a system with $T_N = T_{MI}$. Also here, the magnetic fluctuations do not peak at the phase transition, which rules out its description as a spin-density wave transition.

In chapter 6, ^{205}Tl- and ^{203}Tl-NMR as well as μSR measurements in $TlNiO_3$ are described. This compound is closely related to the rare-earth nickelates. Here, in addition to the known transition at T_N, a second magnetic phase transition was discovered.

First experiments on ^{175}Lu-NQR in $LuNiO_3$ are described in chapter 7. The data seem to indicate the presence of two slightly inequivalent sites of Lu, however this interpretation is highly speculative. If the speculation is correct, this would imply that all crystallographic studies published thus far have missed a very weak distortion of the lattice. Unfortunately, no high-quality sample of $LuNiO_3$ has become available by the end of this thesis project, and future measurements on a higher-purity sample will be required to test the suggested interpretation.

Zusammenfassung

Die Seltenerd-Nickel-Oxid Perowskite $RE\mathrm{NiO_3}$ sind eine bekannte Reihe von Materialien mit starken elektronischen Korrelationen. Während $\mathrm{LaNiO_3}$ mindestens bis zur Temperatur von flüssigem Helium ein paramagnetisches Metall bleibt, haben sämtliche anderen stöchiometrischen $RE\mathrm{NiO_3}$ Verbindungen einen Metall–Isolator Phasenübergang bei einer Temperatur T_{MI} zwischen 0 und 600 K, deren Wert von der Zusammensetzung abhängt. Innerhalb der isolierenden Phase tritt antiferromagnetische Ordnung unterhalb der Néel-Temperatur $T_\mathrm{N} \approx 130 - 221\,\mathrm{K}$ auf. Sowohl T_{MI} als auch T_N hängen stetig vom Radius des RE^{3+}-Ions ab.

Diese Dissertation beschreibt eine Reihe von Experimenten basierend auf lokalen Techniken, hauptsächlich Kernmagnetresonanz (NMR), aber auch Myonenspin-Rotation (μSR) und Kernquadrupolresonanz (NQR), welche in verschiedenen Bereichen des Phasendiagramms von $RE\mathrm{NiO_3}$ durchgeführt wurden.

Eine kurze Einleitung in Kapitel 1 setzt diese Arbeit in den Kontext der Physik von Materialien mit stark korrelierten Elektronen. Kapitel 2 enthält eine Einführung zu den relevanten experimentellen Techniken. Die physikalischen Eigenschaften von $RE\mathrm{NiO_3}$ werden in Kapitel 3 kurz beschrieben.

Kapitel 4 präsentiert eine mathematische Diskussion der Relaxation von Kernspins grösser als 1/2 in Systemen, welche für die Festkörperphysik relevant sind. Nachdem einige bereits bekannte Formeln neu hergeleitet werden, werden neue theoretische Resultate präsentiert, beispielsweise zur longitudinalen Relaxation in antiferromagnetischen Pulvern. Diese werden in den späteren Kapiteln zur Analyse von experimentellen Daten benutzt.

Eine Serie von ^{17}O-NMR Experimenten an zehn verschiedenen $RE\mathrm{NiO_3}$ Materialien wird in Kapitel 5 diskutiert. Es wird gezeigt, dass die Variation des elektrischen Feldgradienten an der Lage des ^{17}O-Atomkerns über die $RE\mathrm{NiO_3}$ Reihe hinweg inkonsistent scheint mit der Vorhersage von kompletter Ladungsdisproportionierung der Nickel-Ionen in der isolierenden Phase. Temperaturabhängige Experimente an $\mathrm{LaNiO_3}$ zwischen Raumtemperatur und 5 K zeigen dass dieses Material durch eine paramagnetische Fermiflüssigkeit beschrieben werden kann. Dies widerlegt die kürzlich publizierte kontroverse Behauptung, dass $\mathrm{LaNiO_3}$ antiferromagnetisch ordne. Bei Messungen an $\mathrm{YNiO_3}$ wurde eine Bandlücke im magnetischen Anregungs-

spektrum in der antiferromagnetischen Phase gefunden. In $SmNiO_3$ wurden Untersuchungen sowohl unterhalb als auch oberhalb von Raumtemperatur durchgeführt, wobei sowohl über T_N als auch T_{MI} hinweg gemessen wurde. Die Relaxation oberhalb von T_{MI} ist nicht vereinbar mit dem Bild einer Fermiflüssigkeit, und deutet stattdessen auf die Präsenz lokalisierter Spins in den NiO_6 Oktaedern hin. Am Metall–Isolator Phasenübergang wurde anhand der Relaxationsrate T_1^{-1} kein Maximum der magnetischen Fluktuationen gefunden. Somit kann ausgeschlossen werden dass diese den Metall–Isolator Übergang verursachen. Stattdessen nimmt T_1^{-1} erst unterhalb von T_{MI} zu, was zeigt dass die isolierende Phase eine Voraussetzung ist für die magnetischen Fluktuationen, welche bei tieferen Temperaturen zu antiferromagnetischer Ordnung führen. Schlussendlich wird $PrNiO_3$ untersucht als Beispiel für ein System mit $T_N = T_{MI}$. Auch hier wird kein Maximum der magnetischen Fluktuationen beim Phasenübergang gefunden, was dessen Beschreibung als Spindichtewellenübergang ausschliesst.

An $TlNiO_3$, welches eng verwandt ist mit $RENiO_3$, wurden sowohl ^{205}Tl- und ^{203}Tl-NMR als auch μSR Experimente durchgeführt, welche in Kapitel 6 beschrieben werden. Hier wurde zusätzlich zum bereits bekannten Übergang bei T_N ein zweiter magnetischer Phasenübergang entdeckt.

Im letzten Kapitel werden erste ^{175}Lu-NQR Messungen an $LuNiO_3$ präsentiert. Die Daten scheinen auf zwei kristallographisch leicht unterschiedliche Lu-Lagen zu deuten. Falls diese spekulative Interpretation korrekt ist, dann würde dies bedeuten, dass eine sehr schwache Verzerrung des Kristallgitters in allen bisher publizierten strukturellen Untersuchungen übersehen wurde. Die Prüfung dieser Interpretation würde hochreines $LuNiO_3$ benötigen, was bis zum Ende dieses Dissertationsprojekts leider nicht zur Verfügung stand.

Contents

Chapter 1

Introduction and Motivation

The study of strongly correlated electron behaviour and its effects on the physical properties of materials is an important branch of condensed matter physics and materials science. Some examples of interesting phenomena in materials with strongly correlated electron include:

- the "volume collapse" isostructural $\gamma \longrightarrow \alpha$ phase transition in cerium, where the volume decreases by $\sim 15\,\%$ [22, 5];
- charge carriers with huge effective masses ("heavy fermions") in intermetallic compounds of f-block elements [12], some of which are unconventional superconductors [131];
- high-temperature unconventional superconductivity in mixed copper oxides with layered perovskite structure [17] and in layered iron pnictides and chalcogenides [63, 64, 54, 123];
- the metal–insulator transitions found in various transition metal oxides [99], including the rare-earth nickel oxides [78, 90].

What all these materials have in common is that the energy scale of electron–electron interactions U is comparable to or larger than the width W of an electronic energy band at or near the Fermi energy. Bands derived from s and p atomic orbitals are typically many eV wide because their large interatomic orbital overlap causes strong hybridisation. In contrast, d and f orbitals tend to hybridise less with neighbouring atomic orbitals, leading to narrower bands. Therefore, strongly correlated electrons are found mostly in materials containing d- and f-block elements.

In many cases, the theoretical description of strongly correlated electron systems is highly challenging. Most ab-initio electronic structure calculations, e.g. those based on density functional theory (DFT) in the local density approximation, tend to fail in the case of strong electronic correlations [74].

One of the most important theoretical models of strongly correlated electron materials is the Hubbard model, which is a tight-binding model with an on-site Coulomb repulsion U [57]. In the large-U limit for a half-filled band, the model describes a magnetic insulator, i.e. a lattice of atoms carrying local magnetic moments. For $U \to 0$, it describes a simple metal. The treatment of this model becomes highly non-trivial in the intermediate case, which is relevant to strongly correlated electron materials. Modern theoretical tools such as the dynamical mean-field theory (DMFT) have led to significant progress in this direction, but are still limited by the reliance on various approximations [43]. The combination of ab-initio DFT band structure calculations with DMFT for treating strong electronic correlations has allowed for models of correlated electron systems with realistic electronic structures [74, 105].

Several important strongly correlated electron systems, e.g. the cuprate high-temperature superconductors, present the additional challenge of strong doping, i.e. non-stoichiometry. This causes chemical disorder in the material, which can be difficult to control experimentally and challenging to describe theoretically. Therefore, stoichiometric strongly correlated electron materials with a non-trivial phenomenology are the ideal "testing grounds" for theoretical models.

The rare-earth nickelate perovskites $RE\mathrm{NiO_3}$ are a well-known class of such materials [90, 25, 92, 26]. They have a metal–insulator transition (MIT) which occurs at a composition-dependent temperature $T_{MI} = 0-600\,\mathrm{K}$. Only $\mathrm{LaNiO_3}$ remains metallic at all temperatures. An antiferromagnetic phase transition occurs simultaneously with the MIT in $\mathrm{PrNiO_3}$ and $\mathrm{NdNiO_3}$ and within the insulating phase for RE=Sm–Lu and Y.

At the MIT, the crystal structure distorts slightly, such that there are two instead of one inequivalent Ni sites in the insulating phase. The experimental observation that the two sites have different Ni–O bond lengths has led to interpretations of the MIT in $RE\mathrm{NiO_3}$ in terms of charge order [87], though more recent theoretical works argue for a more subtle "site-selective Mott" transition instead [104]. Despite many speculations, the microscopic mechanism of the MIT is still unknown.

The antiferromagnetic order in $RE\mathrm{NiO_3}$ is unusual in the sense that it contains four Ni sites per period. Since the magnetic order breaks the inversion symmetry of the lattice, a ferroelectric polarisation is predicted to occur below T_N which would be strongly coupled to the magnetic order [44]. This strong coupling makes the antiferromagnetic $RE\mathrm{NiO_3}$ materials "improper ferroelectrics" [28]. Although the antiferromagnetic transition has been known for almost four decades [31], neither the exact magnetic structure nor a low-energy spin model has been agreed upon [26].

Recently, there has been experimental and theoretical progress on the rare-earth nickelates on several fronts. New theoretical tools such as the "DFT + DMFT" method allow for increasingly realistic simulations of elec-

tronic properties [104, 135]. Experimentally, it is now possible to grow epitaxial films of $RE\mathrm{NiO_3}$ on other perovskite oxides [92, 26]. While this gives access to single-crystalline systems, the properties of films depend on strain, thickness, and growth direction, which can make it difficult to extrapolate properties of the bulk material from experiments on films. Meanwhile, improved synthesis methods for polycrystalline $RE\mathrm{NiO_3}$ have yielded high quality samples, even for some small rare-earths where sample quality was a large issue in the past [42].

Nuclear magnetic resonance (NMR) uses the magnetic moment of atomic nuclei to locally probe magnetic fields in a material. Nuclei with spin $I \geq 1$ also have an electric quadrupole moment, which probes the local electric field gradient (EFG). While the NMR spectrum depends on the static magnetic field and EFG, nuclear spin relaxation measures their fluctuations. This allows NMR to address several important issues in the rare-earth nickelates. NMR relaxation measurements probe the fluctuations driving the phase transitions in the system, which can provide insight into their microscopic mechanism. Quadrupolar NMR spectra measure the static EFG, which should couple to the possible charge order in $RE\mathrm{NiO_3}$. The only previously published NMR study of any rare-earth nickelate was a temperature-dependent ^{139}La-NMR study on $\mathrm{LaNiO_3}$ [124], which is the only $RE\mathrm{NiO_3}$ material which remains a paramagnetic metal at all temperatures. Thus, after the first experiment performed as part of my Master's thesis [71], this dissertation comprises the first detailed NMR investigation of $RE\mathrm{NiO_3}$ perovskites which have both metal–insulator and magnetic phase transitions.

Chapter 4 contains a theoretical treatment of the relaxation of quadrupolar spins. All derivations are performed using the Wangsness–Bloch–Redfield theory of spin relaxation and formulated in terms of the superoperator formalism [33]. After re-deriving some known results, a novel functional form for the longitudinal relaxation of quadrupolar nuclei in an antiferromagnetic powder is discovered. The relation between the decay of the central transition NMR signal of nuclei with half-integer spin and their spin–lattice relaxation is found for the case of isotropic magnetic relaxation mechanisms. Finally, spin–lattice relaxation in nuclear quadrupole resonance is discussed briefly. Theoretical results from this chapter are applied in chapters 5 and 7.

In chapter 5, I will present ^{17}O-NMR results on ten different $RE\mathrm{NiO_3}$ materials, with particular focus on $\mathrm{LaNiO_3}$, $\mathrm{YNiO_3}$, $\mathrm{SmNiO_3}$, and $\mathrm{PrNiO_3}$. Comparing spectra from all samples shows that the EFG at the oxygen site is approximately constant across the series, which seems incompatible with a large charge disproportionation of the Ni ions. Spin–lattice relaxation measurements in all materials show that relaxation is enhanced in the paramagnetic insulating phase compared to the metallic phase. In $\mathrm{LaNiO_3}$, my NMR results show metallic Fermi liquid behaviour at all temperatures and rule out any magnetic order down to 5 K. Thermally activated relaxation

behaviour in magnetically ordered $YNiO_3$ implies that the magnetic excitation spectrum in the antiferromagnetic phase is gapped. High temperature measurements across the MIT in $SmNiO_3$ reveal that the insulating phase is prerequisite to the magnetic fluctuations causing the magnetic order. The magnetic behaviour of the metallic phase of $SmNiO_3$ is inconsistent with the Fermi liquid picture, and instead is consistent with localised magnetic moments on the Ni sublattice. Finally, measurements across the discontinuous metal-to-antiferromagnetic-insulator transition in $PrNiO_3$ show no increased relaxation at the phase transition. The results on $SmNiO_3$ and $PrNiO_3$ rule out any mechanism of the MIT which is driven by critical or nearly critical magnetic fluctuations.

In chapter 6, I discuss ^{203}Tl- and ^{205}Tl-NMR as well as muon spin spectroscopy measurements in $TlNiO_3$, a compound which is very closely related to the rare-earth nickelates [68]. While a magnetic phase transition in $TlNiO_3$ analogous to that in $RENiO_3$ was known previously [66], I have discovered a second magnetic transition in this system whose explanation is yet unclear.

Finally, chapter 7 reports first results of the nuclear quadrupole resonance (NQR) signal of ^{175}Lu in $LuNiO_3$. The experiment may point towards the presence of two very slightly different Lu ions in the paramagnetic insulating phase of $LuNiO_3$. At present, this is in contradiction to all published crystallographic data. Unfortunately, the quality of the NQR sample is not very high and no new high-quality sample has become available for this material. Therefore, the interpretation of the results in chapter 7 must be considered partially speculative.

Chapter 2

Experimental techniques

In this chapter, I will give an introductory review of the experimental techniques that are relevant to this thesis. First, I will discuss pulsed nuclear spin resonance, including both nuclear magnetic resonance (NMR) and nuclear quadrupole resonance (NQR), focussing on applications to solid-state systems with strong electronic correlations. Then, I will briefly describe muon spin rotation and relaxation (μSR).

2.1 Nuclear Spin Resonance

In the fields of NMR and NQR spectroscopy, the nuclear spin Hamiltonian is conventionally written in units of angular frequency (e.g. rad/s), i.e. energy divided by the reduced Planck constant $\hbar$ [81, 33]. Thus, for example the Schrödinger equation is written as

$$\mathcal{H} \left|\psi(t)\right\rangle = i\frac{\mathrm{d}}{\mathrm{d}t} \left|\psi(t)\right\rangle , \tag{2.1}$$

with $|\psi(t)\rangle$ the explicitly time-dependent quantum state and i the imaginary unit.

2.1.1 A single nucleus in an electromagnetic field

Nuclear magnetic dipole moment

Atomic nuclei with non-zero spin I possess a magnetic dipole moment

$$\vec{\mu} = \gamma\hbar\vec{I}, \tag{2.2}$$

where γ is the magnetogyric ratio and $\vec{I}$ is the dimensionless nuclear spin operator. Their interaction with the magnetic field $\vec{B}$ is described by the Zeeman Hamiltonian:

$$\hbar\mathcal{H}_{\mathrm{Z}} = -\vec{\mu}\cdot\vec{B} = -\gamma\hbar\vec{I}\cdot\vec{B}. \tag{2.3}$$

The magnetic field in a sample can have contributions from static and time-dependent applied fields as well as static and dynamic internal fields [81, p. 176].

Nuclear electric quadrupole moment

In addition to their magnetic dipole moment, nuclei with spin $I \geq 1$ also have an electric quadrupole moment

$$Q_{\alpha\beta} = \frac{eQ}{I(2I-1)}\big(\frac{3}{2}(I_\alpha I_\beta + I_\beta I_\alpha) - \vec{I}^2\delta_{\alpha\beta}\big), \tag{2.4}$$

where $\alpha, \beta = x, y, z$, $\delta_{\alpha\beta}$ is the Kronecker delta, e is the elementary charge, and Q is the nuclear quadrupole moment [128, p. 488ff]. The energy of an electric quadrupole moment in an electrostatic potential ϕ is given by

$$\hbar\mathcal{H}_Q = \frac{1}{6}\sum_{\alpha\beta} Q_{\alpha\beta}\frac{\partial^2\phi}{\partial r_\beta \partial r_\alpha} = -\frac{1}{6}\sum_{\alpha\beta} Q_{\alpha\beta}\frac{\partial E_\alpha}{\partial r_\beta}, \tag{2.5}$$

with $\vec{E} = -\vec{\nabla}\phi$ the electric field [59, p. 150]. Since $Q_{\alpha\beta}$ is symmetric and traceless by definition (c.f. equation 2.4), it couples only to the traceless part of the electric field gradient (EFG). The physical reason behind this is that the trace of the EFG is the divergence of the electric field, which is proportional to the local charge density (c.f. Gauß' law of electrostatics, in e.g. [59, p. 29]), which by symmetry cannot couple to a higher multipole moment at the same position. We can thus rewrite the Hamiltonian from equation 2.5 as [81, p. 614]

$$\hbar\mathcal{H}_Q = \frac{1}{6}\sum_{\alpha\beta} Q_{\alpha\beta}V_{\alpha\beta} = \frac{eQ}{2I(2I-1)}\vec{I}\cdot V\cdot\vec{I}, \tag{2.6}$$

$$V_{\alpha\beta} = \frac{\partial^2\phi}{\partial r_\beta \partial r_\alpha} - \frac{1}{3}\nabla^2\phi\,\delta_{\alpha\beta}. \tag{2.7}$$

Following standard parlance, I will refer to $V_{\alpha\beta}$ as the EFG, even though strictly speaking it is only the traceless part of the electric field gradient. The EFG in a sample consists of a static and a dynamic internal component — externally applied EFGs are used extremely rarely.

The nuclear spin Hamiltonian

Based on symmetry arguments, it can be shown that nuclei with $I \geq \frac{3}{2}$ also have a magnetic octupole moment, those with $I \geq 2$ have an electric hexadecapole moment, etc. However, their interactions are usually negligible compared to the magnetic dipolar and electric quadrupolar interactions [2, p. 170]. Therefore, we write the Hamiltonian for a single nuclear spin as

$$\mathcal{H} = \mathcal{H}_\mathrm{Z} + \mathcal{H}_Q. \tag{2.8}$$

Nucleus	I	$\frac{\gamma}{2\pi}$ (MHz/T)	Q ($10^{-30}\,\mathrm{m}^2$)	Natural abundance (%)
^{1}H	1/2	42.5762	—	99.99
^{2}H	1	6.5357	0.29	0.01
^{13}C	1/2	10.7058	—	1
^{17}O	5/2	−5.7718	−2.6	0.04
^{27}Al	5/2	11.0940	15	100
^{31}P	1/2	17.2352	—	100
^{63}Cu	3/2	11.2893	−22.0	69.15
^{65}Cu	3/2	12.0932	−20.4	30.85
^{89}Y	1/2	−2.0863	—	100
^{139}La	7/2	6.0142	20	99.9
^{175}Lu	7/2	4.862	349	97
^{203}Tl	1/2	24.3209	—	29.5
^{205}Tl	1/2	24.5596	—	70.5

Table 2.1: List of properties of selected nuclei, extracted from [23, p. 114–125].

When the Hamiltonian (equation 2.8) is dominated by the Zeeman term, we speak of nuclear magnetic resonance (NMR). When it is dominated by the quadrupolar term instead, we speak of nuclear quadrupole resonance (NQR).

Values of the spin I, magnetogyric ratio γ, and quadrupole moment Q for selected nuclei are tabulated in Table 2.1. For typical magnetic fields of several tesla, the energy level splitting of nuclear spin states is of the order of 10^{-7} eV, corresponding to temperatures of 10^{-3} K, frequencies of orders 10^{7} to 10^{8} Hz or wavelengths of electromagnetic radiation of order 10 m. In the solid state, in zero magnetic field, typical energy level splittings due to the intrinsic EFG of the sample are of the order of 10^{-9} to 10^{-5} eV, corresponding to temperatures of orders 10^{-5} to 10^{-1} K, frequencies of orders 10^{5} to 10^{9} Hz, and wavelengths of electromagnetic radiation of orders 10^{-1} to 10^{3} m.

These energy scales are at least 10 orders of magnitude smaller than typical differences between nuclear energy levels, therefore any admixture of excited nuclear states is negligible [81, p 12ff]. Typical dimensions of the sample and the radio-frequency coil used for transmission and reception are some millimetres, which is much smaller than the typical RF wavelengths. Thus, the electromagnetic field from the RF coil may be described by the magneto-quasi-static approximation [59, p. 218ff].

In thermodynamic equilibrium, the density matrix describing the nuclear

spin system is thus

$$\rho = \frac{\exp(-\frac{\hbar\mathcal{H}}{k_\mathrm{B}T})}{Z} \approx \frac{1-\frac{\hbar\mathcal{H}}{k_\mathrm{B}T}}{Z} \tag{2.9}$$

$$Z = \mathrm{tr}\exp(-\frac{\hbar\mathcal{H}}{k_\mathrm{B}T}) \approx \mathrm{tr}(1-\frac{\hbar\mathcal{H}}{k_\mathrm{B}T}) \tag{2.10}$$

within the high temperature approximation [33, p. 161]. This is an excellent approximation for our purpose, as all measurements described in this thesis were performed well above 1 K.

2.1.2 Semiclassical Model of NMR

Bloch equations

Many basic principles of NMR can be well understood in terms of the semiclassical dynamics of the nuclear magnetisation $\vec{M}^{nucl} = \hbar\gamma\langle\vec{I}\rangle$ in an applied magnetic field along the z-axis $\vec{B}_0 = B_0\vec{e}_z$. The Hamiltonian of this system is given by

$$\mathcal{H}_0 = -\gamma I_z B_0. \tag{2.11}$$

In thermal equilibrium, the nuclear magnetisation due to the applied field is $M_0\vec{e}_z$. The dynamics of a nuclear spin under this Hamiltonian are given by the Heisenberg equation of motion (c.f. [125, p. 95])

$$\frac{\mathrm{d}}{\mathrm{d}t}\langle\vec{I}\rangle = i\left\langle[\mathcal{H}_0,\vec{I}]\right\rangle = -\gamma\vec{B}_0\times\langle\vec{I}\rangle = \omega_0\vec{e}_z\times\langle\vec{I}\rangle, \tag{2.12}$$

$$\omega_0 = -\gamma B_0, \tag{2.13}$$

which can be rewritten in terms of the magnetisation as

$$\frac{\mathrm{d}}{\mathrm{d}t}\vec{M}^{nucl} = \omega_0\vec{e}_z\times\vec{M}^{nucl}, \tag{2.14}$$

where ω_0 is the Larmor frequency [81, p. 29]. This it the equation of motion for gyroscopic precession with angular velocity ω_0. Positive ω_0 corresponds to counterclockwise precession in the xy-plane, whereas negative ω_0 corresponds to clockwise precession.

Phenomenologically introducing nuclear spin relaxation into equation 2.14 gives us the Bloch equations (see e.g. [2, p. 45] or [128, p. 34])

$$\frac{\mathrm{d}}{\mathrm{d}t}\begin{pmatrix}M_x^{nucl}\\M_y^{nucl}\\M_z^{nucl}\end{pmatrix} = -\gamma\vec{B}\times\vec{M}^{nucl} - \begin{pmatrix}\frac{1}{T_2}M_x^{nucl}\\\frac{1}{T_2}M_y^{nucl}\\\frac{1}{T_1}(M_z^{nucl}-M_0)\end{pmatrix}, \tag{2.15}$$

with T_1 the longitudinal relaxation time and T_2 the transverse relaxation time or dephasing time. The two relaxation times are related in general by $T_2 \leq 2T_1$ [81, p. 284].

An alternative name for T_1 is "spin–lattice relaxation time", as its physical origin lies in the fluctuations of degrees of freedom other than the nuclear spin system under study, e.g. lattice vibrations or electronic magnetic moments.

A popular but misleading name for T_2 is "spin–spin relaxation time". It can originate from nuclear-spin–nuclear-spin interactions, however, spin–lattice relaxation mechanisms also contribute to and sometimes dominate transverse relaxation [81, p. 35] — this will be discussed theoretically in sections 4.4 and 4.8 and experimentally in sections 5.3.3 and 5.4.2.

Dynamics with an applied radio-frequency field

In order to perform an NMR measurement, the nuclear spin system must be brought out of equilibrium. This is achieved by applying a radio-frequency magnetic field

$$\vec{B}_{rf}(t) = 2B_1 \cos(|\omega_{rf}|\, t + \psi_p)\vec{e}_x \tag{2.16}$$

perpendicular to the static field $\vec{B}_0$ [81, p. 179ff].

Its effects are more easily understood by transforming to a rotating frame of reference

$$\vec{M}' = R(t)\vec{M}^{nucl} \tag{2.17}$$

$$R(t) = \begin{pmatrix} \cos(\omega_{rf}t) & \sin(\omega_{rf}t) & 0 \\ -\sin(\omega_{rf}t) & \cos(\omega_{rf}t) & 0 \\ 0 & 0 & 1 \end{pmatrix} \tag{2.18}$$

with an angular velocity

$$\omega_{rf} = |\omega_{rf}| \operatorname{sign}(\omega_0). \tag{2.19}$$

To simplify the following expressions, we rewrite the phase of the RF field as

$$\phi_p = \psi_p \operatorname{sign}(\omega_0). \tag{2.20}$$

Note however that frequency and phase which we control experimentally are those of the RF current in a coil, i.e. $|\omega_{rf}|$ and ψ_p [80].

In the rotating frame of reference, the static field remains unchanged and the RF field transforms to

$$\begin{aligned} \vec{B}'_{rf}(t) =& B_1(\cos(\phi_p)\vec{e}_x + \sin(\phi_p)\vec{e}_y) \\ &+ B_1(\cos(2\omega_{rf}t + \phi_p)\vec{e}_x - \sin(2\omega_{rf}t + \phi_p)\vec{e}_y). \end{aligned} \tag{2.21}$$

The equations of motion are transformed to

$$\frac{\mathrm{d}}{\mathrm{d}t}\vec{M}' = \frac{\mathrm{d}R}{\mathrm{d}t}R^{\mathrm{T}}\vec{M}' - \gamma\vec{B}' \times \vec{M}' - \begin{pmatrix} \frac{1}{T_2}M'_x \\ \frac{1}{T_2}M'_y \\ \frac{1}{T_1}(M'_z - M_0) \end{pmatrix}, \tag{2.22}$$

where the time-dependence of the transformation gave rise to the term

$$\frac{\mathrm{d}R}{\mathrm{d}t}R^{\mathrm{T}}\vec{M}' = -\omega_{rf}\vec{e}_z \times \vec{M}'. \tag{2.23}$$

We now simplify the RF field by neglecting the rapidly oscillating terms in the rotating frame

$$\vec{B}_{rf} \approx \vec{B}_1' = B_1(\cos(\phi_p)\vec{e}_x + \sin(\phi_p)\vec{e}_y) \tag{2.24}$$

and define

$$\omega_1 = -\gamma B_1 \tag{2.25}$$

in analogy to ω_0.

This allows us to re-write the equations of motion in the rotating frame as

$$\frac{\mathrm{d}}{\mathrm{d}t}\vec{M}' = \begin{pmatrix}\omega_1 \cos\phi_p \\ \omega_1 \sin\phi_p \\ \omega_0 - \omega_{rf}\end{pmatrix} \times \vec{M}' - \begin{pmatrix}\frac{1}{T_2}M_x' \\ \frac{1}{T_2}M_y' \\ \frac{1}{T_1}(M_z' - M_0)\end{pmatrix}. \tag{2.26}$$

Pulsed NMR and Spin Echoes

Most NMR experiments are performed by applying a sequence of RF pulses on (or near) resonance ($\omega_{rf} \approx \omega_0$) and then detecting the precession of nuclear magnetisation [81, p. 33ff]. The detection of any precession is only feasible if the nuclear spins do not relax too fast. We may therefore assume that $T_2^{-1} \ll \omega_1$. For the excitation of nuclear spins, one typically uses pulses whose length τ is chosen such that $\omega_1\tau = \mathcal{O}(1)$, and thus $T_2^{-1}\tau \ll 1$. With this approximation, the evolution of nuclear magnetisation during an RF pulse is determined by equation 2.26 with negligible relaxation.

The simplest possible pulsed NMR experiment consists of a single pulse on resonance followed by signal acquisition. In the rotating frame of reference, the effect of the pulse is to nutate the nuclear magnetisation away from its equilibrium position along $\vec{e}_z$ by an angle $\omega_1\tau$ about the axis $\cos\phi_p\vec{e}_x + \sin\phi_p\vec{e}_y$. Typically, one calls such a pulse a "$(|\omega_1\tau|)_e$-pulse", where e stands for the axis of rotation (e.g. a $(\pi/2)_y$-pulse corresponds to a rotation by $\pi/2$ about $\vec{e}_y$) [81, p. 89]. The case of negative ω_1 is accounted for in this notation by reversing the sign of axis of rotation (as this yields an equivalent rotation).

Applying a $\pi/2$-pulse brings the nuclear magnetisation from equilibrium to the xy-plane. This gives the maximal precessing magnetisation and thus the maximal NMR signal.

In practice, individual nuclei of the same species in an NMR sample often have different resonance frequencies, due to e.g. different orientations of crystallites in a powder sample of an anisotropic material. This distribution of frequencies causes a dephasing of the signal. In all NMR experiments

discussed in this thesis, this dephasing was rapid enough to make single-pulse experiments impossible.

The problem of rapid dephasing due to static or coherent effects can often be overcome by using multiple-pulse experiments [35, p. 25ff]. Our case of a broad distribution of static magnetic fields can be handled by the simplest two-pulse sequence, the Hahn echo: $\pi/2$ — τ — π — acquire. By flipping the spins, the π-pulse inverts the phase which they have acquired after freely precessing for a time τ. Therefore, after another time τ, the dephasing is cancelled and all spins are in phase again. This gives a maximum in the NMR signal known as a *spin echo* [2, p. 58f]. In this sense, the Hahn echo refocusses the static field distribution.

Measuring the spin echo amplitude at different delays 2τ yields the signal decay ("T_2-decay") due to coherent effects that are not refocussed (e.g. homonuclear spin–spin interactions for the Hahn echo sequence) as well as incoherent effects (spin–lattice relaxation). Disentangling these effects in a useful way is usually highly challenging in strongly-correlated electron materials. One example of such an analysis for ^{63}Cu-NMR in the high-temperature superconductor $YBa_2Cu_3O_{7-x}$ can be found in references [107, 58]. A similar analysis for ^{17}O–NMR in the rare-earth nickelates in sections 5.3.3 and 5.4.2 shows that spin–lattice relaxation fully determines the T_2 in all materials except $LaNiO_3$.

Measuring T_1

In order to measure T_1, we first bring the nuclear magnetisation out of equilibrium, to some configuration along $\vec{e}_z$. Next, we wait for some time t to let M_z relax. Finally, we convert M_z to an NMR signal by using an appropriate pulse sequence, e.g. a single $\pi/2$-pulse or, in our case, a Hahn echo. This is done for several different values of t, which are typically chosen with logarithmic spacing, and the resulting curve $M_z(t)$ is fitted to extract the value for T_1.

In an inversion recovery (IR) experiment, the initial state is $M_z(t = 0) = -M_0$, which is created by applying a single π-pulse to a spin system in thermal equilibrium [81, p. 295ff]. This has been the preferred method to measure T_1 throughout most of this thesis.

In saturation recovery (SR), the initial state is $M_z(t = 0) = 0$, and is typically prepared using a long sequence of $\pi/2$ pulses designed to destroy any coherence in the xy-plane [35, p. 174ff]. For some experiments, I have used the *aperiodic saturation recovery* (APSR) sequence, which consists of N $\pi/2$ pulses with a delay of $(N-k)\tau_{APSR}$ between the k'th and $k+1$'th pulse.

The advantage of SR is that the initial state need not be in thermal equilibrium, and therefore repetition times faster than T_1 are permissible. However, for comparable signal strength, the fits to the $M_z(t)$ tend to be

less stable for SR, because all data at short times t are dominated by noise, whereas for IR this is the case only for data points close to the zero-crossing of $M_z(t)$.

Chemical Shift and Shift Referencing

The experimental NMR frequency of a nucleus in a sample in an applied field depends on the magnetic properties of the sample. In a material or molecule with electronic low-energy magnetic degrees of freedom, e.g. itinerant-electron spins in a metal or local magnetic moments in a sample containing d- or f-block ions, the NMR frequency is affected by the hyperfine interaction of nuclear and electronic magnetic moments. However, even in a diamagnetic insulator, the NMR frequency is still shifted by the shielding of the magnetic field due to the response of filled electron orbitals. This is known as the chemical shift [81, p. 51].

Since NMR spectroscopy is concerned only with nuclei in molecules and materials, the magnetogyric ratios used in NMR spectroscopy are usually not those of a bare nucleus. Instead, for each nucleus, an effective gyromagnetic ratio in a reference compound is reported, such that the chemical shift is defined to be zero for the reference.

In high-resolution NMR spectroscopy, accurate chemical shift referencing is of paramount importance, as sub-ppm accuracy is often required. This is achieved by measuring the NMR frequency of both the sample of interest as well as a reference sample for the same nucleus.

For this thesis, this technique was not necessary as I encountered shifts of the order of 10^3 to 10^4 ppm. Instead, the magnetic field is determined by measuring the resonance frequency of ^{27}Al in aluminium foil, using the known (Knight) shift of ^{27}Al in aluminium metal (1640 ppm, see ref. [13]) to calculate the reference frequency for ^{27}Al. The reference frequencies for other nuclei are then computed using the literature values for their magnetogyric ratio reported in table 2.1.

2.1.3 Quantum Model of Nuclear Spin Spectroscopy

In a real molecule or material, a nucleus experiences not only applied fields but also fields which originate from within the sample. The structural and electronic degrees of freedom (the "lattice") can cause rapidly fluctuating electromagnetic fields at the position of the nucleus, which causes spin–lattice relaxation. Since these fluctuations are much faster than the nuclear spin dynamics, the shape of the nuclear spin spectrum is usually completely defined by the average value of those fields. Therefore, in this section, only the mean internal fields are considered.

Static applied magnetic field

For a standard NMR experiment, the sample is placed inside a strong magnetic field, almost always inside the bore of a superconducting electromagnet. In samples without magnetic order and with small or zero quadrupole contribution, $\mathcal{H}_0$ is usually the dominant contribution to the full Hamiltonian (equation 2.11) such that all other contributions can be treated perturbatively. If there is magnetic order, this causes an additional static magnetic field inside the material, which must be added to $\vec{B}_0$.

In thermodynamic equilibrium, the density matrix of an ensemble of nuclear spins obeying $\mathcal{H}_0$ is found using equation 2.9:

$$\rho_0 = \frac{1}{2I+1}\big(1 - \frac{\hbar\omega_0}{k_\mathrm{B}T} I_z\big). \tag{2.27}$$

and the magnetisation per nucleus is

$$M_0 = \langle \mu_z \rangle = \mathrm{tr}(\mu_z \rho_0) = (\hbar\gamma)^2 \frac{B_0}{k_\mathrm{B}T} \frac{I(I+1)}{3}. \tag{2.28}$$

Applied RF magnetic field

The interaction of the RF magnetic field $\vec{B}_{rf}(t)$ defined in equation 2.16 with a nuclear spin is given by the Hamiltonian

$$\mathcal{H}_{rf}(t) = -\gamma \vec{I} \cdot \vec{B}_{rf}(t) = 2\omega_1 \cos(|\omega_{rf}|\, t + \psi_p) I_x. \tag{2.29}$$

In order to transform to the rotating frame of reference defined above, we use a unitary transformation of the nuclear spin states is given by the operator

$$U(t) = \exp(i\omega_{rf} t I_z) \tag{2.30}$$

which transforms states according to

$$|\psi'\rangle = U(t)\,|\psi\rangle\,. \tag{2.31}$$

Since the transformation $U(t)$ is time-dependent, the Hamiltonian transforms as

$$\mathcal{H}'(t) = U(t)\mathcal{H}U^\dagger(t) + i\frac{\mathrm{d}U(t)}{\mathrm{d}t}U^\dagger(t). \tag{2.32}$$

The unperturbed Hamiltonian $\mathcal{H}_0$ is thus transformed into

$$\mathcal{H}'_0(t) = U(t)\mathcal{H}_0 U^\dagger(t) + i\frac{\mathrm{d}U(t)}{\mathrm{d}t}U^\dagger(t) = (\omega_0 - \omega_{rf}) I_z \tag{2.33}$$

and the perturbation $\mathcal{H}_{rf}$ becomes

$$\begin{aligned}
\mathcal{H}'_{rf}(t) &= U(t)\mathcal{H}_{rf}(t)U^\dagger(t) \\
&= 2\omega_1 \cos(\omega_{rf} t + \phi_p)(I_x \cos\omega_{rf} t - I_y \sin(\omega_{rf} t)) \\
&= \frac{\omega_1}{2}(\mathrm{e}^{i(\omega_{rf}t+\phi_p)} + \mathrm{e}^{-i(\omega_{rf}t+\phi_p)})(I_+ \mathrm{e}^{i\omega_{rf}t} + I_- \mathrm{e}^{-i\omega_{rf}t}) \\
&= \frac{\omega_1}{2}\big(I_+ \mathrm{e}^{-i\phi_p} + I_- \mathrm{e}^{i\phi_p} + I_+ \mathrm{e}^{i(2\omega_{rf}t+\phi_p)} + I_- \mathrm{e}^{-i(2\omega_{rf}t+\phi_p)}\big).
\end{aligned} \tag{2.34}$$

We can now take the rotating wave approximation (RWA), i.e. neglect the rapidly oscillating terms, and write

$$\begin{aligned}\mathcal{H}'_{rf}(t) \approx \mathcal{H}'_1(t) &= \frac{\omega_1}{2}\left(I_+ \mathrm{e}^{-i\phi_p} + I_- \mathrm{e}^{i\phi_p}\right) \\ &= \omega_1\left(I_x \cos(\phi_p) + I_y \sin(\phi_p)\right).\end{aligned} \tag{2.35}$$

Note that this expression only applies to NMR (and not NQR), and that it assumes that the RF pulse is approximately resonant with all $\Delta m = 1$ transitions of the nuclear spin ("hard pulse limit"). For nuclei with spin $I \geq 1$ in a sufficiently strong EFG, different transitions occur at different frequencies and only a single transition can be excited. This situation will be encountered in chapter 5. Then, the two levels involved in the transition can be treated as a "pseudo-spin 1/2" system, and the effective Hamiltonian $\mathcal{H}'_1(t)$ takes the same form as in equation 2.35 except for a prefactor.

Transforming back into the laboratory frame, we see that the RWA projects the linearly polarised RF field onto the co-rotating circularly polarised component:

$$\mathcal{H}_1(t) = U^\dagger(t)\mathcal{H}'_1(t)U(t) = \omega_1\left(I_x \cos(\omega_{rf}t + \phi_p) + I_y \sin(\omega_{rf}t + \phi_p)\right). \tag{2.36}$$

NMR shift tensor

In diamagnetic or paramagnetic sample inside an applied field $\vec{B}_0 = B_0\vec{e}_z$, the magnetic field at a nucleus has a contribution from the response of the material. I will assume that this response is linear. In the solid state, this response can have some anisotropy depending on the point group symmetry at the nucleus under study. The field at a nucleus is thus given by

$$\vec{B} = (1 + \delta)\vec{B}_0 \tag{2.37}$$

with δ the NMR shift tensor.

In insulators without local magnetic moments, the shift tensor is equal to the chemical shift. In insulators with local moments and in metals, it also contains a (usually dominant) contribution due to hyperfine interactions.

Since δ is typically small, its effect is treated to first order in perturbation theory:

$$|\vec{B}| = |B_0\vec{e}_z + (\vec{e}_x\delta_{xz} + \vec{e}_y\delta_{yz} + \vec{e}_z\delta_{zz})B_0| = (1+\delta_{zz})B_0 + \mathcal{O}\left(\delta^2 B_0\right). \tag{2.38}$$

For dealing with powder samples, it will be useful to decompose the shift tensor into irreducible representations (irreps) of spatial rotation group SO(3). The space of linear operators acting on 3-dimensional Euclidean space can be decomposed into an $l = 0$, an $l = 1$, and an $l = 2$ irrep. The $l = 0$ irrep consists of isotropic tensors, i.e. those proportional to the identity. The $l = 1$ irrep contains the antisymmetric matrices, and the $l = 2$ irrep the symmetric traceless matrices [125, p. 246].

The isotropic part of δ is called the isotropic shift [81, p. 198]

$$\delta_{iso} = \frac{1}{3} \operatorname{tr} \delta. \tag{2.39}$$

The antisymmetric part of δ does not contribute to the NMR frequency to first order (c.f. equation 2.38), therefore it is usually neglected.

Finally, the traceless symmetric part of δ is known as the shift anisotropy tensor δ_{SA}.

Since the relevant part of the shift tensor $\delta_{iso} + \delta_{SA}$ is a real symmetric matrix, it can be diagonalised by rotating to a suitable coordinate frame:

$$\delta_{iso} + \delta_{SA} = \begin{pmatrix} \delta_{xx} & 0 & 0 \\ 0 & \delta_{yy} & 0 \\ 0 & 0 & \delta_{zz} \end{pmatrix}. \tag{2.40}$$

In this thesis, I will parametrise the eigenvalues $\delta_{\alpha\alpha}$ according to

$$\begin{aligned} \delta_{iso} &= \frac{1}{3}(\delta_{xx} + \delta_{yy} + \delta_{zz}) \\ \delta_{aniso} &= \delta_{zz} - \delta_{iso} \\ \eta_S &= \frac{\delta_{xx} - \delta_{yy}}{\delta_{aniso}} \end{aligned} \tag{2.41}$$

with the eigenvalues ordered such that

$$|\delta_{zz} - \delta_{iso}| \geq |\delta_{yy} - \delta_{iso}| \geq |\delta_{xx} - \delta_{iso}|. \tag{2.42}$$

Notice that this implies that $0 \leq \eta_S \leq 1$ [81, p. 199].

If the point group symmetry at the nucleus under study is large, e.g. cubic (O_h), the shift anisotropy must be zero by symmetry. Similarly, if there is a 3-fold or higher rotation axis along z, then η_S must be zero.

If an experimental NMR powder spectrum cannot be fitted for some reason, it is often still possible to extract δ_{iso} by finding the first moment ("centre of mass") m_1 of the spectrum $S(\omega)$:

$$m_1 = \int \mathrm{d}\omega \, \omega S(\omega). \tag{2.43}$$

Since m_1 is just the average NMR frequency of all nuclei, the shift anisotropy is averaged out. If there is no quadrupolar interaction, the first moment is therefore related to the isotropic shift as

$$m_1 = \omega_0(1 + \delta_{iso}). \tag{2.44}$$

Quadrupolar interaction

Since the EFG is a real symmetric matrix by definition, it is diagonalisable. In the principal axis frame of the EFG, the nuclear quadrupole Hamiltonian is commonly written as

$$\mathcal{H}_Q = \frac{2\pi C_Q}{4I(2I-1)}\left(3I_z^2 - \vec{I}^2 + \eta_Q(I_x^2 - I_y^2)\right) \tag{2.45}$$

$$C_Q = \frac{eQV_{zz}}{2\pi\hbar} \tag{2.46}$$

$$\eta_Q = \frac{V_{xx} - V_{yy}}{V_{zz}} \tag{2.47}$$

$$|V_{zz}| \geq |V_{yy}| \geq |V_{xx}|\,. \tag{2.48}$$

Using the fact that $V_{\alpha\beta}$ is traceless and its eigenvalues are ordered according to equation 2.48, we can see from equation 2.47 that $0 \leq \eta_Q \leq 1$. Both η_Q and C_Q can be constrained by the point group symmetry at the site of the nucleus under study, in complete analogy to η_S and δ_{aniso} as discussed above.

In this thesis, I will report all results on EFGs in terms of C_Q and η_Q. However, for the derivations in this chapter, I will rewrite $\mathcal{H}_Q$ as

$$\mathcal{H}_Q = \frac{\omega_Q}{6}\left(3I_z^2 - \vec{I}^2 + \eta_Q\frac{I_+^2 + I_-^2}{2}\right), \tag{2.49}$$

$$\omega_Q = 2\pi\frac{3C_Q}{2I(2I-1)}. \tag{2.50}$$

Nuclear Quadrupole Resonance

To find the NQR frequencies of a nucleus in zero applied field, we have to find the eigenvalues and eigenstates of $\mathcal{H}_Q$. In the axially symmetric case ($\eta_Q = 0$), $\mathcal{H}_Q$ is diagonal in the canonical basis:

$$\mathcal{H}_Q\,|m\rangle = \frac{\omega_Q}{6}\left(3m^2 - I(I+1)\right)|m\rangle = \omega_m^{NQR}\,|m\rangle\,. \tag{2.51}$$

Since only transitions with $\Delta m = \pm 1$ can be detected with an RF coil, the NQR frequencies in the axially symmetric case are

$$\left|\omega_{m-1}^{NQR} - \omega_m^{NQR}\right| = \left|\omega_Q(m - \frac{1}{2})\right| = \begin{cases}\omega_Q, 2\omega_Q, \ldots, (I-\frac{1}{2})\omega_Q \\ \frac{1}{2}\omega_Q, \frac{3}{2}\omega_Q, \ldots, (I-\frac{1}{2})\omega_Q\end{cases} \tag{2.52}$$

for half-integer and integer spins I respectively.

If $\eta_Q \neq 0$ instead, $\mathcal{H}_Q$ mixes different $|m\rangle$ and all transitions between any two energy levels become observable.

NMR with perturbative quadrupolar interaction

In chapter 5, we will find a quadrupolar interaction that is significantly weaker than the Zeeman interaction. In this "quadrupolar NMR" regime, one can treat the quadrupolar interaction as a perturbation to the Zeeman Hamiltonian. In this section, I will present some well-known results from first- and second-order perturbation theory.

First, we must account for the fact that the quadrupole Hamiltonian (equation 2.49) is typically formulated in the principal-axis frame (PAF) of the EFG, which is locked to the crystal, whereas the Zeeman Hamiltonian (equation 2.11) is usually written in the laboratory frame (LF) with the z-axis along the magnetic field. Let us define the rotation that transforms a vector between the two coordinate frames

$$\vec{v}_{PAF} = R_z(\varphi)R_y(\theta)R_z(\psi)\vec{v}_{LF} \tag{2.53}$$

where $R_e(\alpha)$ is a counterclockwise rotation about the axis e by an angle α. Note that any rotation can be parameterised by the three Euler angles φ, θ, and ψ [125, p. 183].

The transformations of a wavefunction $|\psi\rangle$ and an operator A acting on a single spin I are then given by

$$\begin{aligned} U &= \mathrm{e}^{i\psi I_z}\mathrm{e}^{i\theta I_y}\mathrm{e}^{i\varphi I_z} \\ |\psi_{LF}\rangle &= U\,|\psi_{PAF}\rangle \\ A_{LF} &= U A_{PAF} U^\dagger. \end{aligned} \tag{2.54}$$

Thus, the quadrupole Hamiltonian in the LF (where $\mathcal{H}_0$ is diagonal) is defined as

$$\mathcal{H}_Q^{LF} = U\mathcal{H}_Q^{PAF}U^\dagger. \tag{2.55}$$

The first-order correction to the energy levels due to $\mathcal{H}_Q^{LF}$ can be written as

$$\mathcal{H}_Q^{(1)} = \frac{\omega_Q}{6}\big(\frac{3\cos^2\theta - 1}{2} + \frac{\eta_Q}{2}\sin^2\theta\cos 2\varphi\big)(3I_z^2 - \vec{I}^2). \tag{2.56}$$

Two properties of this expression are worth noting here. First, if one averages over all crystallite orientations, $\mathcal{H}_Q^{(1)}$ vanishes. Therefore, it does not contribute to the first moment of the NMR powder spectrum. Second, for half-integer spins, the frequency of the *central transition* $|1/2\rangle \leftrightarrow |-1/2\rangle$ is not affected by $\mathcal{H}_Q^{(1)}$. Nevertheless, the spectrum of the central transition does contain information on the EFG due to second-order effects.

For an axially symmetric EFG ($\eta_Q = 0$), the second-order correction is given by

$$\begin{aligned} \mathcal{H}_{Q,ax}^{(2)} = \frac{\omega_Q^2}{4\omega_0}\big(&\sin^2\theta\cos^2\theta(4I_z^3 + (-2\vec{I}^2 + \frac{1}{2})I_z) + \\ &\sin^4\theta(-\frac{1}{4}I_z^3 + (\frac{1}{4}\vec{I}^2 - \frac{1}{8})I_z)\big). \end{aligned} \tag{2.57}$$

Averaging $\mathcal{H}^{(2)}_{Q,ax}$ over all crystallite orientation yields its isotropic component

$$\mathcal{H}^{(2)}_{Q,ax,iso} = \frac{\omega_Q^2}{4\omega_0}\frac{2}{5}(I_z^3 - \frac{1}{3}\vec{I}^2 I_z). \tag{2.58}$$

For the powder spectrum of the central transition, this modifies the first moment from equation 2.44 to

$$m_1 = \omega_0(1+\delta_{iso}) - \frac{\omega_Q^2}{30\omega_0}(\vec{I}^2 - \frac{3}{4}). \tag{2.59}$$

In chapter 5, I will use this expression to extract the isotropic shift in temperature-dependent measurements.

2.1.4 The Free Induction Decay

In a normal experimental NMR setup, the sample is placed inside a single RF solenoid along the x-axis, which is used for both excitation pulses and detection of the nuclear spin precession. By Faraday's law of induction [59, p. 208ff], the precessing nuclear magnetisation induces a voltage across the RF coil

$$\begin{aligned} V_{FID}(t) &\propto -\frac{\mathrm{d}}{\mathrm{d}t}\int \vec{B}_{nucl}\cdot\vec{e}_x \,\mathrm{d}\sigma \propto -\frac{\mathrm{d}}{\mathrm{d}t}\langle\mu_x\rangle \\ &\propto -\gamma\frac{\mathrm{d}}{\mathrm{d}t}\langle I_x\rangle =: -S_{FID}(t), \end{aligned} \tag{2.60}$$

where $\mathrm{d}\sigma$ is the area element of a slice through the sample perpendicular to the x-direction. This signal is called the free induction decay (FID).

FID from nuclei in a static field after a $\frac{\pi}{2}$-pulse

In order to acquire a simple FID, we start from the thermal equilibrium state and apply a $\frac{\pi}{2}$-pulse at time $t = 0$, i.e. we turn on the RF field for a time $\tau = \frac{\pi}{2|\omega_1|}$. Here, I will assume "hard" pulses, i.e. that the bandwidth of the excitation is large compared to the width of the NMR spectrum. Using Equations 2.27 and 2.35, we can obtain the density matrix in the rotating frame after the $\pi/2$-pulse

$$U_1'(t) = \exp(-i\mathcal{H}_1' t) \tag{2.61}$$

$$\begin{aligned} \rho'(t=0) &= U_1'(\tau)\rho_0 U_1'(\tau)^\dagger \\ &= \frac{1}{2I+1}\Big(1 + \frac{\hbar|\omega_0|}{k_\mathrm{B}T}\big(-I_x\sin\phi_p + I_y\cos\phi_p\big)\Big). \end{aligned} \tag{2.62}$$

Note that at time $t = 0$, the rotating frame of reference and the laboratory frame are equal, thus $\rho'(t=0) = \rho(t=0)$.

After the $\pi/2$-pulse, the density matrix evolves as

$$U_0(t) = \exp(-i\mathcal{H}_0 t), \tag{2.63}$$

$$\begin{aligned}\rho(t) &= U_0(t)\rho(t=0)U_0^\dagger(t) \\ &= \frac{1}{2I+1}\Big(1 + \frac{\hbar\,|\omega_0|}{k_\mathrm{B}T}\big(-I_x\sin(\omega_0 t+\phi_p) + I_y\cos(\omega_0 t+\phi_p)\big)\Big).\end{aligned} \tag{2.64}$$

We can then compute the FID signal

$$\begin{aligned}S_{FID}(t) &= \frac{\mathrm{d}}{\mathrm{d}t}\langle\gamma I_x(t)\rangle = \frac{\mathrm{d}}{\mathrm{d}t}\,\mathrm{tr}\left(\gamma I_x\rho(t)\right) \\ &= \frac{\mathrm{d}}{\mathrm{d}t}\frac{\hbar\,|\omega_0|}{k_\mathrm{B}T}\gamma\frac{-\sin(\omega_0 t+\phi_p)}{2} \\ &= \frac{\mathrm{d}}{\mathrm{d}t}\frac{\hbar\,|\omega_0|}{k_\mathrm{B}T}\,|\gamma|\,\frac{\sin(|\omega_0|\,t+\psi_p)}{2} \\ &= \frac{1}{2}\frac{\hbar\,|\omega_0|}{k_\mathrm{B}T}\,|\gamma|\,|\omega_0|\cos(|\omega_0|\,t+\psi_p) \\ &= \frac{1}{2}\frac{\hbar}{k_\mathrm{B}}\frac{|\gamma|^3 B_0^2}{T}\cos(|\omega_0|\,t+\psi_p)\end{aligned} \tag{2.65}$$

Notice that the sign of γ does not enter this expression.

The receiver of the NMR spectrometer amplifies this signal and down-converts it using quadrature detection [81, p. 73f], such that the recorded signal becomes

$$\begin{aligned}S(t) &\propto \exp\left(i((|\omega_0| - |\omega_{rf}|)t + \psi_p - \psi_{RX})\right) \\ &= \exp\left(\mathrm{sign}(\omega_0)i((\omega_0-\omega_{rf})t + \phi_p - \phi_{RX})\right)\end{aligned} \tag{2.66}$$

with $\psi_{RX} = \phi_{RX}\,\mathrm{sign}(\omega_0)$ the receiver phase. The RF electronics of the NMR spectrometers which I have used for this dissertation project are described in full detail in the PhD thesis of Matthias Weller [141] and in my Master's thesis [71].

As discussed in section 2.1.2, all NMR and NQR data presented in this thesis was acquired using spin echoes. In the Hahn echo sequence, at some time τ after the initial $\pi/2$ pulse, a π pulse is added before starting the data acquisition. The quantum mechanical treatment of spin echoes is described in detail in reference [128, p. 46ff].

2.1.5 Powder Averaging and Powder Spectra

All NMR experiments performed as part of this thesis used samples in powder form. Since the solid-state NMR Hamiltonian contains terms which depend on the orientation of the applied magnetic field with respect to the crystal axes, calculating the NMR spectrum of a powder sample requires the co-addition of single-crystal spectra with all possible orientations. In

the limit of large applied static fields, the angle between the crystal axes and the RF field does not affect the NMR spectrum, thus only the direction of the static field affects the NMR spectrum.

The powder FID signal $S_p(t)$ is related to single-crystal FID signal $S_{sc}(t;\theta,\varphi)$ by averaging over all solid angles

$$S_p(t) = \int S_{sc}(t;\theta,\varphi)\frac{\mathrm{d}\Omega}{4\pi}. \tag{2.67}$$

Let us assume that the single-crystal spectrum consists of a set of Lorentzian lines

$$\begin{aligned} S_{sc}(t;\theta,\varphi) &= \sum_k A^{(k)}(\theta,\varphi)\exp(i\omega^{(k)}(\theta,\varphi)t - \frac{t}{T_2^{(k)}(\theta,\varphi)}) \\ &\approx \sum_k A^{(k)}\exp(i\omega^{(k)}(\theta,\varphi)t - \frac{t}{T_2^{(k)}}), \end{aligned} \tag{2.68}$$

where in the second line, we made the assumptions that the amplitude and linewidth are independent of the direction of the magnetic field. The former assumption is easily justified, as the amplitude of the NMR signal is usually proportional to the number of resonant nuclei. The latter assumption may be violated in materials with strongly anisotropic magnetic behaviour.

Fourier transforming equation 2.68 yields

$$\begin{aligned} S_{sc}(\omega;\theta,\varphi) &= \sum_k A^{(k)}(\theta,\varphi)\delta(\omega-\omega^{(k)}(\theta,\varphi)) * L(T_2^{(k)}(\theta,\varphi)) \\ &\approx \sum_k A^{(k)}\delta(\omega-\omega^{(k)}(\theta,\varphi)) * L(T_2^{(k)}), \end{aligned} \tag{2.69}$$

where $L(T_2)$ is a Lorentzian curve with a half-width at half-height of $1/T_2$ and $f * g$ denotes the convolution of two functions f and g.

The NMR powder spectrum can then be calculated as

$$\begin{aligned} S_p(\omega) &= \int S_{sc}(\omega;\theta,\varphi)\frac{\mathrm{d}\Omega}{4\pi} \\ &= \sum_k A^{(k)}\int \delta(\omega-\omega^{(k)}(\theta,\varphi)) * L(T_2^{(k)})\frac{\mathrm{d}\Omega}{4\pi} \\ &= \sum_k A^{(k)}\int \delta(\omega-\omega^{(k)}(\theta,\varphi))\frac{\mathrm{d}\Omega}{4\pi} * L(T_2^{(k)}). \end{aligned} \tag{2.70}$$

In practice, one often uses a Gaussian instead of a Lorentzian lineshape for the convolution, which can phenomenologically account for various broadening mechanisms. The integral can be computed numerically by sampling $\omega^{(k)}(\theta,\varphi)$ and creating a histogram. A more efficient algorithm is based on tessellating the sphere by triangles, evaluating $\omega^{(k)}(\theta,\varphi)$ on the

corners, and using linear interpolation within each triangle [4]. Software for computing NMR powder spectra such as QUEST [111] is often based on this algorithm. In this thesis, I have used a software written by Marek Pikulski in our lab for calculating non-perturbative quadrupolar NMR powder spectra [113], which I have modified to include a shift anisotropy tensor.

2.1.6 Quantum model of nuclear spin relaxation

In any molecule or material, the local magnetic field and EFG at the nucleus fluctuate due to various excitations. In solid-state physics applications, the typical timescale of these fluctuations is usually much shorter than any timescale associated to the nuclear spin dynamics. The mean magnetic field and EFG contribute to the coherent evolution of nuclear spins, which is encoded in the effective nuclear spin Hamiltonian as discussed above. Their fluctuations cause incoherent dynamics, namely relaxation of the nuclear spins. This process is known as "spin–lattice relaxation". In this thesis, two phenomenological channels for spin–lattice relaxation will be discussed: rapidly fluctuating (hyperfine) magnetic fields and rapidly fluctuating EFGs.

Since a quantum mechanical model of nuclear spin relaxation must deal with coherent and incoherent processes, it is best formulated in terms of density matrices. In NMR literature, the density matrix of the whole material is typically called ρ, whereas the reduced density matrix of nuclear spins, where all other degrees of freedom have been traced out, is called σ. Transverse (T_2) relaxation corresponds to the decay of the off-diagonal entries of $\sigma(t)$ in the energy eigenbasis, whereas longitudinal (T_1) relaxation describes the evolution of the diagonal entries, i.e. the energy level populations, towards thermal equilibrium.

Relaxation can be encoded in terms of a linear operator $\hat{\Gamma}$ which acts on (density) matrices, not wavefunctions [77]. In modern NMR literature, operators acting on matrices are called "superoperators" [33, p. 19]. Thus, the full equation of motion for the density matrix is given by

$$\frac{\mathrm{d}\sigma}{\mathrm{d}t} = -i[\mathcal{H}, \sigma] - \hat{\Gamma}\sigma. \tag{2.71}$$

Longitudinal relaxation, measured in e.g. an inversion recovery experiment, is caused purely by spin–lattice relaxation. Transverse relaxation, measured e.g. as the decay of the spin-echo signal depending on the interpulse delay, contains contributions from spin–lattice relaxation as well as nuclear-spin–nuclear-spin interactions which have not been refocussed by the applied pulse sequence. While spin–lattice relaxation causes an exponential spin-echo decay, spin–spin interactions can cause exponential, Gaussian, or more complex time dependences. A detailed discussion of the relevant aspects of nuclear spin relaxation is presented in Chapter 4.

2.1.7 Magnetic hyperfine interactions

The interaction between nuclear and electronic magnetic dipole moments is the Zeeman interaction of the nuclear spin (equation 2.3) with the magnetic field caused by the electronic moment. The magnetic field at the position $\vec{r}$ due to a dipole moment $\vec{m}$ at the origin is [59, p. 188]

$$\vec{B}_d = \frac{\mu_0}{4\pi}\Big(\frac{3(\vec{m}\cdot\vec{e}_r)\vec{e}_r - \vec{m}}{r^3} + \frac{8\pi}{3}\vec{m}\delta^{(3)}(\vec{r})\Big). \tag{2.72}$$

Thus, the Hamiltonian of a nucleus at position r contains the term

$$\mathcal{H}_d = -\gamma\frac{\mu_0}{4\pi}\big(\vec{I}\cdot\frac{3\vec{e}_r\vec{e}_r^{\mathsf{T}} - 1}{r^3}\vec{m} + \frac{8\pi}{3}\delta^{(3)}(\vec{r})\vec{I}\cdot\vec{m}\big). \tag{2.73}$$

The $1/r^3$ term is the usual *dipolar interaction*. Note that the coupling tensor $3\vec{e}_r\vec{e}_r^{\mathsf{T}} - 1$ is traceless and symmetric, and thus belongs to the $l = 2$ representation of $SO(3)$ (see the discussion in section 2.1.3 for the shift anisotropy tensor). The delta function term is the *Fermi contact interaction* (FCI) between nuclear and electronic spins [34]. Electronic wavefunctions are non-zero at the nuclear position only in the case of s-orbitals, thus the FCI acts between nuclear spins and s-electrons only. Since the orbital angular momentum of an s-orbital is zero, the FCI acts on the spin-only magnetic moment of the electron. Note that since the FCI is given by a scalar product of two spins, it is fully isotropic.

Thus, separating the electronic magnetic moment into its orbital and spin contribution gives the full magnetic hyperfine interaction

$$\mathcal{H}_{hf} = \gamma\frac{\mu_0}{4\pi}\mu_{\mathrm{B}}\big(\vec{I}\cdot\frac{3\vec{e}_r\vec{e}_r^{\mathsf{T}} - 1}{r^3}(\vec{L} + g_s\vec{S}) + \frac{8\pi}{3}\delta^{(3)}(\vec{r})g_s\vec{I}\cdot\vec{S}\big) \tag{2.74}$$

with $g_s = 2.0023\ldots \approx 2$ the g-factor of a free electron.

Both the $1/r^3$ dipolar interaction and the FCI can contribute to the on-site hyperfine coupling of the electronic magnetic moment of an ion and its nucleus. If the unpaired electron is in a non-s-orbital, the dipolar interaction causes an anisotropic on-site hyperfine coupling, whose symmetry is determined by the orientation of the half-filled orbital. Due to intraatomic exchange interactions, an atomic magnetic moment lifts the spin-degeneracy of *all* atomic orbitals of the ion. The inner s-orbitals of a magnetic ion are then expanded or compressed depending on the electron spin. This "core polarisation" causes a non-zero electronic spin-density at the nucleus which is proportional to the spin of the ion. Via this mechanism, the FCI gives an isotropic contribution to the on-site hyperfine coupling [51]. Both contributions may be of the same order of magnitude, as famously seen in Cu^{2+} in various complexes [19] and high-temperature superconductors [107]. If the unpaired electron is in an s-orbital instead, the hyperfine coupling is dominated by the FCI. Typically, the on-site hyperfine coupling with s-electrons is much stronger than that with other electrons [2, p. 192].

The coupling between the electronic moment of a magnetic ion and the nuclear spin of a non-magnetic ligand has two components. First, the nucleus senses the dipolar field of the local moment located at the magnetic ion. This causes an anisotropic interaction between the nuclear spin and the full ionic magnetic moment (i.e. including both spin and orbital contribution). Second, if there is any hybridisation of atomic orbitals (i.e. covalent bonding) between the ligand and the magnetic ion, then the atomic orbitals of the ligand become spin-polarised. The transferred spin-polarisation couples to the nuclear spin by the local hyperfine interaction. This through-bond coupling between the spins of a magnetic ion and a ligand nucleus is called the *transferred hyperfine coupling*. If the s-orbitals of the ligand atom are involved in the covalent bond (which is often the case), then the FCI of the s-electrons dominates the transferred hyperfine coupling. In this case, the transferred hyperfine interaction is approximately isotropic. For a non-magnetic ligand, the hyperfine interaction can then be written in the shorthand form

$$\mathcal{H}_{hf} = \vec{I} \cdot D\vec{m} + A\vec{I} \cdot \vec{S}, \tag{2.75}$$

with the dipolar coupling tensor

$$D = -\frac{\gamma\mu_0}{4\pi} \frac{3\vec{e}_r\vec{e}_r^{\mathsf{T}} - 1}{r^3} \tag{2.76}$$

and the contact interaction strength A. If the half-filled orbital of the magnetic ion hybridises with the ligand orbitals, then A is given by the expression

$$A = \gamma\mu_0 g_s \mu_{\mathrm{B}} \frac{2}{3} |\psi(\vec{r})|^2, \tag{2.77}$$

with $|\psi(\vec{r})|^2$ the density of unpaired electrons at the ligand nucleus. If an empty or full orbital of the magnetic ion hybridises with the ligand orbitals, then A depends on the spin-polarisation of the hybridised orbital due to intraatomic exchange interactions.

NMR shifts due to hyperfine interactions

In metals and magnetic insulators, the hyperfine interactions is usually one of the largest terms in the NMR Hamiltonian. The fluctuations of the electronic magnetic moments give a strong contribution to the nuclear spin relaxation. In a paramagnetic phase, an applied field causes the electronic moments to acquire a non-zero expectation value, which causes a shift of the NMR frequency. In metals, this shift is called the *Knight shift* [70].

In the regime of linear response, the expectation value of the electronic magnetic moment in an applied field $\vec{B}_0$ is given by

$$-\mu_{\mathrm{B}}(\langle\vec{L}\rangle + g_s\langle\vec{S}\rangle) = \chi\vec{B}_0, \tag{2.78}$$

with χ the magnetic susceptibility tensor per atom. Similarly, the expectation value of the electronic spin is

$$\langle \vec{S} \rangle = \chi_s \vec{B}_0 \tag{2.79}$$

with χ_s the spin susceptibility tensor. In a real material, depending on crystallographic symmetries, χ and χ_s may be anisotropic.

In NMR of a non-magnetic ligand, the shift due to hyperfine interactions is thus given by the Hamiltonian

$$\mathcal{H}_{hfs} = \vec{I} \cdot D\chi \vec{B}_0 + A\vec{I} \cdot \chi_s \vec{B}_0. \tag{2.80}$$

Four different shift contributions are conventionally distinguished by their physical origin and symmetry properties. The *contact shift* is the isotropic shift due to the FCI and the isotropic part of χ_s. The *dipolar hyperfine shift* is the shift anisotropy due to dipolar interactions. The *pseudodipolar hyperfine shift* is the shift anisotropy due to the FCI and the anisotropy of χ_s. Finally, the *pseudocontact shift* is the isotropic shift due to dipolar interactions and the anisotropy of χ [3, 88].

2.1.8 Experimental aspects

For all NMR and NQR measurements, the sample is placed in an RF coil, which is part of a resonant circuit, whose resonance frequency is equal to or near the RF carrier frequency used for the experiment. This is necessary in order to achieve the RF field strengths needed to excite the nuclear spins in a few microseconds, as well as to detect the FID signal.

All NMR experiments discussed in this thesis were performed in a Bruker 300 UltraShield superconducting magnet with a room temperature bore, which is capable of producing fields up to 7.07 T. For the sample environment, Oxford Instruments Spectrostat helium flow cryostats were used, inside which the samples were placed in a temperature-controlled helium gas flow. During NMR measurements, the cryostat was mounted inside the bore of the magnet, whereas for NQR measurements it was mounted on a fixture away from any strong magnetic fields.

Measurements at and below room temperature used an insert designed by Bill Pedrini in our lab. A trimmer capacitor connected in series with the RF coil is used to form a tank circuit with tunable resonance frequency. A second trimmer capacitor connected in parallel to the tank circuit is used for matching the impedance at the resonance frequency to 50 Ω. The temperature of the NMR sample was measured by a Cernox resistance thermometer mounted on the insert near the sample.

I have built a special-purpose insert for measurements above room temperature up to 500 K, a photograph of which is shown in figure 2.1. It uses a semirigid coaxial cable with stainless steel outer and inner conductors and

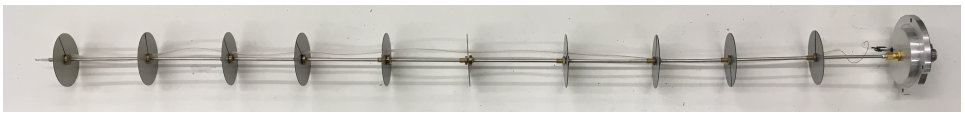

Figure 2.1: Photograph of the high-temperature NMR insert which I have built for measurements from room temperature up to 500 K, based on a stainless steel semirigid coaxial cable. The NMR coil containing the sample can be soldered to the inner and outer conductors. The stainless steel baffles are screwed on to brass baffle holders, which are soldered to the outer conductor. A Pt1000 resistance thermometer is mounted on the baffle closest to the sample and connected to four wires in order to allow four-terminal resistance measurements.

PTFE dielectric bought from Coax Co. Ltd., Japan, which acts simultaneously as an RF transmission line and a structural element. Several circular baffles are installed along the length of the cable, which are used both for centring the insert and to minimise heat transport from the hot sample to the room temperature flange. The only RF element exposed to high temperatures is the RF coil. The resonant circuit is formed by constructing a quarter-wavelength ($\lambda/4$) resonator, or more generally a $((2n+1)/4)\,\lambda$ resonator, using an external phase shifter and additional cable if needed, between the RF coil and an external trimmer capacitor. The resonance frequency can be tuned using the phase shifter, while the impedance can be matched using the trimmer capacitor. A Pt1000 resistance thermometer is mounted on the lowest baffle for monitoring the sample temperature.

For generating RF pulses and detecting FID signals, I have used two NMR spectrometers which were built in our lab. Their design is discussed in Matthias Weller's dissertation [141] and in my Master's thesis [71], respectively.

2.2 Muon Spin Spectroscopy

Like NMR and NQR, muon spin rotation and relaxation (μSR) spectroscopy can locally probe the physical properties of condensed matter. Since the muon has a spin of 1/2, it has a magnetic dipole moment but no electric quadrupole moment. The magnetogyric ratio of the positive muon is $\gamma/2\pi = 135.54\,\mathrm{MHz/T}$ [146] (for the negative muon, γ is equal in magnitude but it is negative). Fully spin-polarised positive muons are injected into the sample and then decay into a positron, electron neutrino, and muon antineutrino after an average lifetime $\tau = 2.197\,\mu\mathrm{s}$ [146]. This decay is mediated by the weak interaction, which violates parity. The positron is emitted preferentially along the direction of the muon spin [30]. Therefore, the muon spin precession and relaxation can be inferred from the positron counts in

multiple detectors mounted in different directions from the sample. The asymmetry of positron counts in μSR is analogous to the FID signal from a single-pulse NMR experiment.

2.2.1 Advantages over NMR

The biggest advantage of μSR over NMR lies in the initial spin polarisation. In μSR, this is nearly 100 % for muons produced by the decay of stopped pions [146]. In NMR and NQR instead, the initial state is given by thermodynamic equilibrium. For a spin 1/2 nucleus, this is given by $\hbar\omega_0/k_\mathrm{B}T$ with ω_0 the Larmor precession frequency. At room temperature in a field of several tesla, this implies a nuclear spin polarisation of some parts per million.

In NMR, there is some receiver deadtime while the RF pulse from the nuclear spin excitation rings down. In "continuous beam" μSR, muons are implanted one by one, therefore the deadtime after implantation is negligibly short [30]. Thus, unlike NMR, μSR measurements are possible even for extremely short relaxation times, e.g. near a continuous phase transition.

In the study of magnetic phase transitions, one often wants to perform measurements in zero field, such that the spin precession is given purely by the internal field due to magnetic order. Just below the phase transition, the order parameter is small, and therefore the internal fields and the Larmor frequency are also small. Therefore, the nuclear spin polarisation is suppressed as ω_0 and the NMR signal decreases proportional to ω_0^2 (see equation 2.65). Zero-field measurements close to a magnetic phase transition are thus impossible in NMR but feasible in μSR. Also NQR measurements may be possible, but they require the presence of quadrupolar nuclei with a large quadrupole coupling constant C_Q, and the experiment is usually more challenging than μSR.

Chapter 3

Physical properties of the $RE\mathrm{NiO_3}$ perovskites

In the phase diagram of the $RE\mathrm{NiO_3}$ perovskites, shown in Figure 3.1, one finds multiple different types of phase transitions: structural, metal–insulator, and magnetic transitions. They all occur in stoichiometric compounds, without requiring any doping or other forms of chemical disorder. This makes the $RE\mathrm{NiO_3}$ a well-suited system for studying the physics of strongly correlated electrons, both experimentally and theoretically.

In this chapter, I will describe the known physical properties of the $RE\mathrm{NiO_3}$ perovskites, starting from their fundamental high-energy properties, and moving across their phase diagram from higher temperature and high-symmetry phases towards lower temperature and lower-symmetry phases. I will not discuss non-universal effects occurring at very low temperature due to the rare-earth ions, such as ordering of the magnetic moments of the rare-earths [120].

3.1 Oxidation states and hybridisation

The formal oxidation states of each atom can be obtained simply by counting electrons. Oxygen atoms are most commonly found in the -II state, while the rare-earths typically adopt the +III state. Therefore, nickel should be in the uncommon +III oxidation state instead of the usual +II state.

This simplistic argument already lets us explain why the hypothetical perovskites $\mathrm{CeNiO_3}$ and $\mathrm{TbNiO_3}$ are not known in the literature. For these two lanthanides, the +IV state is stabilised by an empty or half-filled $4f$ shell, respectively. Reaching the desired oxidation states for all metals would therefore require highly oxidising conditions for nickel but only weakly oxidising conditions for cerium and terbium, which has so far been impossible to achieve simultaneously [31, 9].

We can consider the electronic properties in an (oversimplified) fully

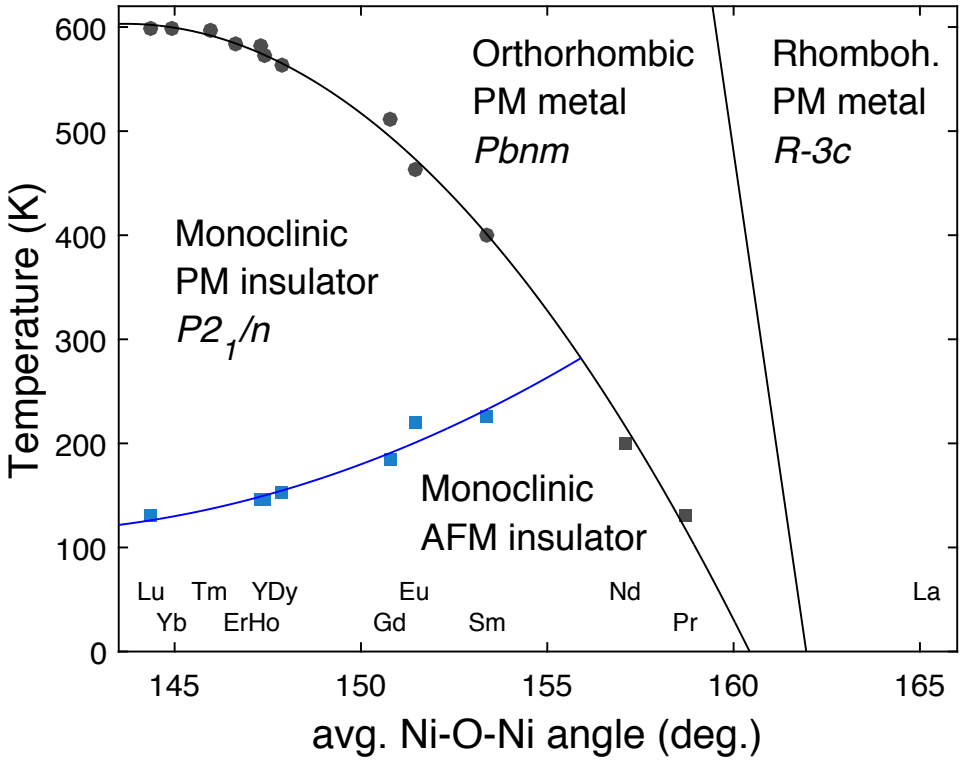

Figure 3.1: Temperature–composition phase diagram of the $RE\mathrm{NiO_3}$ perovskites, using data points from references [11, 90, 7, 9, 8, 101, 10]. If $T_{MI} \neq T_\mathrm{N}$, the magnetic phase transition is continuous, while the metal–insulator transition is only slightly discontinuous [90]. If $T_{MI} = T_\mathrm{N}$, the transition is discontinuous and e.g. the ordered magnetic moment measured in neutron powder diffraction has a large discontinuity at the transition [39]. Also the rhombohedral–orthorhombic structural phase transition is discontinuous [149].

Site	Coordination number	Coordination geometry	Point group
A	12	cuboctahedron	O_h
B	6	octahedron	O_h
X	2 (B) + 4 (A)	square bipyramid	D_{4h}

Table 3.1: Geometric properties of the atomic sites in an ideal perovskite lattice.

ionic picture. The oxide ion has a noble-gas electronic configuration, i.e. it does not have a partially filled shell. Except for Y^{3+}, La^{3+}, and Lu^{3+}, the trivalent rare-earth ions have a partially filled $4f$ shell, which carries a local magnetic moment [69, p. 305ff]. The free Ni^{3+} ion has a configuration of $3d^7$, which is split by an octahedral crystal field into $t_{2g}^6 e_g^1$. This quarter-filled e_g orbital is where the strongly-correlated electron physics happens in these rare-earth nickelates. Note that the low-spin configuration of octahedrally coordinated Ni^{3+} is orbitally degenerate and therefore Jahn–Teller active [60]. However, no cooperative Jahn–Teller distortion is observed in $RE\mathrm{NiO_3}$ experimentally [90].

In the real solid, there is a significant hybridisation of Ni-e_g and O-$2p$ orbitals. The electronic state is therefore a superposition of $3d^7$ and $3d^8\underline{L}$ states ($\underline{L}$: ligand hole), where the latter configuration seems to dominate [90, 26]. In terms of the Zaanen–Sawatzky–Allen classification of the electronic structure of transition metal compounds [147] and its generalisation by Mizokawa [95], the charge-transfer energy is negative [96, 95, 26]. Therefore, in a low energy description, it is usually more appropriate to use a quarter-filled band of e_g-σ^* antibonding states instead of atomic e_g states [144].

3.2 Crystal structures of the metallic phases

The ideal perovskite crystal structure of a material with chemical formula $\mathrm{ABX_3}$ has of a cubic unit cell with the A cation in the corner, the B cation in the body-centre, and the X anions in the face-centres [16], as shown in Figure 3.2. It is often useful to think of the perovskite lattice as a three-dimensional network of corner-sharing $\mathrm{BX_6}$ octahedra, with A ions filling all interstices. If the lattice constant is a, the B–X distance is $a/2$ and the A–X distance is $a/\sqrt{2}$. The space group of this lattice is $Pm\bar{3}m$ (no. 221). The coordination geometry and point group of each atom is given in Table 3.1.

For NMR spectroscopy, knowledge of the point groups provides useful restrictions on the allowed terms in the nuclear spin Hamiltonian. This will be discussed in detail in section 5.1.

A well-known figure of merit for the stability of perovskite phases is the

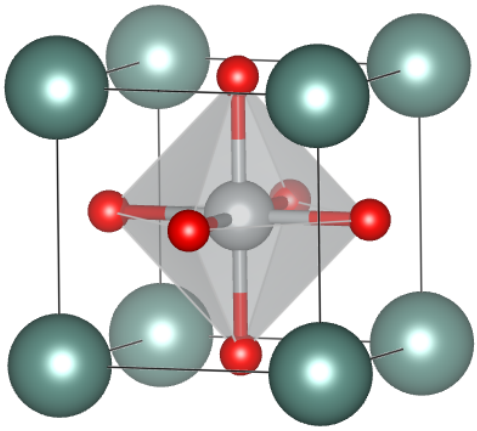

Figure 3.2: Unit cell of the ideal perovskite crystal structure ABX_3, with A in teal, B in grey, and X in red. This figure was created using the crystal structure visualisation software VESTA [97].

tolerance factor, which is defined as

$$t_r = \frac{r(\mathrm{A}) + r(\mathrm{X})}{\sqrt{2}(r(\mathrm{B}) + r(\mathrm{X}))} \quad \text{or} \quad t_d = \frac{d(\mathrm{A{-}X})}{\sqrt{2}d(\mathrm{B{-}X})} \tag{3.1}$$

in terms of the ionic radii r or atomic distances d [47]. Note that for the ideal cubic structure, $t = 1$. Perovskite phases are typically stable for $0.8 \lesssim t \lesssim 1$ [47], but for $t \neq 1$ they can have various lattice distortions.

In all $RE\mathrm{NiO_3}$ perovskites, $t < 1$ because of the small radius of the RE^3+ ions. The ideal cubic structure has been found only for $\mathrm{LaNiO_3}$ at temperatures above 940 °C [103].

The rhombohedral structure shown in figure 3.3 (space group $R\bar{3}c$, no. 167) occurs below this temperature in $\mathrm{LaNiO_3}$ [142, 31], and above 500 °C in $\mathrm{PrNiO_3}$ [55, 56]. In Glazer's notation for distortions of the perovskite structure, this corresponds to the $a^-a^-a^-$ tilt system [45]. This fairly common distorted perovskite structure also occurs e.g. in $\mathrm{NdAlO_3}$

All other metallic $RE\mathrm{NiO_3}$ phases are orthorhombic with space group *Pbnm* (no. 62, standard setting: *Pnma*) [31, 78], with a $a^-a^-b^+$ tilt system in Glazer's notation [45]. The unit cell is shown in figure 3.4. This is the most commonly found distortion of the perovskite lattice [86], and it is found e.g. in oxides such as the mineral perovskite ($\mathrm{CaTiO_3}$) and halides like $\mathrm{CsPbBr_3}$. Note that *Pbnm* is *not* a subgroup of $R\bar{3}c$, and therefore the rhombohedral-to-orthorhombic transition in $\mathrm{PrNiO_3}$ and solid solutions of $RE\mathrm{NiO_3}$ with large rare-earth ions must be discontinuous [149].

The hypothetical perovskite phase $\mathrm{ScNiO_3}$ has never been synthesised, and is probably not stable due to the small radius of the Sc^{3+} ion. Also $\mathrm{PmNiO_3}$ has never been synthesised. The reason for this does not lie in the chemistry of the material but in the strong radioactivity of Pm.

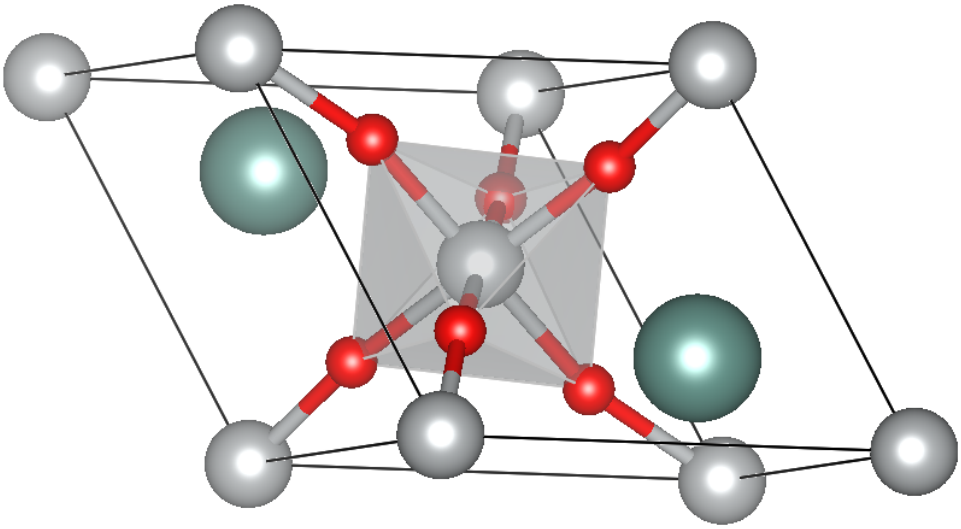

Figure 3.3: Rhombohedral unit cell of $LaNiO_3$, with La in teal, Ni in grey, and O in red. Crystallographic data were taken from reference [41]. Note that the Ni–O–Ni bond angle is no longer 180° due to steric effects, namely the La^{3+} being too small to stabilise the ideal perovskite structure. This figure was created using VESTA [97].

3.3 Electronic behaviour of the metallic phases

The effective model of charge carriers in the metallic phases of $RENiO_3$ is not fully clear. Measurements of the electrical resistivity in bulk polycrystalline $RENiO_3$ have indicated Fermi liquid behaviour ($\rho(T) = \rho_0 + aT^n$, $n = 2$) in $LaNiO_3$, but already in $PrNiO_3$ non-Fermi liquid behaviour ($n < 2$) has been observed [150, 151]. Experiments in epitaxial films have found "bad metal" transport behaviour, i.e. a resistivity which does not saturate at the Mott–Ioffe–Regel limit, in $SmNiO_3$ and $NdNiO_3$ [62, 93].

The magnetic susceptibility of $LaNiO_3$ is known to be dominated by Pauli paramagnetism [48]. For other compounds, large contributions of the lanthanide ion or impurities have made it challenging to obtain measurements of the magnetic susceptibility of the e_g-σ^* electron system. In $SmNiO_3$, after subtraction of the contribution of Sm^{3+}, Curie paramagnetism was found with a slightly reduced effective magnetic moment compared to the insulating phase (1.5 instead of 1.7 μ_B) [110]. This is consistent with a "bad-metal" picture, where the e_g-σ^* electrons have a partially localised character.

The Fermi surface of $LaNiO_3$ is known, from both theory as well as angle-resolved photoemission spectroscopy, to consist of an electron pocket at the Brillouin zone centre and a hole pocket at the Brillouin zone corner [50, 32].

NMR is able to address the question of the nature of the metallic phase

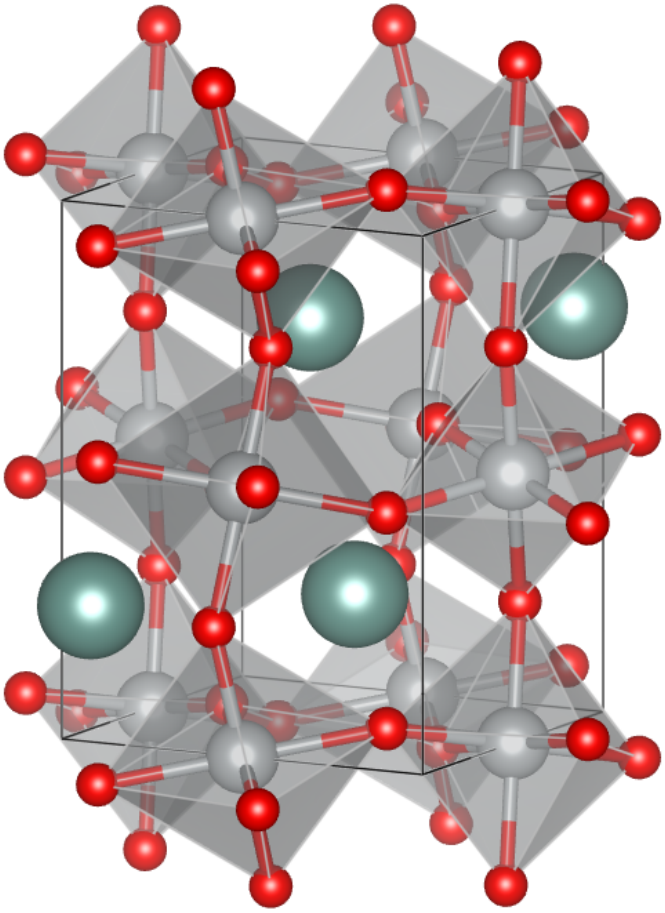

Figure 3.4: Orthorhombic (*Pbnm*) crystal structure of $YNiO_3$ at 653 K [8]. This figure was created using VESTA [97].

both by measurements of the Knight shift and the relaxation rate. The Knight shift probes the spin susceptibility, and thus its temperature dependence can distinguish between Pauli and Curie paramagnetism. The relaxation rate in a Fermi liquid should be approximately linear in temperature and related to the Knight shift via the Korringa relation [73]. If the nuclear spin relaxation occurs due to localised magnetic moments, the relaxation rate should be approximately constant in temperature [100].

3.4 The insulating phases

All $RE\mathrm{NiO_3}$ compounds except for $\mathrm{LaNiO_3}$ have a metal–insulator transition (MIT) at a temperature T_{MI}, which is as high as 600 K for the smallest rare-earth ions. For RE = Sm – Lu and Y, the MIT is only weakly discontinuous, and there is a continuous antiferromagnetic phase transition at a lower temperature. For $\mathrm{PrNiO_3}$ and $\mathrm{NdNiO_3}$ instead, both the MIT and the magnetic transition occur simultaneously, resulting in a discontinuous phase transition from a metallic paramagnet to an insulating antiferromagnet.

3.4.1 Electronic and structural properties

In the insulating phase, the nickel oxide octahedra become inequivalent as a breathing mode freezes in at the MIT. A superstructure of alternating expanded and compressed octahedra occurs at the wavevector $k_{pc} = (1/2, 1/2, 1/2)$ with respect to the ideal (pseudo-)cubic unit cell, i.e. the superstructure forms a rocksalt-like pattern. The insulating $RE\mathrm{NiO_3}$ adopt a monoclinic crystal structure, which has been characterised by the space group $P2_1/n$. This space group is typical for double perovskites with chemical formula $\mathrm{A_2BB'O_6}$ [137], and is therefore suggestive of differences in the electronic structure of large and small octahedra.

The physical mechanism of this metal–insulator transition has not been fully understood theoretically. The first experiments were interpreted in terms of ordering of the nickel $d_{x^2-y^2}$ and $d_{3z^2-r^2}$ orbitals [119]. Early theories suggested instead a complete charge disproportionation, i.e. that the large and small octahedra contain $\mathrm{Ni^{2+}}$ and $\mathrm{Ni^{4+}}$ ions, respectively [87]. Alternative models also suggested spin-density wave behaviour, especially for $\mathrm{PrNiO_3}$ and $\mathrm{NdNiO_3}$ [79]. Later "DFT + DMFT" (density functional theory plus dynamical mean field theory) calculations [105] have instead suggested a "site-selective Mott transition" [104]. Here, all nickel ions are divalent, but in the small octahedra, ligand holes and d-electrons are bound together in a singlet state, whereas the d electrons in the large octahedra from a Mott-insulating state.

A low-energy model containing only the e_g-σ^* bands with on-site Coulomb repulsion U and Hund's-rule coupling J_H has been published in

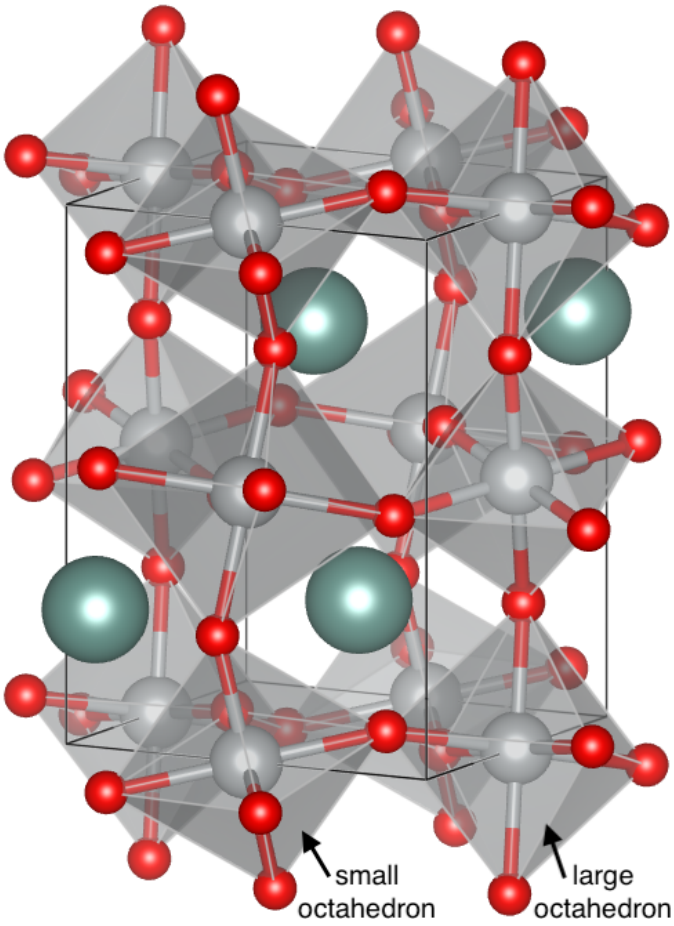

Figure 3.5: Monoclinic ($P2_1/n$) crystal structure of $YNiO_3$ at 513 K [8]. While in the *Pbnm* structure all octahedra were equivalent, here there is an alternating pattern of large and small octahedra. This figure was created using VESTA [97].

reference [135]. Here, the covalency of the Ni−O bonds is found to be modulated due to spontaneous symmetry breaking for intermediate U and large J_{H}. Thus, the "site-selective Mott" or "bond disproportionated insulator" (BDI) phase is an instability of the correlated electron system in this model.

Recently, the study of a Landau theory model of the structural distortions in the $RE\mathrm{NiO_3}$ system has emphasised the importance of the lattice in the MIT [91].

Over the last years, experiment and theory have converged on identifying the insulating state as a BDI with a lattice distortion [26]. However, as this section has illustrated, there is no complete agreement on the microscopic origin of the MIT. In fact, every degree of freedom in the system — orbital, spin, charge, and lattice — has already been suggested to drive the MIT.

The electric quadrupole moment of nuclei with spin $I > 1/2$ can be used to sense charge redistribution in a material, which will provide insight into the nature of the insulating state. Since the NMR relaxation rate probes the low-frequency fluctuations in a material, it can provide useful insight in the presence and identity of critical fluctuations at a phase transition.

3.4.2 Magnetic order

Below the magnetic phase transition, neutron powder diffraction experiments have found antiferromagnetic order with four nickel atoms per period of the magnetic structure. The propagation vector of the magnetic structure respective to the orthorhombic or monoclinic structure is $k = (1/2, 0, 1/2)$, which corresponds to $k_{pc} = (1/4, 1/4, 1/4)$ w.r.t. the ideal (pseudo-)cubic perovskite unit cell [39]. The exact magnetic structure of bulk $RE\mathrm{NiO_3}$ is not yet agreed upon, and may be either collinear or non-collinear. However, every possible magnetic order with this propagation vector and non-zero ordered moments on every Ni site breaks the inversion symmetry of the monoclinic space group $P2_1/n$, and may thus induce "improper" ferroelectricity [44, 28]. Experiments have been unable to measure any ferroelectric polarisation in $RE\mathrm{NiO_3}$ thus far [25, 26].

NMR relaxation measurements in the AF phase, which will be presented later in this thesis, have revealed the presence of a large gap in the magnetic excitation spectrum. Since no large single-crystals of $RE\mathrm{NiO_3}$ have been available (see section 3.5), no inelastic neutron scattering measurements of the magnetic excitations in these materials have been performed. Recent resonant inelastic X-ray scattering experiments on nickelate films have also found a gapped magnetic excitation spectrum [85, 36], in qualitative agreement with my NMR results.

3.5 Unavailability of single-crystalline samples

Historically, all known synthesis pathways for bulk $RE\mathrm{NiO_3}$ were unable to produce large single-crystals [90, 25]. This is why powder samples were used for all experiments discussed in this thesis.

Recently, two groups claim to have synthesised large crystals of $\mathrm{LaNiO_3}$ [148, 49]. In one paper, the reported physical properties of the single-crystalline $\mathrm{LaNiO_3}$ sample are in good agreement with previous experiments on polycrystals and powder samples [148]. The other paper, however, reports twinned crystals which order antiferromagnetically at a temperature of 157 K [49], which clearly contradicts previous studies of $\mathrm{LaNiO_3}$. No large single-crystals are available for other $RE\mathrm{NiO_3}$ materials, where one could study the MIT.

Subsequent experiments have shown that this antiferromagnetic order can be reproduced by reducing high-quality single-crystals in a $\mathrm{H_2/N_2}$ atmosphere. Inclusions of two oxygen-deficient phases were found, $\mathrm{LaNiO_{2.75}}$ and $\mathrm{LaNiO_{2.5}}$, where the former is a ferromagnet with $T_\mathrm{C} \approx 225\,\mathrm{K}$ and the latter an antiferromagnet with $T_\mathrm{N} \approx 152\,\mathrm{K}$ [139]. Thus, the antiferromagnetic order observed in "$\mathrm{LaNiO_3}$" almost certainly originates from a $\mathrm{LaNiO_{2.5}}$ impurity phase. This is consistent with the NMR measurements presented in section 5.4, which exclude the presence of magnetic order in this temperature range in $\mathrm{LaNiO_3}$ powder.

Instead of using bulk material, many recent experimental studies have focussed on epitaxial $RE\mathrm{NiO_3}$ films grown on other perovskite oxides [92, 26]. I will not review the physics of nickelate heterostructures, as it is not directly relevant to this thesis. However, it is noteworthy that many physical properties of $RE\mathrm{NiO_3}$ films depend strongly on growth direction and epitaxial strain [26].

Chapter 4

Spin–lattice relaxation in quadrupolar NMR

In this chapter, I will apply the Wangsness–Bloch–Redfield theory [140, 20, 21, 118] to describe nuclear spin relaxation due to rapidly fluctuating hyperfine fields and rapidly fluctuating electric field gradients. The results from this chapter will be needed for the discussion of experimental relaxation data in later chapters. The functional form of the inversion recovery signal under both non-selective and selective excitation and detection conditions, which are mostly already known in the literature (see e.g. references [53, 136]), will be reproduced for both relaxation mechanisms. Next, the functional form of the inversion recovery signal from quadrupolar nuclei in an antiferromagnetic powder due to hyperfine relaxation is calculated. Then, the contribution of spin–lattice relaxation to the decay of the spin-echo of the central transition of a half-integer spin nucleus will be derived for isotropic magnetic relaxation. Finally, some applications of the ideas described in this chapter to NQR will be outlined. For this purpose, I will first introduce the notion of superoperators and Liouville space, find the irreducible representations of $\mathfrak{so}(3)$ in Liouville space, and give a derivation of Wangsness–Bloch–Redfield theory. While the physical principles discuss in this chapter are quite general, all final results assume isotropic fluctuations.

4.1 Liouville space and superoperators

A natural description of NMR relaxation is obtained using superoperators [33, p. 15ff], i.e. vector space endomorphisms of Liouville space $\mathbb{L}$, which is related to the Hilbert space $\mathbb{H}$ of a quantum system as $\mathbb{L} = \mathbb{H} \otimes \mathbb{H}^*$ [77]. Note that $\mathbb{L}$ is naturally isomorphic to the space of endomorphisms of $\mathbb{H}$. Some useful algebraic properties relating the Hilbert space $\mathbb{H}$ of a quantum system, its Liouville space $\mathbb{L}$, and the space of its superoperators $\operatorname{End}\mathbb{L}$ can be found in table 4.1.

Vector space	Orthonormal basis vectors	Inner product
$\mathbb{H}$	$\lvert\psi_i\rangle$	$\langle\phi,\psi\rangle = \langle\phi\lvert\psi\rangle$
$\mathbb{L} = \mathbb{H}\otimes\mathbb{H}^* \cong \operatorname{End}\mathbb{H}$	$\big\lvert\, \lvert\psi_i\rangle\langle\psi_j\rvert \,\big\rangle$	$\langle\rho,\sigma\rangle = \operatorname{tr}\rho^\dagger\sigma$
$\operatorname{End}\mathbb{L} \cong \mathbb{L}\otimes\mathbb{L}^*$	$\big\lvert\, \lvert\psi_i\rangle\langle\psi_j\rvert \,\big\rangle\big\langle\, \lvert\psi_k\rangle\langle\psi_l\rvert \,\big\rvert$	$\langle\hat{A},\hat{B}\rangle$

Table 4.1: The different vector spaces relevant to NMR relaxation theory.

Notation: Superoperators will be denoted with hats ($\hat{S}$). When a matrix M is considered as a vector in Liouville space, this may be emphasised by writing $\lvert M\rangle$. An operator $A \in \operatorname{End}\mathbb{H}$ can be raised to a superoperator $\hat{A} \in \operatorname{End}\mathbb{L}$ whose action is defined as a commutator $\hat{A}\lvert M\rangle = [A, M]$ [33, p. 20].

I will frequently make use of the fact that raising an operator to a superoperator commutes with taking the Hermitian conjugate:

$$(\hat{A})^\dagger = \widehat{A^\dagger}. \tag{4.1}$$

This superoperator identity is easily proven by showing that the matrix elements are identical:

$$\begin{aligned}\langle\rho\rvert(\hat{A})^\dagger\lvert\sigma\rangle &= \langle\sigma\rvert\hat{A}\lvert\rho\rangle^* = \operatorname{tr}(\sigma^\dagger[A,\rho])^* = \operatorname{tr}([\rho^\dagger, A^\dagger]\sigma),\\ &= \operatorname{tr}(\rho^\dagger A^\dagger\sigma - A^\dagger\rho^\dagger\sigma)\end{aligned} \tag{4.2}$$

$$\langle\rho\rvert\widehat{A^\dagger}\lvert\sigma\rangle = \operatorname{tr}(\rho^\dagger[A^\dagger,\sigma]) = \operatorname{tr}(\rho^\dagger A^\dagger\sigma - \rho^\dagger\sigma A^\dagger) = \operatorname{tr}(\rho^\dagger A^\dagger\sigma - A^\dagger\rho^\dagger\sigma). \tag{4.3}$$

4.2 Representation theory of $\mathfrak{so}(3)$ in Liouville space

Let R_H be the Lie algebra representation of $\mathfrak{so}(3)$ on $\mathbb{H}$. In this section, abstract Lie algebra elements are denoted by j and most representations are invoked explicitly, e.g. instead of writing I_α for the nuclear spin operator I may write $R_H(j_\alpha)$ in this section.

Let R_L be the representation of $\mathfrak{so}(3)$ on $\mathbb{L}$. The action of $g \in \mathfrak{so}(3)$ on $\sigma \in \mathbb{L}$ is given by

$$R_L(g)\sigma = [R_H(g), \sigma]. \tag{4.4}$$

Applying this definition to a single spin I, one can see that

$$\begin{aligned}R_L(j_z)\big\lvert\, \lvert m\rangle\langle m'\rvert \,\big\rangle &= R_H(j_z)\lvert m\rangle\langle m'\rvert - \lvert m\rangle\langle m'\rvert R_H(j_z)\\ &= (m-m')\lvert m\rangle\langle m'\rvert\end{aligned} \tag{4.5}$$

$$\begin{aligned}R_L(j_\pm)\big\lvert\, \lvert m\rangle\langle m'\rvert \,\big\rangle &= R_H(j_\pm)\lvert m\rangle\langle m'\rvert - \lvert m\rangle\langle m'\rvert R_H(j_\pm)\\ &= \sqrt{I(I+1) - m(m\pm1)}\,\lvert m\pm1\rangle\langle m'\rvert\\ &\quad - \sqrt{I(I+1) - m'(m'\mp1)}\,\lvert m\rangle\langle m'\mp1\rvert\end{aligned} \tag{4.6}$$

Let $\mathfrak{D}_j$ be the $(2j+1)$-dimensional ('spin j') irreducible representation of the Lie algebra $\mathfrak{so}(3)$. Then, the Hilbert and Liouville spaces of a single spin I can be decomposed in terms of irreps of $\mathfrak{so}(3)$:

$$\mathbb{H} \cong \mathfrak{D}_I, \tag{4.7}$$

$$\mathbb{L} = \mathbb{H} \otimes \mathbb{H}^* \cong \mathfrak{D}_I \otimes \mathfrak{D}_I^* \cong \mathfrak{D}_0 \oplus \mathfrak{D}_1 \oplus \cdots \oplus \mathfrak{D}_{2I}. \tag{4.8}$$

I will decompose $\mathbb{L}$ explicitly by constructing the new orthonormal basis vectors $|\rho_{kq}\rangle \in \mathfrak{D}_k$. The defining properties of $|\rho_{kq}\rangle$ (up to normalisation) are

$$R_L(j_z)\,|\rho_{kq}\rangle = q\,|\rho_{kq}\rangle\,, \quad q = -k, -k+1, \ldots k \tag{4.9}$$

$$R_L(j_\pm)\,|\rho_{kq}\rangle = \sqrt{k(k+1) - q(q\pm 1)}\,|\rho_{k,q\pm 1}\rangle \tag{4.10}$$

Note that equations 4.5 and 4.9 imply that the subspace of diagonal matrices is spanned by $|\rho_{k0}\rangle$. This will be important later when discussing nuclear spin relaxation.

The highest weight state of the irrep $\mathfrak{D}_k$ is given by $|\rho_{kk}\rangle \propto |R_H(j_+)^k\rangle$:

$$\begin{aligned} R_L(j_z)\,|R_H(j_+)^k\rangle &= [R_H(j_z), R_H(j_+)^k] \\ &= R_H(j_z)R_H(j_+)^k - R_H(j_+)^k R_H(j_z) \\ &= \sum_{l=0}^{k-1} R_H(j_+)^l [R_H(j_z), R_H(j_+)] R_H(j_+)^{k-1-l} \\ &= \sum_{l=0}^{k-1} R_H(j_+)^l R_H(j_+) R_H(j_+)^{k-1-l} \\ &= kR_H(j_+)^k = k\,|R_H(j_+)^k\rangle \end{aligned} \tag{4.11}$$

$$R_L(j_+)\,|R_H(j_+)^k\rangle = [R_H(j_+), R_H(j_+)^k] = 0 \tag{4.12}$$

The entire irrep can be constructed iteratively by application of the lowering operator $R_L(j_-)$.

4.2.1 Spherical tensor operators

When decomposing operators into irreps, it is common in NMR to re-write them in terms of the orthogonal basis set of spherical tensor operators $T_{kq} \in \operatorname{End}\mathbb{H}$. On the Hilbert space of a single spin I, they are most commonly defined as [24]

$$T_{kk} = \big(-\sqrt{\frac{1}{2}}I_+\big)^k \tag{4.13}$$

$$T_{kq} = \frac{1}{\sqrt{k(k+1) - q(q+1)}}[I_-, T_{k,q+1}], \quad q = -k, -k+1, \ldots, k-1. \tag{4.14}$$

A comparison with the previous section shows that the T_{kq} span the irreps of $\mathfrak{so}(3)$ on $\operatorname{End}\mathbb{H} \cong \mathbb{L}$. Using the definition, we obtain the following expressions for the first few tensor operators:

$$\begin{aligned} T_{0,0} &= 1 \\ T_{1,0} &= I_z \\ T_{1,\pm1} &= \mp\sqrt{\frac{1}{2}} I_\pm \\ T_{2,0} &= \sqrt{\frac{1}{6}}(3I_z^2 - I(I+1)) \\ T_{2,\pm1} &= \mp\frac{1}{2}(I_z I_\pm + I_\pm I_z) \\ T_{2,\pm2} &= \frac{1}{2} I_\pm^2. \end{aligned} \tag{4.15}$$

In the subsequent sections, we will frequently make use of the identity

$$T_{k,q}^\dagger = (-1)^q T_{k,-q}. \tag{4.16}$$

I will use T_{kq} not only to decompose operators, but also to fix the phase of the $|\rho_{kq}\rangle$ as

$$|\rho_{kq}\rangle = \frac{|T_{kq}\rangle}{\sqrt{\langle T_{kq}|T_{kq}\rangle}}. \tag{4.17}$$

4.3 Wangsness–Bloch–Redfield relaxation theory

4.3.1 Derivation of the equation of motion

The evolution of a density matrix ρ under the Hamiltonian $\mathcal{H}$ is given by the equation of motion

$$\frac{\mathrm{d}\rho}{\mathrm{d}t} = -i[\mathcal{H}, \rho], \tag{4.18}$$

which has the solution

$$\rho(t_0 + \Delta t) = \mathrm{e}^{-i\mathcal{H}\Delta t}\rho(t_0)\mathrm{e}^{i\mathcal{H}\Delta t} \tag{4.19}$$

for a time-independent Hamiltonian.

Instead of considering an isolated quantum system, let us now consider the nuclear spin subsystem of a real material. Let σ be the reduced density matrix of the nuclear spin system. The spins evolve under the time-independent average (or "mean-field") Hamiltonian $\mathcal{H} = \mathcal{H}_0$, and a stochastic Hamiltonian $\mathcal{H}_{SLR}(t)$ with ensemble average $\overline{\mathcal{H}_{SLR}(t)} = 0$ which encodes the dynamics of the other degrees of freedom of the material (the "lattice" in NMR parlance). The equation of motion for the spin system is now

$$\frac{\mathrm{d}\sigma}{\mathrm{d}t} = -i[\mathcal{H}_0 + \mathcal{H}_{SLR}(t), \sigma]. \tag{4.20}$$

Let us define the interaction frame with respect to $\mathcal{H}_0$ (c.f. [125, p. 330]):

$$\widetilde{A}(t) = \mathrm{e}^{i\mathcal{H}_0 t} A(t) \mathrm{e}^{-i\mathcal{H}_0 t}. \tag{4.21}$$

Then, equation 4.20 can be rewritten in the interaction frame:

$$\frac{\mathrm{d}\widetilde{\sigma}}{\mathrm{d}t} = -i[\widetilde{\mathcal{H}}_{SLR}(t), \widetilde{\sigma}(t)]. \tag{4.22}$$

Let Δt be some timescale on which the evolution under $\widetilde{\mathcal{H}}_{SLR}$ may be described by second-order perturbation theory, i.e. $|\mathcal{H}_{SLR}\Delta t| \ll 1$. Assume that Δt is much larger than the correlation time of the fluctuations τ_c but much smaller than the timescale of experimental observations t, i.e. $\tau_c \ll \Delta t \ll t$. Note that these two assumptions together give the implicit physical assumption that $|\mathcal{H}_{SLR}\tau_c| \ll 1$.

The solution of equation 4.22 to second order in perturbation theory in $\mathcal{H}_{SLR}$ is

$$\begin{aligned} \widetilde{\sigma}(t_0 + \Delta t) = \widetilde{\sigma}(t_0) - i \int_{t_0}^{t_0+\Delta t} \mathrm{d}t' \, [\widetilde{\mathcal{H}}_{SLR}(t'), \widetilde{\sigma}(t_0)] \\ - \int_{t_0}^{t_0+\Delta t} \mathrm{d}t' \int_{t_0}^{t'} \mathrm{d}t'' \, [\widetilde{\mathcal{H}}_{SLR}(t'), [\widetilde{\mathcal{H}}_{SLR}(t''), \widetilde{\sigma}(t_0)]]. \end{aligned} \tag{4.23}$$

Since the experiment is carried out with a macroscopic sample, we take the ensemble average of the stochastic fluctuations, which we denote by an overbar, and obtain

$$\begin{aligned} \overline{\widetilde{\sigma}(t_0 + \Delta t) - \widetilde{\sigma}(t_0)} = -i \overline{\int_{t_0}^{t_0+\Delta t} \mathrm{d}t' \, [\widetilde{\mathcal{H}}_{SLR}(t'), \widetilde{\sigma}(t_0)]} \\ - \overline{\int_{t_0}^{t_0+\Delta t} \mathrm{d}t' \int_{t_0}^{t'} \mathrm{d}t'' \, [\widetilde{\mathcal{H}}_{SLR}(t'), [\widetilde{\mathcal{H}}_{SLR}(t''), \widetilde{\sigma}(t_0)]]}. \end{aligned} \tag{4.24}$$

Since $|\mathcal{H}_{SLR}\tau_c| \ll 1$ is assumed, $\widetilde{\sigma}$ does not change much on the timescale of τ_c. Therefore, $\widetilde{\sigma}$ cannot contain information on the correlations of $\widetilde{\mathcal{H}}_{SLR}$ and the ensemble averages can be separated. Furthermore, since $\tau_c \ll \Delta t$, the outermost time-integral can be taken outside the ensemble average using the ergodic hypothesis:

$$\begin{aligned} \overline{\widetilde{\sigma}(t_0 + \Delta t) - \widetilde{\sigma}(t_0)} = -i \int_{t_0}^{t_0+\Delta t} \mathrm{d}t' \, [\overline{\widetilde{\mathcal{H}}_{SLR}(t')}, \overline{\widetilde{\sigma}(t_0)}] \\ - \int_{t_0}^{t_0+\Delta t} \mathrm{d}t' \, \overline{\int_{t_0}^{t'} \mathrm{d}t'' \, [\widetilde{\mathcal{H}}_{SLR}(t'), [\widetilde{\mathcal{H}}_{SLR}(t''), \overline{\widetilde{\sigma}(t_0)}]]}. \end{aligned} \tag{4.25}$$

By construction, $\overline{\mathcal{H}_{SLR}} = 0$, thus the linear term drops out. We are left with

$$\begin{aligned}\overline{\widetilde{\sigma}(t_0+\Delta t) - \widetilde{\sigma}(t_0)} &= -\int_{t_0}^{t_0+\Delta t} \mathrm{d}t' \overline{\int_{t_0}^{t'} \mathrm{d}t''[\widetilde{\mathcal{H}}_{SLR}(t'), [\widetilde{\mathcal{H}}_{SLR}(t''), \overline{\widetilde{\sigma}(t_0)}]]} \\ &= -\int_{t_0}^{t_0+\Delta t} \mathrm{d}t' \overline{\int_{t_0}^{t'} \mathrm{d}t'' \hat{\widetilde{\mathcal{H}}}_{SLR}(t')\hat{\widetilde{\mathcal{H}}}_{SLR}(t'')}\overline{\widetilde{\sigma}(t_0)}.\end{aligned} \tag{4.26}$$

Since the integral over t'' decays on a timescale of $\tau_c \ll \Delta t$, we can extend the integral to infinity. Using the more convenient superoperator notation lets us write

$$\int_{t_0}^{t'} \mathrm{d}t'' \hat{\widetilde{\mathcal{H}}}_{SLR}(t')\hat{\widetilde{\mathcal{H}}}_{SLR}(t'') \approx \int_0^{\infty} \mathrm{d}\tau \hat{\widetilde{\mathcal{H}}}_{SLR}(\tau)\hat{\widetilde{\mathcal{H}}}_{SLR}(0). \tag{4.27}$$

The matrix elements of this superoperator are Fourier transforms of the two-time correlation functions of the stochastic fluctuations, evaluated at frequencies corresponding to the differences between eigenvalues of the average Hamiltonian $\mathcal{H}_0$.

Let us simplify the problem further by assuming that the correlations of the fluctuations are frequency-independent over the relevant frequency range. This corresponds to the physical assumption that the correlation time is much shorter than the inverse resonance frequency (in the laboratory frame) $2\pi/\omega$, i.e. $\omega\tau_c \ll 1$, also known as *extreme narrowing* [33, p. 52f].

In order to evaluate the integral 4.27, we need to assume some form for the two-time correlation functions. Let us assume an exponential form with time constant τ_c. We can then calculate

$$\begin{aligned}\int_0^{\infty} \mathrm{d}\tau \hat{\widetilde{\mathcal{H}}}_{SLR}(\tau)\hat{\widetilde{\mathcal{H}}}_{SLR}(0) &= \int_0^{\infty} \mathrm{d}\tau \overline{\left(\hat{\widetilde{\mathcal{H}}}_{SLR}(0)\right)^2} \exp(-\frac{\tau}{\tau_c}) \\ &= \overline{\left(\hat{\widetilde{\mathcal{H}}}_{SLR}(0)\right)^2} \tau_c.\end{aligned} \tag{4.28}$$

Plugging this expression back into equation 4.26 then gives

$$\overline{\widetilde{\sigma}(t_0+\Delta t) - \widetilde{\sigma}(t_0)} = -\tau_c \int_{t_0}^{t_0+\Delta t} \mathrm{d}t' \overline{[\widetilde{\mathcal{H}}_{SLR}(t'), [\widetilde{\mathcal{H}}_{SLR}(t'), \overline{\widetilde{\sigma}(t_0)}]]}. \tag{4.29}$$

In order to describe the system over a timescale $t \gg \Delta t$, we may now take the limit $\Delta t \to 0$ and obtain the equations of motion as a differential equation:

$$\frac{\mathrm{d}\overline{\widetilde{\sigma}}}{\mathrm{d}t} = -\tau_c \overline{[\widetilde{\mathcal{H}}_{SLR}(t), [\widetilde{\mathcal{H}}_{SLR}(t), \overline{\widetilde{\sigma}(t)}]]}. \tag{4.30}$$

Finally, we must account for the fact that we did not use the full density matrix ρ of the whole (spin + lattice) system, but only the reduced density

matrix σ of the spin system. If the lattice is in thermal equilibrium and the spin-lattice interaction may be treated as a perturbation, it has been shown in ref. [118] that one must simply subtract the spin density matrix at thermal equilibrium σ_0 from the spin density matrix in equation 4.30:

$$\frac{\mathrm{d}\overline{\widetilde{\sigma}}}{\mathrm{d}t} = -\tau_c\overline{[\widetilde{\mathcal{H}}_{SLR}(t), [\widetilde{\mathcal{H}}_{SLR}(t), (\overline{\widetilde{\sigma}(t)} - \sigma_0)]]}. \tag{4.31}$$

Now, we can return from the interaction frame back to the laboratory frame:

$$\frac{\mathrm{d}\overline{\sigma}}{\mathrm{d}t} = -i[\mathcal{H}_0, \overline{\sigma(t)}] - \tau_c\overline{[\mathcal{H}_{SLR}(t), [\mathcal{H}_{SLR}(t), (\overline{\sigma(t)} - \sigma_0)]]}. \tag{4.32}$$

This is an equation of motion in Liouville space, and can be written in terms of superoperators as

$$\frac{\mathrm{d}}{\mathrm{d}t}|\overline{\sigma}\rangle = \hat{\mathcal{L}}(|\overline{\sigma}\rangle - |\sigma_0\rangle) \tag{4.33}$$

$$\hat{\mathcal{L}} = -i\hat{\mathcal{H}}_0 - \hat{\Gamma} \tag{4.34}$$

$$\hat{\Gamma} = \tau_c\overline{\hat{\mathcal{H}}_{SLR}(t)^2} \tag{4.35}$$

with $\hat{\mathcal{L}}$ the Liouvillian superoperator, $\hat{\Gamma}$ the relaxation superoperator, and we used that $[\mathcal{H}_0, \sigma_0] = 0$. Note that $\overline{\hat{\mathcal{H}}_{SLR}(t)^2}$ is actually time-independent due to the ensemble average, thus $\hat{\Gamma}$ is time-independent.

If we remove the assumption of an exponential two-time correlation function (which gave us equation 4.28) but keep the approximation of frequency-independent correlations, the relaxation superoperator can instead be written in the slightly more general form

$$\hat{\Gamma} = \overline{\int_0^\infty \mathrm{d}\tau\, \hat{\mathcal{H}}_{SLR}(\tau)\hat{\mathcal{H}}_{SLR}(0)}, \tag{4.36}$$

which is probably the most useful form for typical applications of NMR and NQR relaxation in solid state physics.

4.3.2 Relaxation superoperator for magnetic relaxation

If relaxation occurs via a fluctuating magnetic field $\vec{B}^{fluc}(t)$ satisfying the assumptions of WBR theory (short correlation time, zero average), then the spin–lattice relaxation Hamiltonian is given by

$$\mathcal{H}_{SLR}^{mag}(t) = -\gamma\vec{I}\cdot\vec{B}^{fluc}(t) \tag{4.37}$$

and the relaxation superoperator is

$$\begin{aligned}\hat{\Gamma}^{mag} &= \int_0^\infty \mathrm{d}\tau\, \overline{\hat{\mathcal{H}}_{SLR}^{mag}(t+\tau)\hat{\mathcal{H}}_{SLR}^{mag}(t)} \\ &= \gamma^2 \int_0^\infty \mathrm{d}\tau\, \overline{(\hat{\vec{I}}\cdot\vec{B}^{fluc}(t+\tau))(\hat{\vec{I}}\cdot\vec{B}^{fluc}(t))} \\ &= \gamma^2 \sum_{\alpha,\beta=x,y,z} \hat{I}_\alpha \hat{I}_\beta \int_0^\infty \mathrm{d}\tau\, \overline{B_\alpha^{fluc}(t+\tau)B_\beta^{fluc}(t)}.\end{aligned} \tag{4.38}$$

In our case, the dominant physical origin of this fluctuating magnetic field is the isotropic Fermi contact between the nuclear spins and either conduction electron spins or ionic spins $\vec{S}$, i.e. $\vec{B}^{fluc}(t) = -A/\gamma(\vec{S}(t) - \langle\vec{S}\rangle)$. In order to simplify the case of a powder sample, let us assume that all nuclei experience the same fluctuations independent of orientation, i.e. that the fluctuations are isotropic:

$$\gamma^2 \int_0^\infty \mathrm{d}\tau\, \overline{B_\alpha^{fluc}(t+\tau)B_\beta^{fluc}(t)} = W\delta_{\alpha\beta}. \tag{4.39}$$

If the fluctuating field $\vec{B}^{fluc}$ originates from electronic magnetic moments at temperature T, then the fluctuation–dissipation theorem allows us to rewrite the correlation function in equation 4.39 in terms of the dynamic magnetic susceptibility [138, p. 100f]:

$$W \propto \lim_{\omega\to 0} T \sum_{\vec{q}} A(\vec{q})^2 \frac{\chi''(\vec{q},\omega)}{\omega}, \tag{4.40}$$

with $\vec{q}$ the wavevector, ω the NMR frequency, $A(\vec{q})$ the wavevector-dependent coupling between nuclear spins and electronic moments (if each nucleus couples to multiple magnetic moments), and $\chi''(\vec{q},\omega)$ the imaginary part of the dynamical magnetic susceptibility.

The assumption of isotropic fluctuations is valid if there is no magnetic order, the electronic spin Hamiltonian is (approximately) rotationally invariant, and the applied field is much smaller than the saturation field. The resulting formulae also apply in an antiferromagnetic phase even if the internal field is strong compared to the NMR bandwidth, if we assume that all nuclei remaining within the bandwidth experience similar fluctuations.

Thus, the relaxation superoperator for isotropic magnetic fluctuations may be written in the following equivalent forms:

$$\begin{aligned}\hat{\Gamma}_{iso}^{mag} &= W \sum_{\alpha=x,y,z} \hat{I}_\alpha \cdot \hat{I}_\alpha = W\hat{\vec{I}}\cdot\hat{\vec{I}} \\ &= W\left(\frac{\hat{I}_+\hat{I}_- + \hat{I}_-\hat{I}_+}{2} + \hat{I}_z\hat{I}_z\right) \\ &= W\sum_{q=-1}^{1} (-1)^q \hat{T}_{1,-q}\hat{T}_{1,q}.\end{aligned} \tag{4.41}$$

Note that $\hat{\Gamma}_{iso}^{mag}$ is proportional to the Casimir invariant of $\mathfrak{so}(3)$ on $\mathbb{L}$ and therefore its application to the irreps of $\mathfrak{so}(3)$ returns

$$\begin{aligned} \hat{\Gamma}_{iso}^{mag} |\rho_{kq}\rangle &= W\lambda_k^{mag} |\rho_{kq}\rangle \\ \lambda_k^{mag} &= k(k+1). \end{aligned} \tag{4.42}$$

4.3.3 Relaxation superoperator for quadrupolar relaxation

If relaxation occurs via a fluctuating electric field gradient $V^{fluc}(t)$ satisfying the assumptions of WBR theory (short correlation time, zero average), then the spin–lattice relaxation Hamiltonian is given by

$$\mathcal{H}_{SLR}^{Q}(t) = \frac{1}{6} \sum_{\alpha,\beta=x,y,z} Q_{\alpha\beta} V_{\alpha\beta}^{fluc}(t) \tag{4.43}$$

and the relaxation superoperator is

$$\begin{aligned} \hat{\Gamma}^{Q} &= \int_0^\infty \mathrm{d}\tau \, \overline{\hat{\mathcal{H}}_{SLR}^{Q}(t+\tau)\hat{\mathcal{H}}_{SLR}^{Q}(t)} \\ &= \frac{1}{6^2} \sum_{\alpha,\beta,\gamma,\delta} \hat{Q}_{\alpha\beta}\hat{Q}_{\gamma\delta} \int_0^\infty \mathrm{d}\tau \, \overline{V_{\alpha\beta}^{fluc}(t+\tau)V_{\gamma\delta}^{fluc}(t)}. \end{aligned} \tag{4.44}$$

Again, in order to simplify the treatment of powder samples, we will assume that the fluctuations be isotropic. For symmetric traceless tensors like $V^{fluc}(t)$, this can be written more naturally after changing from a Cartesian basis to a spherical tensor basis

$$\begin{aligned} V_{2,0}^{fluc} &= \sqrt{\frac{1}{6}}(2V_{zz}^{fluc} - V_{xx}^{fluc} - V_{yy}^{fluc}) \\ V_{2,\pm1}^{fluc} &= \mp\frac{1}{2}(V_{xz}^{fluc} + V_{zx}^{fluc} \pm i(V_{yz}^{fluc} + V_{zy}^{fluc})) \\ V_{2,\pm2}^{fluc} &= \frac{1}{2}(V_{xx}^{fluc} - V_{yy}^{fluc} \pm i(V_{xy}^{fluc} + V_{yx}^{fluc})). \end{aligned} \tag{4.45}$$

In terms of spherical tensors, the relaxation superoperator becomes

$$\begin{aligned} \hat{\Gamma}^{Q} &= \frac{1}{6^2} \sum_{q,q'=-2}^{2} (-1)^{q+q'} \hat{Q}_{2,-q}\hat{Q}_{2,-q'} \int_0^\infty \mathrm{d}\tau \, \overline{V_{2,q}^{fluc}(t+\tau)V_{2,q'}^{fluc}(t)} \\ &= \Big(\frac{eQ}{2I(2I-1)}\Big)^2 \sum_{q,q'=-2}^{2} (-1)^{q+q'} \hat{T}_{2,-q}\hat{T}_{2,-q'} \int_0^\infty \mathrm{d}\tau \, \overline{V_{2,q}^{fluc}(t+\tau)V_{2,q'}^{fluc}(t)}, \end{aligned} \tag{4.46}$$

where I used the fact that the nuclear electric quadrupole moment in terms of spherical tensor operators is

$$Q_{2q} = \frac{3eQ}{I(2I-1)} T_{2q}. \tag{4.47}$$

Now we are able to define isotropic EFG fluctuations in analogy to isotropic magnetic fluctuations

$$\left(\frac{eQ}{2I(2I-1)}\right)^2 \int_0^\infty \mathrm{d}\tau\, \overline{V_{2,q}^{fluc}(t+\tau)V_{2,q'}^{fluc}(t)} = (-1)^q W_Q \delta_{q,-q'} \tag{4.48}$$

and obtain the relaxation superoperator for isotropic EFG fluctuations:

$$\hat{\Gamma}_{iso}^{Q} = W_Q \sum_{q=-2}^{2} (-1)^q \hat{T}_{2,-q}\hat{T}_{2,q}. \tag{4.49}$$

Since this superoperator is clearly invariant under rotations, its eigenspaces are again equal to the irreps of $\mathfrak{so}(3)$:

$$\hat{\Gamma}_{iso}^{Q} \left|\rho_{kq}\right\rangle = W_Q \lambda_k^Q \left|\rho_{kq}\right\rangle. \tag{4.50}$$

It is straightforward, but very tedious, to show that

$$\lambda_k^Q = \frac{k(k+1)}{2}(4I(I+1) - k(k+1) - 1). \tag{4.51}$$

4.3.4 The Redfield kite and the master equation

In order to solve the equation of motion of WBR theory (Eq. 4.33), we must treat the relaxation superoperator as a perturbation of the coherent dynamics due to $\mathcal{H}_0$. In this section, I will show that this lets us define an effective relaxation superoperator (the "Redfield matrix") using first-order perturbation theory, for which many matrix elements are zero.

Suppose the average Hamiltonian is given by a dominant Zeeman term and a quadrupolar first-order perturbation,

$$\mathcal{H}_0 = \omega_0 I_z + \frac{\omega_Q}{6}(3I_z^2 - I(I+1)). \tag{4.52}$$

The canonical basis of $\mathbb{L}$ is an eigenbasis of $\hat{\mathcal{H}}_0$:

$$\hat{\mathcal{H}}_0 \big|\, |m\rangle\langle m'| \,\big\rangle = (\omega_0(m-m') + \frac{\omega_Q}{2}(m^2 - m'^2)) \big|\, |m\rangle\langle m'| \,\big\rangle \tag{4.53}$$

Clearly, all diagonal density matrices ($m = m'$) form an eigenspace with eigenvalue 0, while all other canonical basis vectors span one-dimensional eigenspaces.

If relaxation is slow compared to the Zeeman and quadrupolar frequencies, we have the following hierarchy of frequencies and rates in our system:

$$\omega_0 \gg \omega_Q \gg W, W^Q. \tag{4.54}$$

When solving the WBR equation of motion, we can view relaxation as a perturbation to the evolution under $\hat{\mathcal{H}}_0$. Then, we must use degenerate

perturbation theory in the subspace of diagonal density matrices and non-degenerate perturbation theory for all one-dimensional eigenspaces. Since isotropic superoperators map diagonal matrices onto diagonal matrices, in that case the degenerate perturbation theory is identical to the exact treatment applied to diagonal matrices.

Thus, to first order in this perturbation theory, the effective relaxation superoperator (also known as the "Redfield matrix") is block-diagonal in the canonical basis. This block-diagonal structure is known as the *Redfield kite* [33, p. 54]. In our particular example of quadrupolar NMR with negligible spin–spin interactions, the Redfield matrix is completely diagonal except for one block corresponding to the diagonal density matrices.

In applications of relaxation theory to longitudinal relaxation, especially for quadrupolar nuclei in strongly-correlated electron materials, one often specifies not the full relaxation superoperator $\hat{\Gamma}$, but only the matrix of the diagonal block acting on diagonal density matrices Γ^{diag}. The diagonal density matrix elements, i.e. the populations, are collected in a vector $\vec{p}$. The relaxation behaviour of the populations is then described by a master equation

$$\frac{\mathrm{d}}{\mathrm{d}t}\vec{p}(t) = -\Gamma^{diag}(\vec{p}(t) - \vec{p}_0) \tag{4.55}$$

where $\vec{p}_0$ are the populations in thermal equilibrium.

Let us derive the matrix Γ^{diag} for the two cases of magnetic relaxation and of isotropic quadrupolar relaxation.

The master equation for magnetic relaxation

For this derivation, I will assume isotropic magnetic relaxation. As can be seen in reference [136], the result for anisotropic magnetic relaxation is identical.

The matrix elements of Γ^{diag} are given by

$$\Gamma^{diag}_{m'm} = \left\langle \left|m'\right\rangle \left\langle m'\right| \left|\hat{\Gamma}^{mag}_{iso}\right| \left|m\right\rangle \left\langle m\right| \right\rangle. \tag{4.56}$$

Using equations 4.41, 4.16, and 4.1 , we can write this matrix element

as

$$\begin{aligned}
\big\langle |m'\rangle\langle m'| \big|\hat{\Gamma}_{iso}^{mag}\big| |m\rangle\langle m| \big\rangle &= W\sum_{q=-1}^{1} \big\langle |m'\rangle\langle m'| \big|\hat{T}_{1,q}^{\dagger}\hat{T}_{1,q}\big| |m\rangle\langle m| \big\rangle \\
&= W\sum_{q=-1}^{1} \mathrm{tr}\left((\hat{T}_{1,q}|m'\rangle\langle m'|)^{\dagger}\hat{T}_{1,q}|m\rangle\langle m|\right) \\
&= W\sum_{q=-1}^{1} \mathrm{tr}\left([T_{1,q},|m'\rangle\langle m'|]^{\dagger}[T_{1,q},|m\rangle\langle m|]\right) \\
&= W\sum_{q=-1}^{1} \mathrm{tr}\left((|m'\rangle\langle m'|T_{1,q}^{\dagger} - T_{1,q}^{\dagger}|m'\rangle\langle m'|)(T_{1,q}|m\rangle\langle m| - |m\rangle\langle m|T_{1,q})\right) \\
&= W\sum_{q=-1}^{1} \big(\langle m|m'\rangle\langle m'|T_{1,q}^{\dagger}T_{1,q}|m\rangle + \langle m'|m\rangle\langle m|T_{1,q}T_{1,q}^{\dagger}|m'\rangle \\
&\qquad - |\langle m'|T_{1,q}|m\rangle|^2 - |\langle m'|T_{1,q}^{\dagger}|m\rangle|^2\big) \\
&= W\sum_{q=-1}^{1} \big(\delta_{m'm}\sum_{m''}(|\langle m''|T_{1q}|m\rangle|^2 + |\langle m''|T_{1,q}^{\dagger}|m\rangle|^2) \\
&\qquad - |\langle m'|T_{1,q}|m\rangle|^2 - |\langle m'|T_{1,q}^{\dagger}|m\rangle|^2\big).
\end{aligned} \tag{4.57}$$

Replacing the spherical tensor operators by explicit spin operators according to equation 4.15 and simplifying the equation yields

$$\Gamma_{m'm}^{diag} = \begin{cases} -W|\langle m+1|I_+|m\rangle|^2 = -W(I(I+1)-m(m+1)) & m' = m+1 \\ -W|\langle m-1|I_-|m\rangle|^2 = -W(I(I+1)-m(m-1)) & m' = m-1 \\ -\sum_{m''}\Gamma_{mm''}^{diag} = 2W(I(I+1)-m^2) & m' = m \\ 0 & \text{otherwise.} \end{cases} \tag{4.58}$$

Clearly, this matrix is often much easier to handle than the full superoperator, which is why this approach is so widespread in the literature.

The master equation for isotropic quadrupolar relaxation

The derivation for isotropic quadrupolar relaxation proceeds in full analogy to that for isotropic magnetic relaxation. After the same manipulations as

in equation 4.57, we obtain

$$\begin{aligned}\Gamma^{diag}_{m'm} &= \left\langle \left|m'\right\rangle \left\langle m'\right| \left|\hat{\Gamma}^{Q}_{iso}\right| \left|m\right\rangle \left\langle m\right| \right\rangle \\ &= W^Q \sum_{q=-2}^{2} \big(\delta_{m'm} \sum_{m''} (|\left\langle m''\right| T_{2q} \left|m\right\rangle|^2 + |\left\langle m''\right| T^{\dagger}_{2,q} \left|m\right\rangle|^2) \\ &\qquad - |\left\langle m'\right| T_{2,q} \left|m\right\rangle|^2 - |\left\langle m'\right| T^{\dagger}_{2,q} \left|m\right\rangle|^2\big).\end{aligned} \tag{4.59}$$

Using equations 4.15 and simplifying gives

$$\Gamma^{diag}_{m'm} = \begin{cases} -\frac{W^Q}{2}|\left\langle m+2\right| I_+^2 \left|m\right\rangle|^2 & m' = m+2 \\ -\frac{W^Q}{2}|\left\langle m+1\right| I_z I_+ + I_+ I_z \left|m\right\rangle|^2 & m' = m+1 \\ -\frac{W^Q}{2}|\left\langle m-1\right| I_z I_- + I_- I_z \left|m\right\rangle|^2 & m' = m-1 \\ -\frac{W^Q}{2}|\left\langle m-2\right| I_-^2 \left|m\right\rangle|^2 & m' = m-2 \\ -\sum_{m''} \Gamma^{diag}_{mm''} & m' = m \\ 0 & \text{otherwise.} \end{cases} \tag{4.60}$$

Evaluating the off-diagonal matrix elements yields

$$\begin{aligned}\Gamma^{diag}_{m+2,m} &= -\frac{W^Q}{2}(I(I+1) - (m+1)(m+2))(I(I+1) - m(m+1)) \\ \Gamma^{diag}_{m+1,m} &= -\frac{W^Q}{2}(I(I+1) - m(m+1))(2m+1)^2 \\ \Gamma^{diag}_{m-1,m} &= -\frac{W^Q}{2}(I(I+1) - m(m-1))(2m-1)^2 \\ \Gamma^{diag}_{m-2,m} &= -\frac{W^Q}{2}(I(I+1) - (m-1)(m-2))(I(I+1) - m(m-1)).\end{aligned} \tag{4.61}$$

The eigenvalues of this matrix can be computed analytically in order to prove equation 4.51.

4.4 Longitudinal and transverse relaxation

In longitudinal relaxation ("T_1") measurements such as inversion recovery (IR) and saturation recovery (SR) experiments, the initial density matrix is prepared in a diagonal state and its relaxation is observed. In terms of the Redfield kite, we need to consider only the diagonal block acting on diagonal density matrices.

Assuming the preparation is fast enough, the IR and SR signals have the same shape:

$$S_{IR}(t) \propto 1 - 2f(t) \tag{4.62}$$

$$S_{SR}(t) \propto 1 - f(t) \tag{4.63}$$

where $f(t)$ is defined such that $f(0) = 1$ and $f(t \to \infty) = 0$. For data analysis in both IR and SR, I will use the fit function

$$S(t) = a - bf(t), \tag{4.64}$$

where the parameters a and b can account for imperfect experimental conditions. The functional form of $f(t)$ will be derived for different conditions (hard and soft pulses, magnetic and quadrupolar relaxation). Since IR and SR are ideally equivalent, I will only discuss IR below.

In transverse relaxation ("T_2") measurements such as spin-echo decay (SED) experiments, the initial density matrix contains off-diagonal elements whose relaxation is measured.

While longitudinal relaxation probes only spin–lattice relaxation, transverse relaxation probes a combination of spin–lattice relaxation and so-called "spin–spin relaxation", which is due to nuclear-spin–nuclear-spin interactions which are not refocussed by the RF pulse sequence. If there are no degenerate transitions, e.g. in the case of quadrupolar NMR, then the spin–lattice contribution to the transverse relaxation of the $m \leftrightarrow m'$ transition comes only from the matrix element $\left\langle \left|m\right\rangle \left\langle m'\right| \left|\hat{\Gamma}\right| \left|m\right\rangle \left\langle m'\right| \right\rangle$ due to the Redfield kite structure.

In our case, the pulse sequence is a simple $\pi/2 - \pi$ Hahn echo sequence, which does not refocus e.g. any homonuclear indirect or dipolar coupling.

The spin–lattice and spin–spin relaxation components of the SED signal may be separated as [107]

$$S_{SED}(t) = f_{SLR}(t) f_{SSR}(t). \tag{4.65}$$

In this section 4.8, I will derive that $f_{SLR}(t)$ is an exponential function whose decay rate is related to T_1.

4.5 Inversion recovery in NMR in the hard pulse limit

In the hard pulse limit ($\omega_1 \gg \omega_Q$), the initial state of an IR experiment is

$$\sigma(t = 0) - \sigma_0 = -2\sigma_0 \propto I_z \propto \rho_{10}. \tag{4.66}$$

and the IR signal is given by

$$S_{IR}(t) \propto \langle I_z | \sigma(t) \rangle . \tag{4.67}$$

Macroscopically, this is simply a measurement of the relaxation of the total nuclear magnetisation, which should recover as a single exponential with time constant T_1 according to the Bloch equation 2.15.

4.5.1 Magnetic relaxation

For isotropic magnetic relaxation, the time evolution of this state is easily found, because it is an eigenvector of the relaxation superoperator and its eigenvalue is known from equation 4.42:

$$\begin{aligned}\frac{\mathrm{d}}{\mathrm{d}t}|\sigma(t)\rangle &= -\hat{\Gamma}^{mag}_{iso}(|\sigma(t)\rangle - |\sigma_0\rangle) \\ &= -2W(|\sigma(t)\rangle - |\sigma_0\rangle),\end{aligned} \tag{4.68}$$

$$|\sigma(t)\rangle - |\sigma_0\rangle = -\mathrm{e}^{-2Wt}|\sigma_0\rangle\,, \tag{4.69}$$

$$S_{IR}(t) \propto 1 - 2\mathrm{e}^{-2Wt}. \tag{4.70}$$

If we now define

$$T_1^{-1} := 2W \tag{4.71}$$

we obtain the expected result

$$f(t) = \exp(-\frac{t}{T_1}). \tag{4.72}$$

4.5.2 Quadrupolar relaxation

For isotropic quadrupolar relaxation, the initial state is also an eigenvector of the relaxation superoperator because of rotational symmetry:

$$\hat{\Gamma}^{Q}_{iso}|\rho_{10}\rangle = W_Q\lambda_1^Q|\rho_{10}\rangle\,. \tag{4.73}$$

This lets us solve the equation of motion and find the IR signal:

$$\begin{aligned}\frac{\mathrm{d}}{\mathrm{d}t}|\sigma(t)\rangle &= -\hat{\Gamma}^{Q}_{iso}(|\sigma(t)\rangle - |\sigma_0\rangle) \\ &= -\lambda_1^Q W_Q(|\sigma(t)\rangle - |\sigma_0\rangle),\end{aligned} \tag{4.74}$$

$$|\sigma(t)\rangle - |\sigma_0\rangle = -\mathrm{e}^{-\lambda_1^Q W_Q t}|\sigma_0\rangle\,, \tag{4.75}$$

$$S_{IR}(t) \propto 1 - 2\mathrm{e}^{-\lambda_1^Q Wt}. \tag{4.76}$$

Evaluating equation 4.51 gives us that

$$\lambda_1^Q = 4I(I+1) - 3. \tag{4.77}$$

After defining

$$T_{1Q}^{-1} = \lambda_1^Q W_Q = (4I(I+1) - 3)W_Q \tag{4.78}$$

we find the expected relaxation behaviour:

$$f(t) = \exp(-\frac{t}{T_{1Q}}). \tag{4.79}$$

4.6 Inversion recovery in NMR in the soft pulse limit

In the soft pulse limit ($\omega_1 \ll \omega_Q$), we can excite and detect only one transition $m \leftrightarrow m-1$. Therefore, the initial state is given by

$$\sigma(t=0) - \sigma_0 \propto |m-1\rangle\langle m-1| - |m\rangle\langle m| \tag{4.80}$$

and the IR signal is

$$S_{IR}(t) \propto \big(\langle |m\rangle\langle m| \,| - \langle |m-1\rangle\langle m-1| \,|\big)|\sigma(t)\rangle\!\rangle. \tag{4.81}$$

4.6.1 Magnetic relaxation

Since our initial state is now not an eigenvector of $\hat{\Gamma}_{iso}^{mag}$ anymore, we need to solve the equations of motion for the general case. Since we have already diagonalised the superoperator, this is quite simple:

$$\begin{aligned}
\frac{\mathrm{d}}{\mathrm{d}t}|\sigma(t)\rangle\!\rangle &= -\hat{\Gamma}_{iso}^{mag}(|\sigma(t)\rangle\!\rangle - |\sigma_0\rangle\!\rangle) \\
&= -\sum_{k=0}^{2I} \hat{\Gamma}_{iso}^{mag} |\rho_{k0}\rangle\!\rangle\langle\!\langle\rho_{k0}| \,(|\sigma(t)\rangle\!\rangle - |\sigma_0\rangle\!\rangle) \\
&= -W\sum_{k=0}^{2I} \lambda_k^{mag} |\rho_{k0}\rangle\!\rangle\langle\!\langle\rho_{k0}| \,(|\sigma(t)\rangle\!\rangle - |\sigma_0\rangle\!\rangle)
\end{aligned} \tag{4.82}$$

$$\begin{aligned}
|\sigma(t)\rangle\!\rangle - |\sigma_0\rangle\!\rangle &= \sum_{k=0}^{2I} \mathrm{e}^{-\lambda_k^{mag} W t} |\rho_{k0}\rangle\!\rangle\langle\!\langle\rho_{k0}| \,(|\sigma(t=0)\rangle\!\rangle - |\sigma_0\rangle\!\rangle) \\
&= \sum_{k=0}^{2I} \exp(-\frac{k(k+1)}{2}\frac{t}{T_1}) \,|\rho_{k0}\rangle\!\rangle\langle\!\langle\rho_{k0}| \,(|\sigma(t=0)\rangle\!\rangle - |\sigma_0\rangle\!\rangle)
\end{aligned} \tag{4.83}$$

Plugging this into equation 4.81, we get

$$\begin{aligned}
S_{IR}(t) \propto & \big(\langle |m\rangle\langle m| \,| - \langle |m-1\rangle\langle m-1| \,|\big)\big(\,|I_z\rangle\!\rangle + \sum_{k=0}^{2I} \exp(-\frac{k(k+1)}{2}\frac{t}{T_1}) \\
& \times |\rho_{k0}\rangle\!\rangle\langle\!\langle\rho_{k0}| \,\big(\big|\,|m-1\rangle\langle m-1|\,\big\rangle\!\big\rangle - \big|\,|m\rangle\langle m|\,\big\rangle\!\big\rangle\big) \\
= & 1 - \sum_{k=0}^{2I} \exp(-\frac{k(k+1)}{2}\frac{t}{T_1}) \\
& \times \big|\langle\!\langle\rho_{k0}| \,\big(\big|\,|m-1\rangle\langle m-1|\,\big\rangle\!\big\rangle - \big|\,|m\rangle\langle m|\,\big\rangle\!\big\rangle\big)\big|^2
\end{aligned} \tag{4.84}$$

and thus

$$f(t)=\sum_{k=0}^{2I}\frac{\left|\langle\rho_{k0}|\left(\left||m-1\rangle\langle m-1|\right\rangle-\left||m\rangle\langle m|\right\rangle\right)\right|^2}{2}\exp(-\frac{k(k+1)}{2}\frac{t}{T_1}). \tag{4.85}$$

In this thesis, I have used the explicit expressions for spin $\frac{5}{2}$ (for ^{17}O) and $\frac{7}{2}$ (for ^{139}La):

$$f^{mag}_{I=\frac{5}{2},CT}(t)=\frac{1}{35}\exp(-\frac{t}{T_1})+\frac{8}{45}\exp(-6\frac{t}{T_1})+\frac{50}{63}\exp(-15\frac{t}{T_1}), \tag{4.86}$$

$$\begin{aligned}f^{mag}_{I=\frac{5}{2},\pm1ST}(t)=&\frac{1}{35}\exp(-\frac{t}{T_1})+\frac{3}{56}\exp(-3\frac{t}{T_1})+\frac{1}{40}\exp(-6\frac{t}{T_1})\\&+\frac{25}{56}\exp(-10\frac{t}{T_1})+\frac{25}{56}\exp(-15\frac{t}{T_1}),\end{aligned} \tag{4.87}$$

$$\begin{aligned}f^{mag}_{I=\frac{5}{2},\pm2ST}(t)=&\frac{1}{35}\exp(-\frac{t}{T_1})+\frac{3}{14}\exp(-3\frac{t}{T_1})+\frac{2}{5}\exp(-6\frac{t}{T_1})\\&+\frac{2}{7}\exp(-10\frac{t}{T_1})+\frac{1}{14}\exp(-15\frac{t}{T_1});\end{aligned} \tag{4.88}$$

$$\begin{aligned}f^{mag}_{I=\frac{7}{2},CT}(t)=&\frac{1}{84}\exp(-\frac{t}{T_1})+\frac{3}{44}\exp(-6\frac{t}{T_1})+\frac{75}{364}\exp(-15\frac{t}{T_1})\\&+\frac{1225}{1716}\exp(-28\frac{t}{T_1}),\end{aligned} \tag{4.89}$$

$$\begin{aligned}f^{mag}_{I=\frac{7}{2},\pm1ST}(t)=&\frac{1}{84}\exp(-\frac{t}{T_1})+\frac{1}{84}\exp(-3\frac{t}{T_1})+\frac{1}{33}\exp(-6\frac{t}{T_1})\\&+\frac{9}{77}\exp(-10\frac{t}{T_1})+\frac{1}{1092}\exp(-15\frac{t}{T_1})+\frac{49}{132}\exp(-21\frac{t}{T_1})\\&+\frac{196}{429}\exp(-28\frac{t}{T_1}),\end{aligned} \tag{4.90}$$

$$\begin{aligned}f^{mag}_{I=\frac{7}{2},\pm2ST}(t)=&\frac{1}{84}\exp(-\frac{t}{T_1})+\frac{1}{21}\exp(-3\frac{t}{T_1})+\frac{1}{132}\exp(-6\frac{t}{T_1})\\&+\frac{25}{308}\exp(-10\frac{t}{T_1})+\frac{100}{273}\exp(-15\frac{t}{T_1})+\frac{49}{132}\exp(-21\frac{t}{T_1})\\&+\frac{49}{429}\exp(-28\frac{t}{T_1}),\end{aligned} \tag{4.91}$$

$$\begin{aligned}f^{mag}_{I=\frac{7}{2},\pm3ST}(t)=&\frac{1}{84}\exp(-\frac{t}{T_1})+\frac{3}{28}\exp(-3\frac{t}{T_1})+\frac{3}{1}\exp(-6\frac{t}{T_1})\\&+\frac{25}{77}\exp(-10\frac{t}{T_1})+\frac{75}{364}\exp(-15\frac{t}{T_1})+\frac{3}{44}\exp(-21\frac{t}{T_1})\\&+\frac{4}{429}\exp(-28\frac{t}{T_1}).\end{aligned} \tag{4.92}$$

Here, "CT" stands for the central transition ($|1/2\rangle \leftrightarrow |-1/2\rangle$), "±1ST" the first satellite transitions $|\pm 1/2\rangle \leftrightarrow |\pm 3/2\rangle$, "±2ST" the second satellite transitions $|\pm 3/2\rangle \leftrightarrow |\pm 5/2\rangle$, etc.

4.6.2 Quadrupolar relaxation

For quadrupolar relaxation, we can do the same calculation, only with λ_k^{mag} and W replaced by λ_k^Q and W_Q. The time dependence of the density matrix is now

$$\begin{aligned} |\sigma(t)\rangle - |\sigma_0\rangle &= \sum_{k=0}^{2I} \mathrm{e}^{-\lambda_k^Q W_Q t} \, |\rho_{k0}\rangle \langle\rho_{k0}| \left(|\sigma(t=0)\rangle - |\sigma_0\rangle\right) \\ &= \sum_{k=0}^{2I} \exp\left(-\frac{\frac{k(k+1)}{2}(4I(I+1)-k(k+1)-1)}{4I(I+1)-3}\frac{t}{T_{1Q}}\right) |\rho_{k0}\rangle \\ &\qquad \times \langle\rho_{k0}| \left(|\sigma(t=0)\rangle - |\sigma_0\rangle\right) \end{aligned} \tag{4.93}$$

and the inversion recovery signal is given by

$$\begin{aligned} S_{IR}(t) = 1 - \sum_{k=0}^{2I} &\exp\left(-\frac{\frac{k(k+1)}{2}(4I(I+1)-k(k+1)-1)}{4I(I+1)-3}\frac{t}{T_{1Q}}\right) \\ &\times \left|\langle\rho_{k0}| \left(\big| \, |m-1\rangle\langle m-1| \, \big\rangle - \big| \, |m\rangle\langle m| \, \big\rangle\right)\right|^2 . \end{aligned} \tag{4.94}$$

Evaluating this explicitly for spin $\frac{5}{2}$ gives the equations below:

$$f^Q_{I=\frac{5}{2},CT}(t) = \frac{1}{35}\exp(-\frac{t}{T_{1Q}}) + \frac{8}{45}\exp(-\frac{33}{8}\frac{t}{T_{1Q}}) + \frac{50}{63}\exp(-\frac{15}{8}\frac{t}{T_{1Q}}), \tag{4.95}$$

$$\begin{aligned} f^Q_{I=\frac{5}{2},\pm 1ST}(t) = &\frac{1}{35}\exp(-\frac{t}{T_{1Q}}) + \frac{3}{56}\exp(-\frac{21}{8}\frac{t}{T_{1Q}}) + \frac{1}{40}\exp(-\frac{33}{8}\frac{t}{T_{1Q}}) \\ &+ \frac{25}{56}\exp(-\frac{35}{8}\frac{t}{T_{1Q}}) + \frac{25}{56}\exp(-\frac{15}{8}\frac{t}{T_{1Q}}), \end{aligned} \tag{4.96}$$

$$\begin{aligned} f^Q_{I=\frac{5}{2},\pm 2ST}(t) = &\frac{1}{35}\exp(-\frac{t}{T_{1Q}}) + \frac{3}{14}\exp(-\frac{21}{8}\frac{t}{T_{1Q}}) + \frac{2}{5}\exp(-\frac{33}{8}\frac{t}{T_{1Q}}) \\ &+ \frac{2}{7}\exp(-\frac{35}{8}\frac{t}{T_{1Q}}) + \frac{1}{14}\exp(-\frac{15}{8}\frac{t}{T_{1Q}}). \end{aligned} \tag{4.97}$$

4.7 Inversion recovery in quadrupolar NMR in antiferromagnetic powders

Let us consider quadrupolar NMR on a material with an antiferromagnetic phase below some temperature T_N. Suppose that we are in the perturbative regime of quadrupolar NMR $\omega_Q \ll \omega_0$ and in the soft pulse limit $\omega_1 \ll \omega_Q$.

In the paramagnetic phase, we can obtain an NMR spectrum, identify all transitions, and fit all inversion recovery curves with the model functions from the previous section.

In the antiferromagnetic phase, however, we have an additional, intrinsic static magnetic field $\vec{B}_{AF}$ at the nucleus due to magnetic order. If the applied magnetic field $\vec{B}_0$ is sufficiently weak, then $\vec{B}_{AF}$ is independent of $\vec{B}_0$ and its direction is locked to the crystal lattice.

Suppose that $|\vec{B}_{AF}| < |\vec{B}_0|$. Then, in a single-crystalline sample, the antiferromagnetic order causes a shift or splitting of the NMR frequencies of the order of $|\gamma B_{AF}|$.

In a powder sample, instead, the spectrum becomes broadened by that same amount, due to the random orientation of $\vec{B}_{AF}$, with respect to $\vec{B}_0$ If this field is stronger than the quadrupolar splitting, i.e. if $|\gamma B_{AF}| \gg \omega_Q$, then the different transitions are no longer resolved in a powder. Instead, for any frequency near ω_0, we detect different transitions in different nuclei, depending on the orientation of the crystallite in which they reside.

Thus, the proper fit function for magnetic relaxation is a sum of the recovery functions $f_{I,i}^{mag}(t)$ of different transitions i, weighted by both the number of nuclei for which we excite this transition N_i and the intrinsic signal amplitude from this transition A_i:

$$f_{I,AF}(t) \propto \sum_i N_i A_i f_{I,i}^{mag}(t). \tag{4.98}$$

Suppose we perform our experiments at a carrier frequency of ω_0, where the central transition used to be in the paramagnetic phase. If $|\gamma B_0| \gg |\gamma B_{AF}| \gg \omega_Q$, we can make the approximation that we are resonant with any one transition in an equal number of nuclei, i.e. all N_i are equal.

Next, if we assume that the quantisation axis of each spin is still approximately along z, then the amplitude of the signal from each transition is proportional to the squared matrix element of I_x [111].

For a half-integer spin nucleus, this gives us

$$\begin{aligned} f_{I,AF}(t) \propto & |\langle \tfrac{1}{2} | I_x | -\tfrac{1}{2} \rangle|^2 f_{I,CT}^{mag}(t) + |\langle \tfrac{3}{2} | I_x | \tfrac{1}{2} \rangle|^2 f_{I,+1ST}^{mag}(t) \\ & + |\langle -\tfrac{1}{2} | I_x | -\tfrac{3}{2} \rangle|^2 f_{I,-1ST}^{mag}(t) + \dots \end{aligned} \tag{4.99}$$

Simplifying this expression yields a surprisingly elegant form. Let us

start by plugging in the recovery functions from equation 4.85:

$$\begin{aligned} f_{I,AF}(t) \propto & \sum_{m=-I+1}^{I} |\langle m| I_x |m-1\rangle|^2 \\ & \sum_{k=0}^{2I} \frac{\left|\langle \rho_{k0}| \left(\left| |m-1\rangle \langle m-1| \right\rangle - \left| |m\rangle \langle m| \right\rangle \right)\right|^2}{2} \\ & \exp(-\frac{k(k+1)}{2}\frac{t}{T_1}) \\ = & \sum_{k=0}^{2I} \langle \rho_{k0}| \Big(\sum_{m=-I+1}^{I} \left(\left| |m-1\rangle \langle m-1| \right\rangle - \left| |m\rangle \langle m| \right\rangle \right) \\ & \frac{|\langle m| I_x |m-1\rangle|^2}{2} \left(\left\langle |m-1\rangle \langle m-1| \right| - \left\langle |m\rangle \langle m| \right| \right) \Big) \\ & |\rho_{k0}\rangle \exp(-\frac{k(k+1)}{2}\frac{t}{T_1}). \end{aligned} \tag{4.100}$$

By comparing the matrix elements of the superoperator sandwiched between the ρ_{k0} bra and kets to equation 4.58, we can see that it is in fact equal to $-\frac{1}{2W}\hat{\Gamma}_{iso}^{mag}$ restricted to diagonal density matrices. Thus we get to the final result

$$\begin{aligned} f_{I,AF}(t) &\propto \sum_{k=0}^{2I} \langle \rho_{k0}| (-\frac{1}{2W}\hat{\Gamma}_{iso}^{mag}) |\rho_{k0}\rangle \exp(-\frac{k(k+1)}{2}\frac{t}{T_1}) \\ &= \sum_{k=0}^{2I} \frac{k(k+1)}{2} \exp(-\frac{k(k+1)}{2}\frac{t}{T_1}). \end{aligned} \tag{4.101}$$

4.8 Transverse relaxation in quadrupolar NMR

Let us consider the decay of the spin-echo signal in the soft-pulse limit of quadrupolar NMR due to spin–lattice relaxation. The spin-echo amplitude of the $m \leftrightarrow m-1$ transition is

$$S(t) \propto \langle m-1| \sigma(t) |m\rangle . \tag{4.102}$$

As discussed in Section 4.3.4, the only matrix element of the relaxation superoperator that contributes to the decay of the $m \leftrightarrow m-1$ coherence, is $\left\langle |m\rangle \langle m-1| \left|\hat{\Gamma}\right| |m\rangle \langle m-1| \right\rangle$.

For isotropic magnetic relaxation, this matrix element takes the value

$$\begin{aligned}
&\big\langle\, |m\rangle\langle m-1|\,\big|\hat{\Gamma}_{iso}^{mag}\big|\,|m\rangle\langle m-1|\,\big\rangle \\
&\quad = W\sum_{q=-1}^{1}\big\langle\, |m\rangle\langle m-1|\,\big|(-1)^q\hat{T}_{1,-q}\hat{T}_{1,q}\big|\,|m\rangle\langle m-1|\,\big\rangle \\
&\quad = W\sum_{q=-1}^{1}\big\langle\, |m\rangle\langle m-1|\,\big|\hat{T}_{1,q}^{\dagger}\hat{T}_{1,q}\big|\,|m\rangle\langle m-1|\,\big\rangle.
\end{aligned} \tag{4.103}$$

A brief auxiliary calculation gives:

$$\hat{T}_{1,0}\big|\,|m\rangle\langle m-1|\,\big\rangle = [I_z, |m\rangle\langle m-1|] = \big|\,|m\rangle\langle m-1|\,\big\rangle, \tag{4.104}$$

$$\begin{aligned}
\hat{T}_{1,1}\big|\,|m\rangle\langle m-1|\,\big\rangle &= -\sqrt{\frac{1}{2}}[I_+, |m\rangle\langle m-1|] \\
&= -\sqrt{\frac{I(I+1)-m(m+1)}{2}}\big|\,|m+1\rangle\langle m-1|\,\big\rangle \\
&\quad + \sqrt{\frac{I(I+1)-(m-1)(m-2)}{2}}\big|\,|m\rangle\langle m-2|\,\big\rangle,
\end{aligned} \tag{4.105}$$

$$\begin{aligned}
\hat{T}_{1,-1}\big|\,|m\rangle\langle m-1|\,\big\rangle &= \sqrt{\frac{1}{2}}[I_-, |m\rangle\langle m-1|] \\
&= \sqrt{\frac{I(I+1)-m(m-1)}{2}}\big|\,|m-1\rangle\langle m-1|\,\big\rangle \\
&\quad - \sqrt{\frac{I(I+1)-m(m-1)}{2}}\big|\,|m\rangle\langle m|\,\big\rangle.
\end{aligned} \tag{4.106}$$

The final matrix element is thus

$$\begin{aligned}
&\big\langle\, |m\rangle\langle m-1|\,\big|\hat{\Gamma}_{iso}^{mag}\big|\,|m\rangle\langle m-1|\,\big\rangle = W\big(1+\frac{I(I+1)-m(m+1)}{2} \\
&\quad + \frac{I(I+1)-(m-1)(m-2)}{2} + I(I+1) - m(m-1)\big) \\
&= 2W(I(I+1)-m(m-1))
\end{aligned} \tag{4.107}$$

and the spin–lattice relaxation of the $m \leftrightarrow m-1$ coherence has the form

$$f_{SLR}(t) = \exp(-(I(I+1)-m(m-1))\frac{t}{T_1}). \tag{4.108}$$

4.9 Spin–lattice relaxation in NQR

The NQR Hamiltonian $\mathcal{H}_Q$ has been defined in equation 2.49. Its eigenstates for the case of axially symmetric EFG ($\eta_Q = 0$) are the eigenstates of I_z, as was already the case in quadrupolar NMR. For the general case, however,

the energy eigenstates depend on η_Q. This means that the Redfield matrix will depend on η_Q.

In the case of half-integer spin, each energy level is doubly degenerate by Kramers' theorem [75]. Also an integer spin in an axially symmetric EFG has some doubly degenerate energy levels (c.f. equation 2.51). The presence of degenerate energy levels complicates the Redfield kite structure and must be accounted for.

Since this section is motivated by the analysis of ^{175}Lu-NQR data in $LuNiO_3$ in section 7.4, I will focus on the case of half-integer spins and $\eta_Q \neq 0$.

4.9.1 Partitioning the Hilbert space

The only non-zero matrix elements of $\mathcal{H}_Q$ in the I_z eigenbasis are $\langle m|\mathcal{H}_Q|m\rangle$ and $\langle m \pm 2|\mathcal{H}_Q|m\rangle$. Therefore, the two subspaces

$$\begin{aligned} \mathbb{H}_+ &:= \mathrm{span}(|-I\rangle, |-I+2\rangle, \dots) \\ \mathbb{H}_- &:= \mathrm{span}(|-I+1\rangle, |-I+3\rangle, \dots) \end{aligned} \tag{4.109}$$

are never mixed by $\mathcal{H}_Q$. In order to distinguish them easily, we can define an operator that takes the eigenvalues ± 1 in these two subspaces:

$$\varsigma = \exp(i\pi(I + I_z)). \tag{4.110}$$

On the canonical basis vectors, it acts as $\varsigma\,|m\rangle = (-1)^{I+m}\,|m\rangle$.

The (anti-unitary) time-reversal operator is defined as

$$\check{T} = \exp(-i\pi I_y)\check{K}, \tag{4.111}$$

where $\check{K}$ applies complex conjugation to all coefficients of the vector when written in the I_z eigenbasis [125, p.289]. Applying it to a general state gives

$$\check{T}\big(\sum_m c_m\,|m\rangle\big) = \sum_m (-1)^{I+m} c_m^*\,|-m\rangle\,. \tag{4.112}$$

Before proceeding with diagonalising the Hamiltonian, let us compute a few useful commutators. From Kramers' theorem it is known that $[\check{T}, \mathcal{H}_Q] = 0$. By the construction of ς, it is obvious that $[\varsigma, \mathcal{H}_Q] = 0$. The non-trivial commutator $[\check{T}, \varsigma]$ gives:

$$\begin{aligned} \check{T}\varsigma \sum_m c_m\,|m\rangle &= \check{T}\sum_m (-1)^{I+m} c_m\,|m\rangle = \sum_m (-1)^{2(I+m)} c_m^*\,|m\rangle \\ \varsigma\check{T}\sum_m c_m\,|m\rangle &= \varsigma\sum_m (-1)^{I+m} c_m^*\,|-m\rangle = \sum_m (-1)^{2I} c_m^*\,|-m\rangle \\ [\check{T}, \varsigma] &= \begin{cases} = 0 & I \text{ integer} \\ \neq 0 & I \text{ half-integer} \end{cases} \end{aligned} \tag{4.113}$$

For half-integer spins, this implies that two states forming a Kramers doublet must have different eigenvalues under ς. Therefore, for half-integer spins, diagonalising $\mathcal{H}_Q$ will give doubly degenerate eigenvalues

$$\mathcal{H}_Q \left|\psi_{i,\pm}\right\rangle = \omega_i \left|\psi_{i,\pm}\right\rangle, \quad \varsigma \left|\psi_{i,\pm}\right\rangle = \pm \left|\psi_{i,\pm}\right\rangle. \tag{4.114}$$

When dealing with transverse relaxation, it will be useful to fix the relative phase of two degenerate eigenvectors by demanding that

$$\check{T} \left|\psi_{i,\pm}\right\rangle = \pm \left|\psi_{i,\mp}\right\rangle. \tag{4.115}$$

4.9.2 The Redfield kite in NQR

In preparation for computing the Redfield matrix, let us find the eigenvalues of the superoperator $\hat{\mathcal{H}}_Q$:

$$\hat{\mathcal{H}}_Q \big| \left|\psi_{i,\varsigma}\right\rangle \left\langle\psi_{j,\varsigma'}\right| \big\rangle = (\omega_i - \omega_j) \big| \left|\psi_{i,\varsigma}\right\rangle \left\langle\psi_{j,\varsigma'}\right| \big\rangle. \tag{4.116}$$

One can see that the eigenspace for the eigenvalue 0 (i.e. $i = j$) is spanned by not only the diagonal density matrices $\left|\psi_{i,\varsigma}\right\rangle \left\langle\psi_{i,\varsigma}\right|$ but also the off-diagonal zero-frequency coherences $\left|\psi_{i,\varsigma}\right\rangle \left\langle\psi_{i,-\varsigma}\right|$. All other eigenspaces (associated to the eigenvalues $\omega_i - \omega_j, i \neq j$) are fourfold degenerate due to the four possible combinations of ς and ς'.

In order to further reduce the problem, I would like to decompose the Liouville space in analogy to the decomposition of the Hilbert space using ς. Therefore, I will define the superoperator $\hat{\tau}$ as

$$\hat{\tau} \left|\rho\right\rangle = \varsigma \rho \varsigma^{\dagger}. \tag{4.117}$$

This operator multiplies the ς quantum numbers of the ket and bra state, and thus has eigenvalues ± 1. Dividing the Liouville space into the eigenspaces of $\hat{\tau}$ gives the decomposition

$$\begin{aligned} \mathbb{L}_+ &= (\mathbb{H}_+ \otimes \mathbb{H}_+^*) \oplus (\mathbb{H}_- \otimes \mathbb{H}_-^*) \\ \mathbb{L}_- &= (\mathbb{H}_+ \otimes \mathbb{H}_-^*) \oplus (\mathbb{H}_- \otimes \mathbb{H}_+^*). \end{aligned} \tag{4.118}$$

Applying $\hat{\tau}$ to the canonical basis vectors

$$\begin{aligned} \hat{\tau} \big| \left|m\right\rangle \left\langle m'\right| \big\rangle &= (-1)^{2I+m+m'} \big| \left|m\right\rangle \left\langle m'\right| \big\rangle = (-1)^{m-m'} \big| \left|m\right\rangle \left\langle m'\right| \big\rangle \\ &= \exp(i\pi \hat{I}_z) \big| \left|m\right\rangle \left\langle m'\right| \big\rangle \end{aligned} \tag{4.119}$$

reveals the superoperator identity

$$\hat{\tau} = \exp(i\pi \hat{I}_z). \tag{4.120}$$

All relaxation superoperators considered in this thesiscommute with $\hat{\tau}$. The Redfield matrix can thus be simplified by subdividing each eigenspace of $\hat{\mathcal{H}}_Q$ into eigenspaces of $\hat{\tau}$. Applying $\hat{\tau}$ to an eigenvector of $\hat{\mathcal{H}}_Q$ gives

$$\hat{\tau} \big| \left|\psi_{i,\varsigma}\right\rangle \left\langle\psi_{j,\pm\varsigma}\right| \big\rangle = \pm \big| \left|\psi_{i,\varsigma}\right\rangle \left\langle\psi_{j,\pm\varsigma}\right| \big\rangle. \tag{4.121}$$

For the eigenspace with eigenvalue zero, this implies that the diagonal density matrices fall into $\mathbb{L}_+$ whereas the zero-frequency coherences are in $\mathbb{L}_-$. For the other, four-dimensional eigenspaces, this means that coherences between states with equal and unequal ς quantum number are in $\mathbb{L}_+$ and $\mathbb{L}_-$, respectively. The Redfield kite for NQR with half-integer spins therefore consists of a $2I+1$ by $2I+1$ block acting on diagonal density matrices (i.e. level populations), a second $2I+1$ by $2I+1$ block for the off-diagonal zero-frequency coherences, and two 2 by 2 blocks for each coherence at non-zero frequency.

4.9.3 Inversion recovery in NQR

Suppose that we have a half-integer spin in a generic EFG and that we are studying the inversion recovery of the NQR signal at frequency $\omega_i - \omega_j$. This means that our initial state is given by

$$\sigma(t=0) - \sigma_0 \propto \sum_{\varsigma} \frac{|\psi_{i,\varsigma}\rangle\langle\psi_{i,\varsigma}| - |\psi_{j,\varsigma}\rangle\langle\psi_{j,\varsigma}|}{2}. \tag{4.122}$$

The inversion recovery signal is then given by

$$S_{IR}(t) \propto -\langle \sigma(t=0) - \sigma_0 | \sigma(t) \rangle\,. \tag{4.123}$$

In order to find the time-evolution of $\sigma(t)$, the Redfield matrix for diagonal density matrices must be calculated

$$\Gamma^{diag}_{i,\varsigma;j,\varsigma'} = \big\langle\!\big\langle\, |\psi_{i,\varsigma}\rangle\langle\psi_{i,\varsigma}|\, \big|\hat{\Gamma}\big|\, |\psi_{j,\varsigma'}\rangle\langle\psi_{j,\varsigma'}|\, \big\rangle\!\big\rangle. \tag{4.124}$$

Then, diagonalising the matrix numerically allows for the solution of the equations of motion.

4.9.4 Transverse relaxation in NQR

Transverse relaxation in NQR is complicated by the fact that each non-zero frequency coherence is fourfold degenerate. As discussed in section 4.9.2, the Redfield matrix can be decomposed into two 2×2 blocks. These blocks are usually symmetric, and therefore the four eigenvectors of the Redfield matrix associated to the frequency $\omega_i - \omega_j$ are

$$\begin{aligned}
&\frac{\big|\, |\psi_{i,+}\rangle\langle\psi_{j,+}|\,\big\rangle + \big|\, |\psi_{i,-}\rangle\langle\psi_{j,-}|\,\big\rangle}{\sqrt{2}}, \frac{\big|\, |\psi_{i,+}\rangle\langle\psi_{j,+}|\,\big\rangle - \big|\, |\psi_{i,-}\rangle\langle\psi_{j,-}|\,\big\rangle}{\sqrt{2}} \in \mathbb{L}_+\,,\\
&\frac{\big|\, |\psi_{i,+}\rangle\langle\psi_{j,-}|\,\big\rangle + \big|\, |\psi_{i,-}\rangle\langle\psi_{j,+}|\,\big\rangle}{\sqrt{2}}, \frac{\big|\, |\psi_{i,+}\rangle\langle\psi_{j,-}|\,\big\rangle - \big|\, |\psi_{i,-}\rangle\langle\psi_{j,+}|\,\big\rangle}{\sqrt{2}} \in \mathbb{L}_-\,.
\end{aligned} \tag{4.125}$$

For single-crystalline samples, the orientation of the RF field with respect to the EFG is unique for each atom in the unit cell. Then, for each atom, one

can transform the Zeeman Hamiltonian for the RF field to the interaction frame

$$\mathcal{H}_{rf}^{IF}(t) = \exp(i\mathcal{H}_Q t)\mathcal{H}_{rf}(t)\exp(-i\mathcal{H}_Q t) \tag{4.126}$$

and keep only the secular (non-oscillating) terms. Evolving the equilibrium density matrix under this secular RF Hamiltonian shows which coherences are generated and what their relative phases are. The coherences and their relative phases depend on the direction of the RF field w.r.t. the EFG.

In powder samples, all directions of the RF field occur equiprobably. Therefore, for each RF field direction, one must find the excited coherences. Furthermore, the matrix elements of the RF Hamiltonian are direction-dependent, and thus also the signal amplitude and even the nutation frequency depend on direction and differ between coherences. This makes the theoretical treatment of transverse relaxation in powder-NQR a daunting task even for the simplest relaxation mechanisms. Unfortunately, this work could not be completed within the scope of this thesis.

4.10 Conclusion

After a re-derivation of the well-known equation of motion of Wangsness-Bloch-Redfield (WBR) relaxation theory in the extreme narrowing limit, some applications to solid state physics were described. While in solid state physics, relaxation theory is often formulated only in terms of the master equation for energy level populations, the full WBR theory has several advantages, and it is necessary for describing transverse relaxation. The relaxation superoperators for magnetic and quadrupolar fluctuations were defined. In both cases, the superoperator formalism makes it simple to define the case of isotropic fluctuations. First, this was used to re-derive the known expressions for the inversion recovery curves in quadrupolar NMR. Then, a theoretical expression for the inversion recovery curves of quadrupolar nuclei in antiferromagnetic powders was developed. Next, the contribution of spin–lattice relaxation due to isotropic magnetic fluctuations to the transverse relaxation of quadrupolar nuclei was calculated. Finally, the application of WBR theory to spin–lattice relaxation in NQR was discussed. The theoretical developments in this chapter will be used to fit and interpret experimental relaxation data, which will be discussed in the following chapters.

Chapter 5

A systematic ^{17}O-NMR study of the RENiO$_3$ family

In this chapter, I describe a series of ^{17}O-NMR experiments on powder samples of ten different RENiO$_3$ compounds: RE = La – Er and Y (with the exceptions of Ce, Tb, and Pm, as discussed in chapter 3). For all samples, the NMR spectra, shown in figure 5.1, and spin–lattice relaxation rate, shown in figure 5.2, were measured at room temperature.

Four samples (LaNiO$_3$, PrNiO$_3$, SmNiO$_3$, and YNiO$_3$) were selected for temperature-dependent investigations from room-temperature down to 5 K. Additionally, high-temperature measurements up to 500 K were performed with SmNiO$_3$. Both LaNiO$_3$ and YNiO$_3$ have diamagnetic rare-earth ions, which is advantageous for NMR. They represent opposite extreme cases in the phase diagram of the rare-earth nickelates (Figure 3.1): LaNiO$_3$ remains metallic at all temperatures whereas YNiO$_3$ is insulating below $T_{MI} \approx 582$ K [7]. The discontinuous simultaneous metal–insulator and magnetic transition was studied in PrNiO$_3$. Finally, SmNiO$_3$ was chosen because it has the lowest T_{MI} among the nickelates with $T_{MI} \neq T_{\mathrm{N}}$ (excluding solid solutions with different rare-earths), allowing for easy measurements across the MIT without intervening magnetic order as in PrNiO$_3$ and NdNiO$_3$.

The samples of PrNiO$_3$ and SmNiO$_3$ were prepared by José-Antonio Alonso (for details, see [130, 11]), and enriched with the isotope ^{17}O by Kazimierz Conder at PSI following the annealing procedure described in [89]. All other samples were synthesised and isotopically substituted by Dariusz Gawryluk at PSI [42]. The first preliminary ^{17}O-NMR experiment in PrNiO$_3$ was performed by Marek Pikulski.

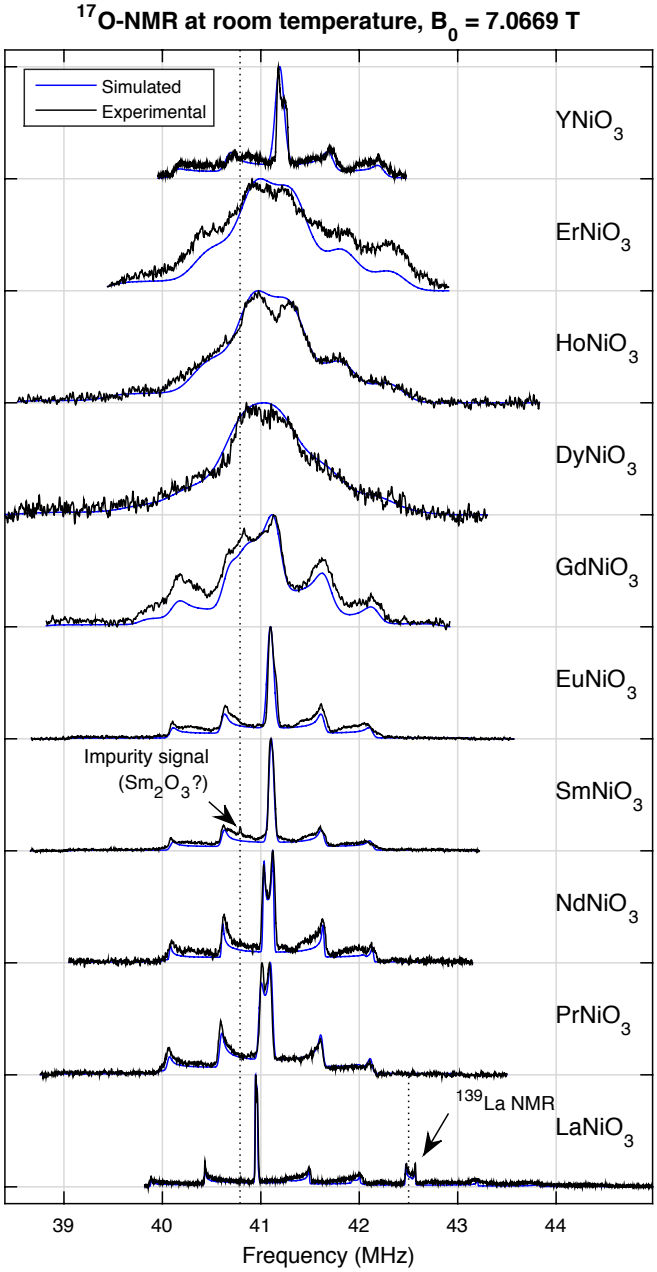

Figure 5.1: Room-temperature ^{17}O-NMR spectra of all RENiO$_3$ samples used for this series of experiments. In LaNiO$_3$, also the ^{139}La-NMR spectrum is recorded because it partially overlaps with the ^{17}O-NMR spectrum. Simulated spectra (blue) assume a single axially symmetric oxygen site, and a single axially symmetric lanthanum site in the case of LaNiO$_3$. The shoulder of the central transition spectrum in YNiO$_3$ could not be reproduced by this simple model. Vertical dotted lines correspond to the reference frequencies (i.e. zero shift) for ^{17}O and ^{139}La in 7.0669 T. A weak impurity signal is found in SmNiO$_3$, which likely originates from unreacted Sm$_2$O$_3$ (see text for details).

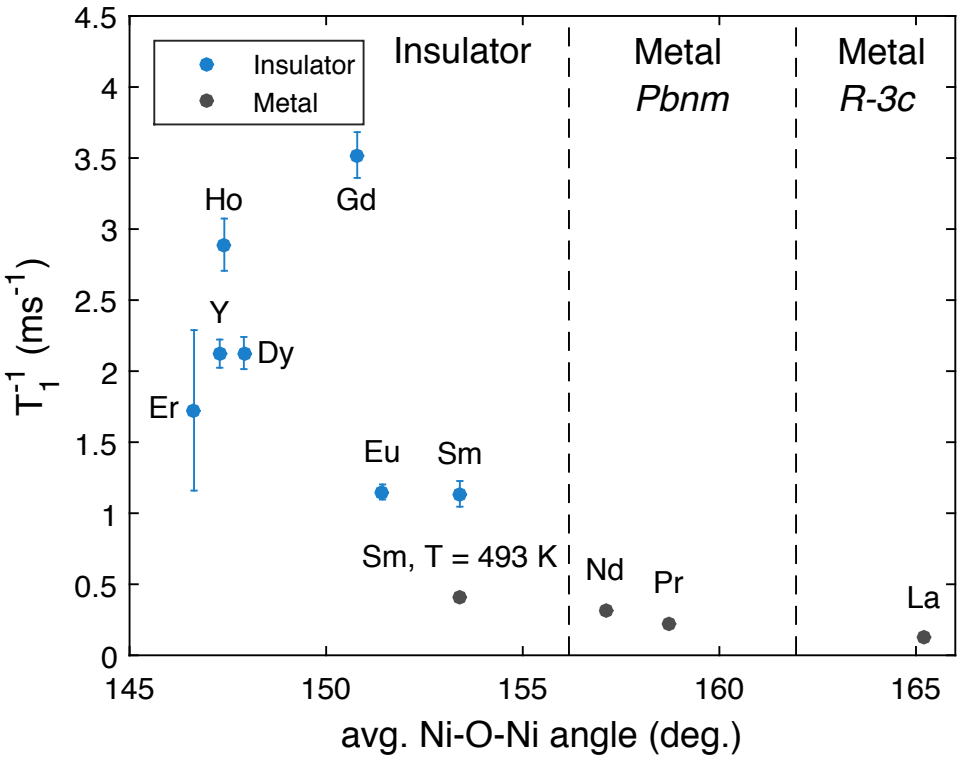

Figure 5.2: Spin–lattice relaxation rate of ^{17}O in RENiO$_3$ at room temperature, and in SmNiO$_3$ above T_{MI}. Vertical dashed lines indicate the metal–insulator and rhombohedral–orthorhombic phase transitions at room temperature. Data shown here were extracted from inversion recovery (IR) measurements at the central transition of the ^{17}O-NMR spectra. IR curves were fitted assuming relaxation purely due to magnetic fluctuations. Since the T_1 of YNiO$_3$ is so similar to that of heavy lanthanide compounds, relaxation must be driven mostly by e_g-σ^* electron spins and not the rare-earth magnetic moment. An exception must be made for GdNiO$_3$, where relaxation is dominated by fluctuations of the Gd^{3+} spin.

5.1 Crystallographic symmetry considerations

Purely from symmetry considerations, there are several restrictions on the NMR spectra of RENiO$_3$. In this section, I will discuss the maximal symmetry-allowed Hamiltonians for quadrupolar NMR on both oxygen and the rare-earth ion.

The ideal cubic perovskite structure

Since all the crystal structures of RENiO$_3$ are all distorted perovskites, the lowest-order expectations can be found from considerations of the ideal cubic $Pm\bar{3}m$ perovskite structure.

Here, all oxygen sites are crystallographically equivalent and have a point group symmetry D_{4h}. The crystallographic fourfold rotation symmetry along the Ni–O–Ni axis must also be a symmetry axis of all NMR tensors. Thus, if we approximate the crystal structure of RENiO$_3$ as an ideal cubic perovskite, the ^{17}O-NMR spectrum consists of a single site with axially symmetric shift anisotropy and EFG. The relevant NMR Hamiltonian has only three parameters: the isotropic shift δ_{iso}, the shift anisotropy δ_{aniso}, and the quadrupolar coupling constant C_Q.

Also for the rare-earth there is a single crystallographic site, and it has the point group O_h Thus, its NMR tensors must be isotropic, and the Hamiltonian has only one parameter, δ_{iso}.

The rhombohedral $R\bar{3}c$ structure

In the $R\bar{3}c$ structure of LaNiO$_3$, all oxygen sites remain equivalent, however the point group is reduced to a C_2 rotation about a La–O–La axis. For the NMR tensors, the only constraint is that one eigenvector must be along the C_2 axis, which we will consider the z-axis in this paragraph. Thus, the NMR Hamiltonian has six parameters in general: the isotropic shift δ_{iso}, two parameters for the shift anisotropy (δ_{aniso} and η_S), two parameters for the EFG tensor (C_Q and η_Q), and one angle describing the relative orientation of the principal axes of the shift and EFG tensors about the C_2 axis. Note that here the η parameters must not be restricted to values between 0 and 1 as usual, since the eigenvector along the C_2 axis might not have the largest eigenvalue. In fact, this is almost certainly the case as the O–Ni bonds, which are the symmetry axis of the EFG in the cubic phase, are almost perpendicular to the C_2 axis.

The unique rare-earth site has the point group D_3. Its NMR tensors are axially symmetric, and their symmetry axis is the threefold rotation axis. The Hamiltonian is therefore the same as the one discussed for oxygen in the $Pm\bar{3}m$ phase.

The orthorhombic *Pbnm* structure

In the *Pbnm* structure of the other metallic $RE\mathrm{NiO_3}$, there are two inequivalent oxygen sites, O(1) and O(2), occurring in a ratio of 1 : 2. The point group of O(1) is C_{1h}, i.e. it consists only of a mirror plane, while that of O(2) is the trivial group. For O(1), the Hamiltonian has the same six-parameter form as the one discussed for the point group C_2, however its unique axis is different. The mirror plane is spanned by O(1) and the four nearest rare-earth ions, therefore the unique axis is close to the O(1)–Ni bond directions. For O(2) instead, the Hamiltonian has eight parameters: δ_{iso}, δ_{aniso}, η_S, C_Q, η_Q, and three Euler angles describing the relative orientation of the principal axes systems of the shift and EFG tensors.

The point group of the rare-earth ion is also C_{1h}, with the same mirror plane as discussed for O(1) above. Its NMR Hamiltonian must therefore have the same form as that of O(1).

The monoclinic $P2_1/n$ structure

Finally, in the $P2_1/n$ structure of the insulating $RE\mathrm{NiO_3}$, there are three inequivalent oxygen sites in a ratio of 1 : 1 : 1, which all have a trivial point group and thus the full eight-parameter Hamiltonian described above.

There is still only one rare-earth site, which also has a trivial point group, and thus the general eight-parameter Hamiltonian.

Comparison with experimental spectra

The full ^{17}O-NMR Hamiltonians for the experimental crystal structures have an unwieldy number of parameters — between six and twenty-four (three sites times eight parameters). However, most experimental spectra could be fitted well by assuming a single axially symmetric site, as is the case in the ideal cubic structure, except for the case of $\mathrm{YNiO_3}$. This reduction to three parameters of the NMR Hamiltonian allows for reliable manual fitting, the results of which are overlapped with the experimental data in Figure 5.1. In order to fit the experimental spectra, the calculated spectra were convolved with a Gaussian. Since the same Gaussian broadening was applied to the whole NMR spectrum, i.e. both central and satellite transitions, this shows that the broadening must be magnetic and not quadrupolar in origin.

Note that the simplification of the Hamiltonian does not necessarily imply that all crystallographic oxygen sites are indistinguishable by NMR. In fact, as will be discussed in sections 5.2.3 and 5.2.4, both the shift and EFG tensors for the O(1) site in the *Pbnm* and $P2_1/n$ structures are expected to strongly deviate from axial symmetry. It is possible that this site is more difficult to detect in NMR due to rapid relaxation. Since the NMR signals from samples with small RE^{3+} ions already relax very quickly, it seems not unlikely that if an additional signal would relax even faster, it would be

impossible to measure. The fact that no trace of such an additional signal was seen even in $PrNiO_3$ implies that the additional signal, if it exists, must have a relaxation time which differs by at least one order of magnitude from that of the experimental signal. This is unlikely considering that the spin–lattice relaxation is dominated by the hyperfine coupling to e_g electrons: a large difference in relaxation rates between two oxygen sites would imply a significant difference in hyperfine coupling constants and thus a substantial difference in chemical bonding. Unfortunately, no conclusive evidence was found neither for nor against this conjecture.

5.2 Estimating the NMR Hamiltonian

In the previous section, it was argued that the experimental NMR spectra can be fitted well by assuming an axially symmetric nuclear spin Hamiltonian. Any non-trivial physical interpretation of the NMR data requires knowledge of the underlying mechanisms. For the RENiO$_3$ systems, an important task is to characterise the interactions between the nuclear spins and both the e_g-σ^* electrons and the localised RE^{3+} moments, which both contribute to the shift. The EFG needs to be interpreted in terms of the possible charge disproportionation across the metal–insulator transition.

5.2.1 Hyperfine coupling to e_g-σ^* electrons

In paramagnetic materials with a single species of magnetic ions, the hyperfine coupling can be determined experimentally from the slope of the Clogston–Jaccarino plot, which graphs the NMR shift against the magnetic susceptibility at the same temperature [29]. Due to the strong hybridisation of Ni and O orbitals discussed in section 3.1, a rather large transferred hyperfine coupling of ^{17}O nuclear spins and e_g-σ^* electron spins is expected (c.f. section 2.1.7). Its measurement requires a RENiO$_3$ sample with diamagnetic RE^{3+} ion. In the case of $LaNiO_3$, the magnetic susceptibility is dominated by the temperature-independent Pauli paramagnetism, which is expected for a Fermi liquid [69, p. 315ff]. In our $LaNiO_3$ sample, the temperature-dependence of $\chi(T)$ originates mostly from impurities, which precludes any accurate determination of the hyperfine coupling. Therefore, the only available sample from which the hyperfine coupling to e_g-σ^* electrons can be extracted reliably is $YNiO_3$.

The temperature-dependent magnetic susceptibility of $YNiO_3$ powder was measured by Dariusz Gawryluk in different applied magnetic fields, and is shown in figure 5.3. The isotropic NMR shift was obtained by computing the first moment of the ^{17}O central transition spectrum, after subtraction of the isotropic second-order quadrupole shift according to equation 2.59. Combining these two datasets gives the Clogston–Jaccarino plot shown in

figure 5.4. As can be seen, the linear fit

$$\delta_{iso} = \delta_{orb} + a_{tot}^{e_g}\chi \tag{5.1}$$

agrees perfectly with the data from room temperature down to the magnetic phase transition at $T_{\mathrm{N}} = 152\,\mathrm{K}$. The fitted parameters are

$$\delta_{orb} = -670\,\mathrm{ppm}, \quad a_{tot}^{e_g} = 5.3513\,\mathrm{T}/\mu_{\mathrm{B}}. \tag{5.2}$$

In order to evaluate whether the extracted hyperfine coupling remains a good estimate across the whole $RE\mathrm{NiO_3}$ series, I added a point at the shift and magnetic susceptibility of $\mathrm{LaNiO_3}$ at room temperature (where the impurity contribution is small) to Figure 5.4. Even though the NMR shift and susceptibility of $\mathrm{LaNiO_3}$ and $\mathrm{YNiO_3}$ differ by a factor of ~ 3, extrapolating the fit of the $\mathrm{YNiO_3}$ dataset gives acceptable agreement with the data on $\mathrm{LaNiO_3}$ at 295 K. Therefore, the hyperfine coupling in $\mathrm{YNiO_3}$ and $\mathrm{LaNiO_3}$ should be very similar. Since these two compounds have small and very large RE^{3+} ions, respectively, I will assume that the hyperfine coupling remains constant throughout the entire $RE\mathrm{NiO_3}$ family.

5.2.2 Transferred hyperfine coupling with rare-earth spins

Solid lanthanide oxides are known to have a significant transferred hyperfine coupling, causing large isotropic ^{17}O-NMR shifts which are proportional to the spin $\langle S_z\rangle$ of the rare-earth ion [145]. This shift originates from the hybridisation of the oxygen $2s$ or $2p$ orbitals with unoccupied orbitals of the rare-earth ions ($6s$ or $6p$ or $5d$), which are spin-polarised because of the intra-atomic exchange interaction with $4f$ electrons [82, 145].

Note that unlike for $3d$ transition metal ions, for lanthanide ions the magnetic moment has a large orbital contribution due to their large spin-orbit coupling. Neglecting crystal field splitting and higher J-multiplets, the average magnetic moment of a $4f$ ion in a small applied field B_0 along the z-direction is given by

$$\langle \mu_z\rangle = -\langle L_z + 2S_z\rangle\mu_{\mathrm{B}} = \frac{g_J^2 J(J+1)\mu_{\mathrm{B}}^2}{3k_{\mathrm{B}}T}B_0, \tag{5.3}$$

where the electron g-factor $g_s = 2.0023\ldots$ was approximated by 2 [69, p. 304].

The transferred hyperfine coupling described above does *not* couple to the electronic magnetic moment, but to the electronic spin. Within the same approximation, its expectation value is given by

$$\langle S_z\rangle = -\frac{g_J(g_J-1)J(J+1)\mu_{\mathrm{B}}}{3k_{\mathrm{B}}T}B_0. \tag{5.4}$$

From this formula, it is clear that if $g_J > 1$, $\langle S_z\rangle$ is negative, which is the familiar result for spin-only magnetic moments. For lanthanides with a less

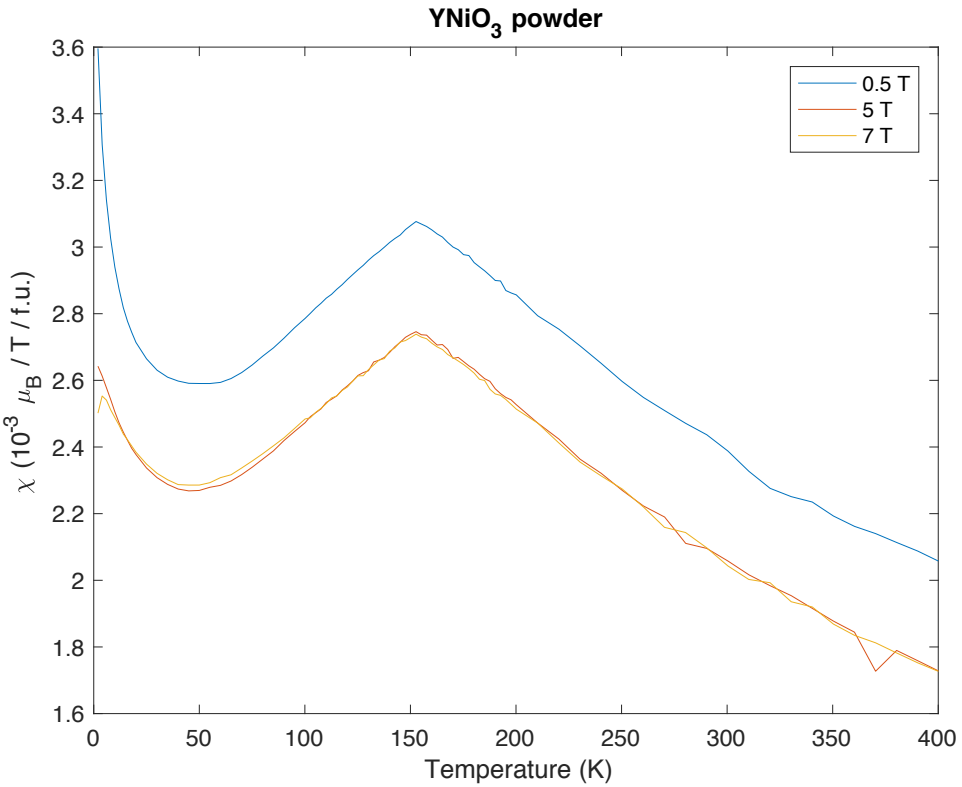

Figure 5.3: Magnetic susceptibility of $YNiO_3$ measured in different fields as a function of temperature. Measurements were performed by Dariusz Gawryluk.

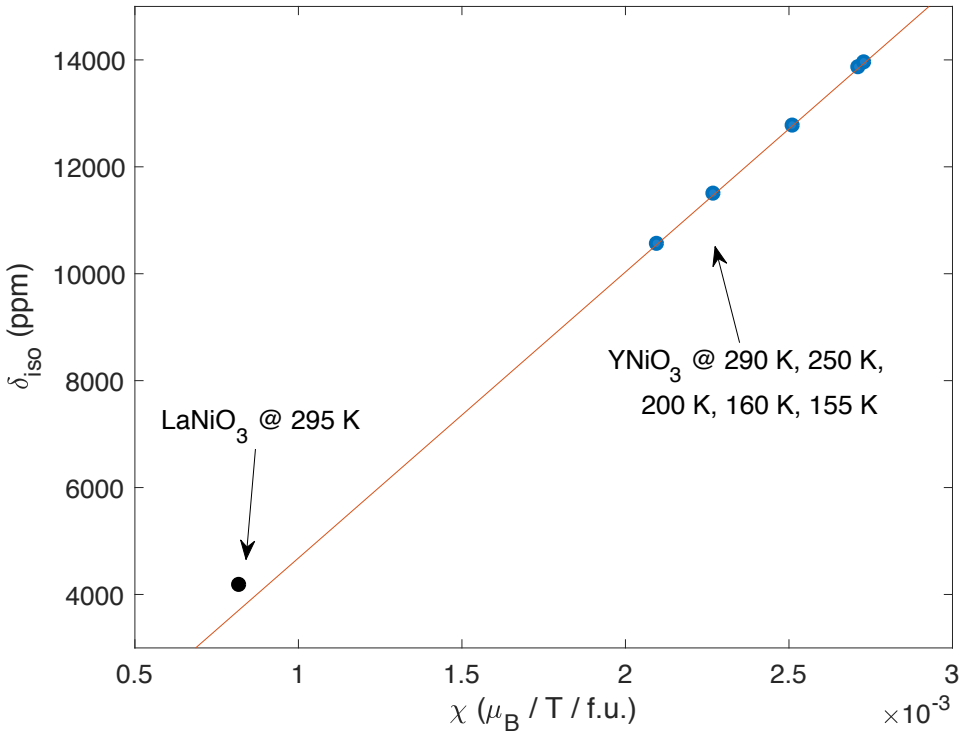

Figure 5.4: Clogston–Jaccarino plot for $YNiO_3$, with an additional point for $LaNiO_3$ at room temperature, using magnetic susceptibility measurements by D. Gawryluk. Fit function: $\delta_{iso} = \delta_{orb} + a_{tot}^{e_g}\chi$ with $\delta_{orb} = -670\,\text{ppm}$ and $a_{tot}^{e_g} = 5.3513\,\text{T}/\mu_\text{B}$.

than half filled $4f$ shell, however, $g_J < 1$ in the ground state according to Hund's rule [69, p.306]. Thus, $\langle S_z \rangle$ is positive, i.e. the spin magnetic moment points opposite to the total ionic magnetic moment for large lanthanides.

For the analysis of this data, instead of using equation 5.4, the numerical value for $\langle S_z \rangle$ from reference [46] is used, which includes corrections such as the admixture of other J-multiplets. The effect of a crystal field or ligand field on the $4f$ orbitals is ignored, however. Although that calculation was originally performed for ^{17}O nuclei in water molecules coordinating RE^{3+} ions in solution, its results have been applied successfully in solid-state NMR [145].

Experimental crystal field parameters in RENiO$_3$ have been reported for Pr^{3+}, Nd^{3+}, Sm^{3+}, and Eu^{3+} [122, 121], but not for the heavier lanthanides. The splitting of the ground state multiplet can be as large as $\sim 80\,\mathrm{meV}$, which is large compared to room temperature ($k_\mathrm{B}T \approx 25\,\mathrm{meV}$). Thus, for the isotropic spin-only susceptibility of the RE^{3+} ions in RENiO$_3$ at room temperature, the values for the spherically symmetric ion are not exact. The crystal field also creates an anisotropic component of the magnetic susceptibility of RE^{3+}, which can affect the isotropic shift via the pseudocontact interaction (c.f. section 2.1.7). For simplicity, I have chosen to neglect the effects of the crystal field in this analysis.

As already shown in figure 5.4 for YNiO$_3$ and LaNiO$_3$, the NMR shift purely due to the e_g electrons changes significantly across the RENiO$_3$ series. Since there is no obvious simple way to model the composition-dependence of this shift component, an ad-hoc fit function is required here. I have chosen to simply use a straight line as function of the average Ni–O–Ni angle. The fit function is thus

$$\delta_{iso} = \alpha + \beta \langle \measuredangle \mathrm{Ni{-}O{-}Ni} \rangle + a_{tot}^{RE} \frac{\langle S_z \rangle}{B_0} \tag{5.5}$$

with literature values for $\langle \measuredangle \mathrm{Ni{-}O{-}Ni} \rangle$ (c.f. figure 3.1 and its references) and $\langle S_z \rangle / B_0$ [46], and δ_{iso} extracted from the fits shown in figure 5.1.

Clearly, the hyperfine coupling extracted from this analysis is only a first approximation, due to the necessary simplifying assumptions. Nevertheless, the resulting model is in reasonable agreement with the experimental data, as is shown in figure 5.5. The fitted value for the total hyperfine coupling is

$$a_{tot}^{RE} = 0.14\,\mathrm{T}. \tag{5.6}$$

Note that since the magnetogyric ratio of the electron is negative, this means that the direction of the hyperfine field at the ^{17}O nucleus is opposite to the spin magnetic moment of the RE^{3+} ion. This is expected for NMR on ligands bonded to rare-earth ions [82].

Compared to the literature value for the hyperfine coupling in RE_2O$_3$ of $0.474\,\mathrm{T}$ [145], this corresponds to a reduction by a factor 3. In both RE_2O$_3$

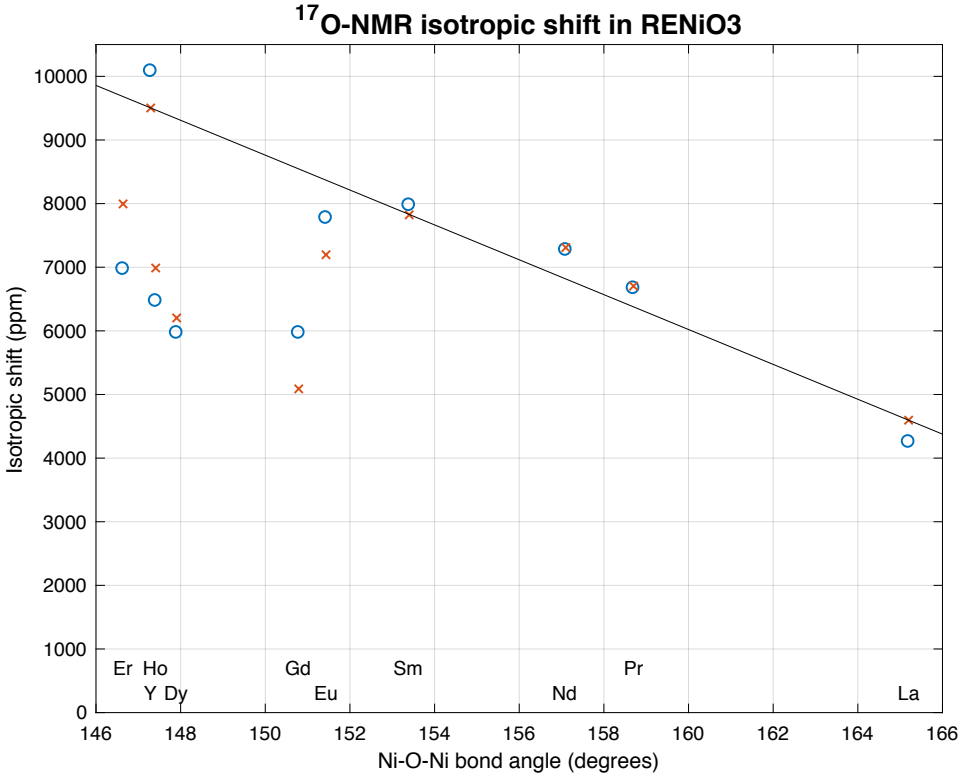

Figure 5.5: Isotropic ^{17}O-NMR shift plotted vs composition. Blue circles: experimental data. Red crosses: fit using a straight line (drawn in black) plus a transferred hyperfine coupling to the spin of the RE^{3+} ions, using spin expectation values from reference [46] and ignoring the crystal field, at room temperature.

and RENiO$_3$, each oxygen has four neighbouring rare-earth ions, therefore a reduced hyperfine coupling directly corresponds to reduced orbital overlap between O and RE. This is not surprising in a ternary oxide (compared to a binary oxide), as the RE–O distances must be larger due to the steric interference of the other metal cation.

5.2.3 Dipolar interaction with rare-earth moments

The fitted shift anisotropy of the ^{17}O-NMR spectra in figure 5.1 is negative and large ($\delta_{aniso} \lesssim -1\,\%$) for DyNiO$_3$, HoNiO$_3$, and ErNiO$_3$, i.e. for the compounds whose rare-earth ions have the largest magnetic moments. This suggests that the shift anisotropy is dominated by the dipolar field of the RE^{3+} moments.

Figure 5.6 compares the experimental data to a simple model

$$\delta_{aniso} = \delta_a^0 + d_{exp}^{\mathrm{Hund}} \chi_{\mathrm{Hund}}, \tag{5.7}$$

with χ_{Hund} the Curie susceptibility in μ_{B}/T per ion in the Hund's rule ground state of the RE^{3+} ion. This means that $\chi_{\mathrm{Hund}} = \langle\mu_z\rangle/B_0$ with $\langle\mu_z\rangle$ taken from equation 5.3. Data on $YNiO_3$ were excluded from this fit because the lineshape of the central transition could not be reproduced by the model of a single axially symmetric site (see figure 5.1), which makes the determination of δ_{aniso} unreliable. The extracted fit parameters are

$$\delta_a^0 = 18\,\mathrm{ppm}(\approx 0), \quad d_{exp}^{\mathrm{Hund}} = -0.16\,\mathrm{T}/\mu_{\mathrm{B}}. \tag{5.8}$$

Clearly, the coupling constant d_{exp}^{Hund} is not exactly the dipolar coupling to the rare-earth ions, as it must contain corrections to the lanthanide magnetic susceptibility as well as the pseudodipolar coupling due to the substantial crystal field (c.f. section 2.1.7). However, since the dipolar coupling tensor is a purely geometric property of the lattice, it can easily be calculated exactly, and compared to d_{exp}^{Hund} in order to check for consistency.

In order to calculate the dipolar coupling tensor, I have used a program written by Marek Pikulski in our lab for computing the dipolar coupling in orthorhombic crystals based on a Ewald summation technique [115, 114].[1] For the idealised $Pm\bar{3}m$ structure with pseudocubic lattice constant $a_{pc} = (a/\sqrt{2} + b/\sqrt{2} + c/2)/3 = 3.8165\,\text{Å}$ of $PrNiO_3$ (values taken from [41]), the dipolar coupling tensor is

$$D_{Pm\bar{3}m} = \begin{pmatrix} 0.0723\,\mathrm{T}/\mu_{\mathrm{B}} & 0 & 0 \\ 0 & 0.0723\,\mathrm{T}/\mu_{\mathrm{B}} & 0 \\ 0 & 0 & -0.1446\,\mathrm{T}/\mu_{\mathrm{B}} \end{pmatrix}. \tag{5.9}$$

This is in agreement with the experimental estimate

$$D_{exp}^{Hund} = \begin{pmatrix} -\frac{d_{exp}^{\mathrm{Hund}}}{2} & 0 & 0 \\ 0 & -\frac{d_{exp}^{\mathrm{Hund}}}{2} & 0 \\ 0 & 0 & d_{exp}^{\mathrm{Hund}} \end{pmatrix} = \begin{pmatrix} 0.08 & 0 & 0 \\ 0 & 0.08 & 0 \\ 0 & 0 & -0.16 \end{pmatrix} \mathrm{T}/\mu_{\mathrm{B}}. \tag{5.10}$$

When plugging in the experimental $Pbnm$ crystal structure of $PrNiO_3$ [41] instead, the diagonalised dipolar couplings take following values for the two oxygen sites:

$$\begin{aligned} D_{diag}(\mathrm{O}(1)) &= \begin{pmatrix} -0.0183\,\mathrm{T}/\mu_{\mathrm{B}} & 0 & 0 \\ 0 & -0.0986\,\mathrm{T}/\mu_{\mathrm{B}} & 0 \\ 0 & 0 & 0.1170\,\mathrm{T}/\mu_{\mathrm{B}} \end{pmatrix}, \\ D_{diag}(\mathrm{O}(2)) &= \begin{pmatrix} 0.0782\,\mathrm{T}/\mu_{\mathrm{B}} & 0 & 0 \\ 0 & 0.1244\,\mathrm{T}/\mu_{\mathrm{B}} & 0 \\ 0 & 0 & -0.2026\,\mathrm{T}/\mu_{\mathrm{B}} \end{pmatrix}. \end{aligned} \tag{5.11}$$

[1] I have modified this program by vectorising parts of the code, achieving a drastic speed-up. All calculations in this thesis used the vectorised code.

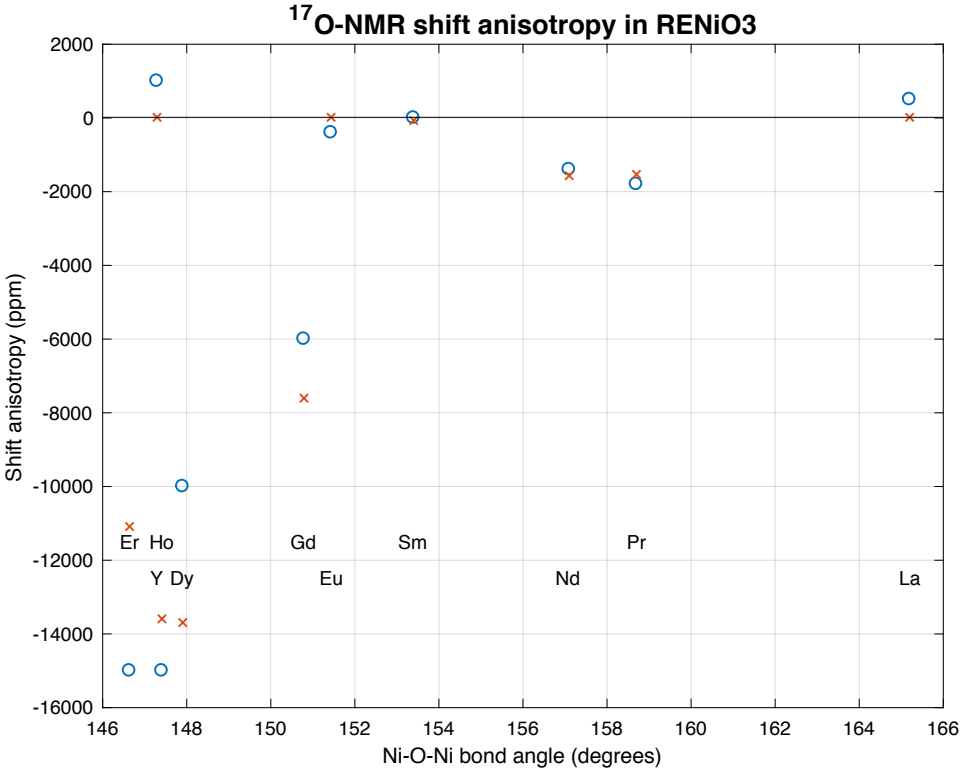

Figure 5.6: Anisotropic ^{17}O-NMR shift plotted vs composition. Circles: experimental data. Crosses: fit using constant times magnetic moment of rare-earth ion in the Hund's rule ground state, plus constant offset (black horizontal line). Clearly, the shift anisotropy is predominantly due to dipolar interaction with the rare-earth ions.

These two tensors are no longer axially symmetric, especially in the case of O(1), and they differ substantially from one another. This behaviour is not seen experimentally. There are two possible ways to reconcile this exact theoretical result with the experimental data: either the O(1) site is invisible in NMR, or the neglected anisotropic effects approximately cancel both the deviation from axial symmetry and the difference between the two sites. The former seems unlikely considering the fact that both oxygen sites couple to the same magnetic ions, thus any difference in the relaxation rate must come from differences in chemical bonding.

5.2.4 Modelling the electric field gradient

The EFG is an interesting experimental quantity in the nickelates because it is sensitive to the charge distribution around the probe nucleus. The simplest model of the EFG in an inorganic material is the point-charge model. It

assumes all chemical bonding to be fully ionic and treats each atom as a point-like electric charge. Clearly, this assumption cannot work very well for RENiO$_3$ because of partially covalent bonding. While values for η_Q can be approximately correct, those for C_Q require a Sternheimer correction factor γ_∞ due to (anti-)shielding of the EFG by inner electrons [132]:

$$C_Q = (1 - \gamma_\infty) C_Q^0, \tag{5.12}$$

where C_Q^0 is the quadrupolar coupling constant due to the lattice and valence electrons. For the F^- ion, the Sternheimer antishielding is estimated as $\gamma_\infty = -22.53$ [133], while for heavy metals it can be as large as $\gamma_\infty \sim -100$ [134].

I have implemented the point-charge model using simple electrostatics, taking into account all ions within a radius of 400 Å of the probe nucleus. For LaNiO$_3$, assuming the experimental crystal structure [41] and fully ionic La^{3+}, Ni^{3+}, and O^{2-}, the point charge model gives the following predictions for ^{17}O and ^{139}La:

$$\begin{aligned} C_Q^0(^{17}\mathrm{O}) &= -0.697\,\mathrm{MHz}, \quad \eta_Q^0(^{17}\mathrm{O}) = 0.086, \\ C_Q^0(^{139}\mathrm{La}) &= 0.308\,\mathrm{MHz}, \quad \eta_Q^0(^{139}\mathrm{La}) = 0.000. \end{aligned} \tag{5.13}$$

As discussed previously, $\eta_Q(^{139}\mathrm{La})$ must be zero by symmetry. The simulated spectrum in Figure 5.1, which is in good agreement with the experimental data, assumes $\eta_Q(^{17}\mathrm{O}) = 0$ and uses $|C_Q(^{17}\mathrm{O})| = 7.1\,\mathrm{MHz}$ and $|C_Q(^{139}\mathrm{La})| = 18\,\mathrm{MHz}$. These experimental values differ from the point-charge model values by factors of about 10 and 60, respectively, which seem like reasonable values for the antishielding factor.

In order to assess the effect of a possible charge disproportionation on the EFG, I have performed the analogous calculation also for YNiO$_3$. Using the experimental $P2_1/n$ structure [8] and assuming the ionic charges Y^{3+}, Ni^{3+}, and O^{2-}, i.e. no charge disproportionation, the following values are obtained for the three oxygen sites:

$$\begin{aligned} C_Q^0(\mathrm{O}(1)) &= -0.591\,\mathrm{MHz}, \quad \eta_Q^0(\mathrm{O}(1)) = 0.804, \\ C_Q^0(\mathrm{O}(2)) &= -0.559\,\mathrm{MHz}, \quad \eta_Q^0(\mathrm{O}(2)) = 0.101, \\ C_Q^0(\mathrm{O}(3)) &= -0.564\,\mathrm{MHz}, \quad \eta_Q^0(\mathrm{O}(3)) = 0.131. \end{aligned} \tag{5.14}$$

The same simulation assuming full charge disproportionation, i.e. Ni^{2+} on the Ni(1) position and Ni^{4+} on the Ni(2) site, gives the following values instead:

$$\begin{aligned} C_Q^0(\mathrm{O}(1)) &= -0.685\,\mathrm{MHz}, \quad \eta_Q^0(\mathrm{O}(1)) = 0.686, \\ C_Q^0(\mathrm{O}(2)) &= -0.602\,\mathrm{MHz}, \quad \eta_Q^0(\mathrm{O}(2)) = 0.075, \\ C_Q^0(\mathrm{O}(3)) &= -0.693\,\mathrm{MHz}, \quad \eta_Q^0(\mathrm{O}(3)) = 0.187. \end{aligned} \tag{5.15}$$

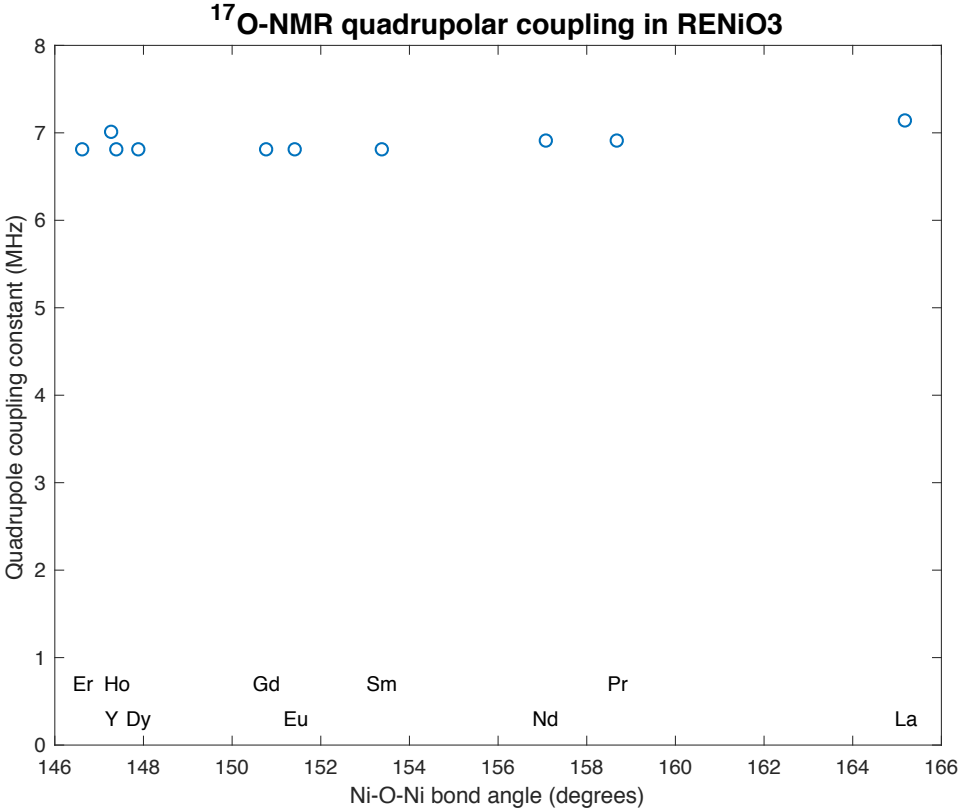

Figure 5.7: Quadrupole coupling constant of ^{17}O in RENiO$_3$ plotted versus composition. Clearly, the experimental data is approximately constant across the metal–insulator transition, which is inconsistent with full charge disproportionation of Ni ions in the insulating phase, at least at the level of a point-charge model. Note however that the EFG in this model is clearly not correct due to partially covalent bonding in the nickelates.

First, notice that the relative change of C_Q^0 between the two simulation for the different sites is between 7 to 23 %. Such a large change in C_Q can be easily resolved in the experiments. Therefore, if a full charge disproportionation occurs, a significant change of C_Q should be apparent in the NMR spectra, both when comparing the paramagnetic insulating and the metallic phase of a single RENiO$_3$ sample and when comparing RENiO$_3$ samples with different degrees of charge disproportionation. This is *not* seen in the experiment — Figure 5.7 shows that at room temperature all samples have $|C_Q| \approx 7\,\text{MHz}$, and the $|C_Q|$ in SmNiO$_3$ below and above T_{MI} shown in figure 5.8 also remains constant across the transition.

Second, the EFG at the O(1) site is very asymmetric in this model, with huge values of η_Q^0. This is consistent with the strong asymmetry of the dipolar coupling of O(1) to the rare-earth moments in equation 5.11, but

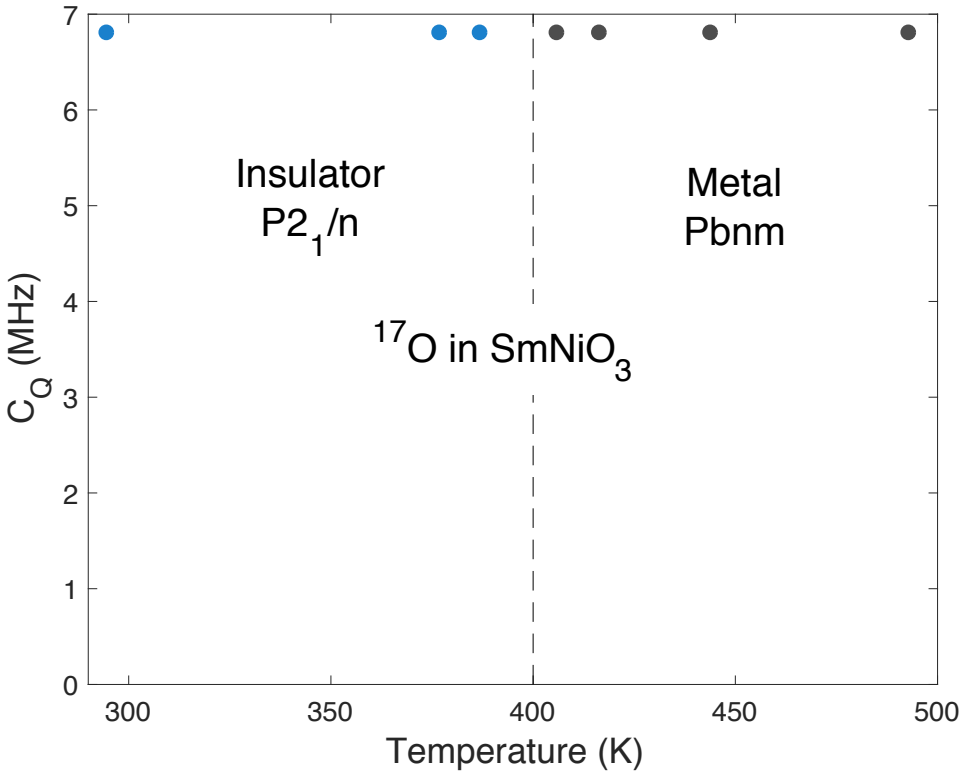

Figure 5.8: The quadrupolar coupling constant C_Q versus temperature in $SmNiO_3$ above room temperature. In a point-charge model, a full charge disproportionation of Ni ions at $T_{MI} = 400\,\mathrm{K}$ would cause a change in C_Q of the order of 10 %, which is not seen in the experiment. Instead, C_Q remains constant within the accuracy of the measurement across T_{MI}.

inconsistent with experiments.

Instead of computing the EFG from a point-charge model, better agreement with experiment can be achieved using density functional theory (DFT). Such calculations have been performed by Oleg Peil [106]. In these DFT simulations, the magnitude of the quadrupolar coupling constant is approximately correct, with $C_Q^{DFT} \sim -7\,\mathrm{MHz}$ for all oxygen sites. The EFGs for all sites are also much less asymmetric than those in the point-charge model, though the η_Q for the O(1) site still disagrees with the experimental data.

5.2.5 The ^{17}O-NMR Hamiltonian in RENiO$_3$

In order to interpret ^{17}O-NMR relaxation data in the following sections, it is important to know how the nuclear spins couple to the other magnetic degrees of freedom in the system. Therefore, let us briefly summarise the results of section 5.2.

The effective ^{17}O-NMR Hamiltonian in RENiO$_3$ is axially symmetric and describes only a single site. In a crystal-fixed coordinate system with the symmetry axis along z, it takes the form

$$\begin{aligned}\mathcal{H} = &-\gamma\vec{I}\cdot(1+\delta_{iso}+\begin{pmatrix}-\frac{\delta_{aniso}}{2} & 0 & 0\\ 0 & -\frac{\delta_{aniso}}{2} & 0\\ 0 & 0 & \delta_{aniso}\end{pmatrix})\vec{B}_0 \\ &+\frac{2\pi C_Q}{4I(2I-1)}(3I_z^2-\vec{I}^2).\end{aligned} \tag{5.16}$$

In sections 5.2.1, 5.2.2 and 5.2.3, I have demonstrated that to good approximation, the isotropic and anisotropic shift can be fully explained by an isotropic orbital shift, hyperfine coupling to e_g-σ^* electrons, and both transferred and dipolar hyperfine interaction with lanthanide ions. Plugging in the results from equations 5.1, 5.5, and 5.7, and replacing $\chi\vec{B}_0 \approx -g^{e_g}\mu_\mathrm{B}\langle\vec{S}^{e_g}\rangle$ and $\chi_\mathrm{Hund}\vec{B}_0 \approx -g_J^{RE}\mu_\mathrm{B}\langle\vec{J}^{RE}\rangle$ yields

$$\begin{aligned}\mathcal{H} \approx &-\gamma(1+\delta_{orb})\vec{I}\cdot\vec{B}_0 + \gamma a_{tot}^{e_g} g^{e_g}\mu_\mathrm{B}\,\vec{I}\cdot\langle\vec{S}^{e_g}\rangle - \gamma a_{tot}^{RE}\,\vec{I}\cdot\langle\vec{S}^{RE}\rangle \\ &+\gamma d_{exp}^{\mathrm{Hund}} g_J^{RE}\mu_\mathrm{B}\,\vec{I}\cdot\begin{pmatrix}-\frac{1}{2} & 0 & 0\\ 0 & -\frac{1}{2} & 0\\ 0 & 0 & 1\end{pmatrix}\langle\vec{J}^{RE}\rangle + \frac{2\pi C_Q}{4I(2I-1)}(3I_z^2-\vec{I}^2),\end{aligned} \tag{5.17}$$

with g^{e_g} the gyromagnetic ratio of the e_g-σ^* electrons, $\vec{S}^{e_g}$ the e_g-σ^* electron spin, $\vec{S}^{RE}$ the total spin of a RE^{3+} ion, and $\vec{J}^{RE}$ the total angular momentum of a RE^{3+} ion. The literature value of g^{e_g} based on electron spin resonance measurements in YNiO$_3$ is 2.16 ± 0.02 [27]. All other quantities in this approximate Hamiltonian have been determined in the previous sections.

Let us briefly compare the orders of magnitude of the different hyperfine coupling terms. The coupling to e_g-σ^* electrons $a_{tot}^{e_g}$ is larger than the dipolar coupling to RE^{3+} moments d_{exp}^{Hund} by a factor of ~ 30. The coupling constant to e_g-σ^* electrons in units of magnetic field is given by $-a_{tot}^{e_g} g^{e_g} \mu_{\mathrm{B}} \approx -11.6\,\mathrm{T}$. This is greater in magnitude than a_{tot}^{RE} by a factor of ~ 80. Thus, the ^{17}O nuclear spins interact much more strongly with e_g-σ^* electrons than with RE^{3+} ions.

5.3 NMR relaxation across the RENiO$_3$ series

In this section, I will discuss NMR relaxation in RENiO$_3$ at room temperature. First, I will use T_1 relaxation data to show that the ^{17}O-NMR spin–lattice relaxation is mostly caused by spin fluctuations of the e_g-σ^* electrons in most RENiO$_3$ materials, and that these fluctuations increase strongly towards smaller rare-earths. Second, I will show that the transverse nuclear spin relaxation is dominated by spin–lattice relaxation, not spin–spin relaxation, except in the case of LaNiO$_3$.

5.3.1 Magnetic or quadrupolar relaxation mechanism

Since the bandwidth of the excitation pulses ($\sim 100\,\mathrm{kHz}$) is much smaller than the full width of the quadrupolar NMR spectrum including the satellite transitions (some MHz), all relaxation measurements must be performed selectively on one nuclear spin transition. This means that we are in the soft pulse limit of quadrupolar NMR. As discussed at length in section 4.6, the functional form of the inversion recovery curve depends on the transition under study and on the relaxation mechanism (magnetic or EFG fluctuations).

It is impossible to differentiate between magnetic and quadrupolar relaxation from measurements on only one transition, because the signal-to-noise ratio is insufficient to distinguish the two shapes of the relaxation curve. This is illustrated at the example of the inversion recovery curve of the ^{17}O central transition in LaNiO$_3$ at room temperature in figure 5.9. However, measurements on two different transitions at the same temperature will result in inconsistent values of T_1 if the wrong relaxation mechanism is assumed.

I have performed inversion recovery measurements in YNiO$_3$ at 290 K at both the central transition ($|-1/2\rangle \leftrightarrow |1/2\rangle$, 41.18 MHz) and the higher-frequency maximum of the first satellite transition spectrum ($|1/2\rangle \leftrightarrow |3/2\rangle$, 41.70 MHz). The experiments were performed during the same cooldown and the temperature was kept stable across all measurements. Fitting both datasets using the expressions for magnetic relaxation (equations 4.86 and 4.87) give $T_1^{CT} = 496 \pm 21\,\mu\mathrm{s}$ and $T_1^{1ST} = 515 \pm 15\,\mu\mathrm{s}$, which are

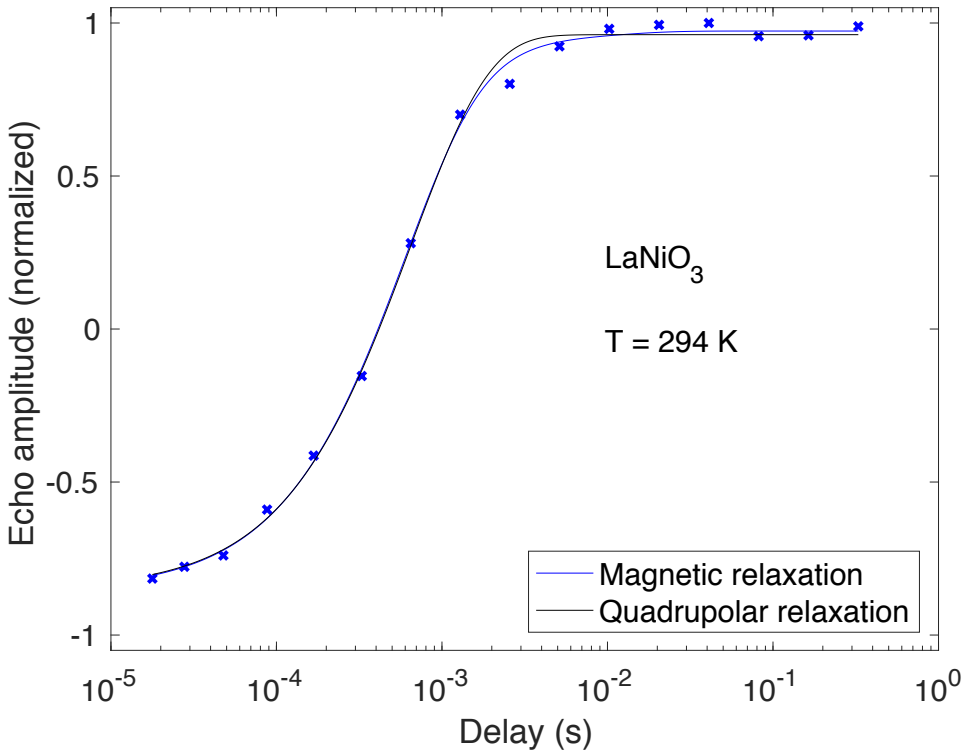

Figure 5.9: Inversion recovery curve of the central transition of ^{17}O in $LaNiO_3$ at room temperature. Both magnetic and isotropic quadrupolar relaxation models give a reasonable fit to the data. However, only magnetic relaxation gives consistent values for T_1 at both the central and the first satellite transitions (see text).

consistent within the error bar. Assuming isotropic quadrupolar relaxation instead, using equations 4.95 and 4.96 yields $T_{1,Q}^{CT} = 87 \pm 5\,\mu s$ and $T_{1,Q}^{1ST} = 132 \pm 5\,\mu s$, which are clearly inconsistent.

Also in $SmNiO_3$ I have performed T_1 measurements on both the central and first satellite transitions at various temperatures, in both the paramagnetic insulating and the metallic phase. In all cases, the fits assuming magnetic relaxation give consistent or almost consistent results. The results will be presented in section 5.6.

Based on these experimental findings, all further data analysis in this thesis will assume that spin–lattice relaxation in RENiO$_3$ is caused by purely magnetic fluctuations.

5.3.2 Longitudinal relaxation

The spin–lattice relaxation time T_1 of all NMR samples at room temperature (and for $SmNiO_3$ also at 493 K) are shown in figure 5.2. The data shown in this figure were obtained by measurements at the central transition of the ^{17}O-NMR spectra (figure 5.1). All T_1 measurements discussed in this section were performed by the inversion recovery method with spin-echo detection, as described in section 2.1.2.

Notice that the T_1 in $YNiO_3$ is very similar to that in lanthanide nickelates with RE^{3+} ions with similar radii, such as $DyNiO_3$ and $ErNiO_3$. This implies that the magnetic RE^{3+} ions do not contribute strongly to the spin–lattice relaxation. Relaxation due to a fluctuating EFG has already been excluded in the previous section. Thus, the only remaining coupling term in the Hamiltonian of the ^{17}O nuclear spins (equation 5.17) which can cause spin–lattice relaxation is the hyperfine interaction with e_g-σ^* electron spins. Since this interaction is dominated by the isotropic Fermi contact interaction, the spin–lattice relaxation should be isotropic.

An exception must be made for $GdNiO_3$, where the relaxation is dominated by the fluctuations of Gd^{3+} spins. Experimentally, the fluctuations of Gd^{3+} electronic magnetic moments are much slower than those of other lanthanide moments, which causes much faster nuclear spin relaxation [82]. The magnetic moment of Gd^{3+} is unique among the lanthanides because is a pure spin moment, i.e. it has no orbital contribution, unlike that of all other magnetic lanthanides [69, p. 306].

A clear and remarkable trend in the T_1 versus composition plot is that the relaxation in insulating phases is faster than in metallic phases. Normally, in a system with a MIT, the NMR relaxation rate is suppressed in the insulating phase as there are fewer excitations which can act as relaxation pathways, as seen in e.g. ^{31}P-NMR in RuP [83] or ^{63}Cu-NMR in $CuIr_2S_4$ [102]. Here instead, the opposite behaviour is observed, and relaxation becomes faster (slower) the further one moves towards the insulating (metallic) side of the diagram. This trend is also seen in temperature-dependent measurements

across the MIT in $SmNiO_3$, which will be discussed later in section 5.6. It indicates that in paramagnetic insulating RENiO$_3$, ^{17}O-NMR relaxation senses magnetic fluctuations which require the insulating phase. It is not yet clear how to reconcile the experimental facts that towards smaller rare-earth ions, T_1^{-1} increases while T_N decreases.

5.3.3 Transverse relaxation dominated by spin–lattice relaxation

Transverse relaxation was measured by the decay of the Hahn echo signal. The amplitude of the spin-echo signal $S(2\tau)$ measured with interpulse delay τ was determined by integration of its Fourier transform. As discussed in section 4.4, transverse relaxation has contributions from both spin–lattice relaxation and nuclear-spin–nuclear-spin interactions, c.f. equation 4.65. If spin–lattice relaxation is caused by isotropic magnetic fluctuations, then their contribution to the transverse relaxation of the central transition signal is given by equation 4.108.

In figure 5.10, the raw spin-echo decay $S(2\tau)$ is plotted for different RENiO$_3$ and compared to the spin–lattice contribution. The solid black line was computed as

$$S(2\tau) = a \cdot f_{SLR}(2\tau) + c, \tag{5.18}$$

with f_{SLR} from equation 4.108 and T_1 extracted from inversion recovery measurements performed under identical conditions as the spin-echo decay experiments. Thus, the amplitude a and small constant background c are the only free parameters. As can be seen in figure 5.10, this gives an excellent fit for all data except those from $LaNiO_3$. Since $LaNiO_3$ has the slowest relaxation rate of all RENiO$_3$ compounds (in a paramagnetic phase), we can conclude that in all materials except $LaNiO_3$, spin–lattice relaxation is so rapid that spin–spin relaxation is invisible. Spin–spin relaxation in $LaNiO_3$ is discussed below in section 5.4.2.

5.4 Fermi liquid behaviour in $LaNiO_3$

As one of the few nickelates with a diamagnetic rare-earth ion, $LaNiO_3$ is valuable for the NMR study of RENiO$_3$ as all magnetic effects here must come from the e_g-σ^* electrons. It also has the simplest physical properties of all RENiO$_3$ materials, as it remains a paramagnetic metal down to at least liquid helium temperatures. However, as already discussed in section 3.5, a controversial recent paper claimed to have found an antiferromagnetic transition in "twinned single-crystals" of $LaNiO_3$ at 157 K [49].

From the perspective of ^{17}O-NMR, $LaNiO_3$ is unique because the satellite transitions of the ^{139}La-NMR spectrum overlap with the ^{17}O-NMR spec-

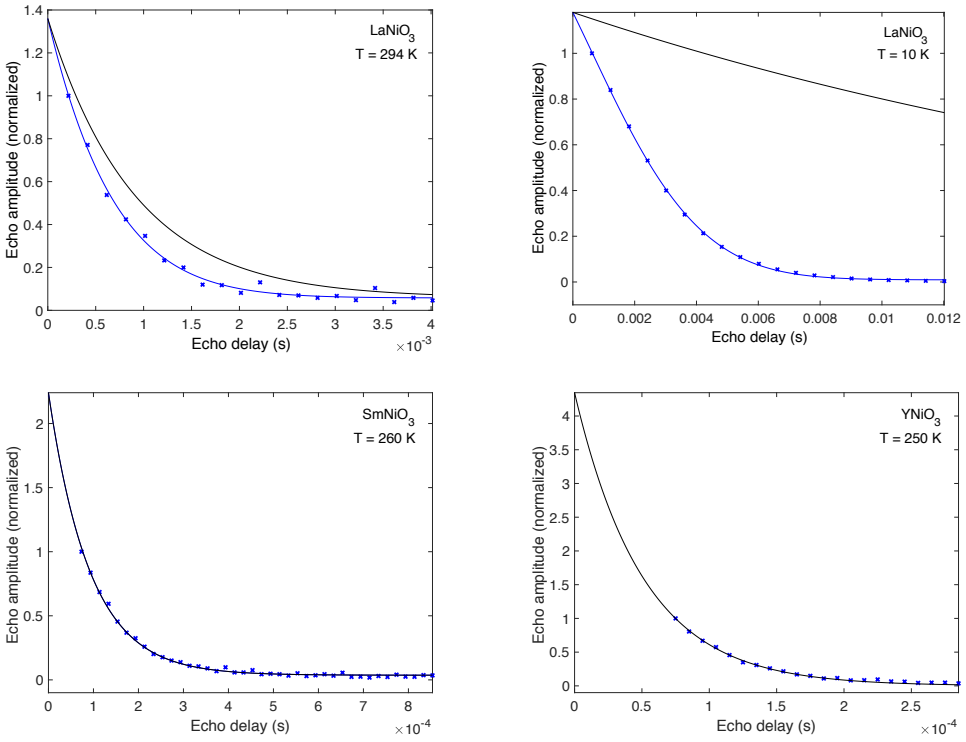

Figure 5.10: Some selected examples for spin–echo decay curves. The decay due to spin–lattice relaxation (black curve) fully explains the experimental data (blue crosses) in all cases except $LaNiO_3$. The fit for the $LaNiO_3$ data (blue curve) is discussed in section 5.4.2.

trum. I have focussed mostly on ^{17}O because the ^{17}O-NMR signal is stronger than the that of ^{139}La-NMR, c.f. figure 5.1.

Some ^{139}La-NMR data on $LaNiO_3$ have been known in the literature [124]. My ^{139}La-NMR measurements are in agreement with all experimental data from this paper — note however that the Knight shift given in this paper has the correct magnitude but the wrong sign, and all interpretations which rely on the sign of the shift are incorrect.

Due to the larger signal-to-noise ratio and narrow central transition spectrum, ^{17}O-NMR measurements in $LaNiO_3$ are more accurate than ^{139}La-NMR measurements. In this section, I report measurements of the (Knight) shift, spin–lattice relaxation, and spin–spin relaxation of ^{17}O, and some spin–lattice relaxation measurements on ^{139}La. The Knight shift and spin–lattice relaxation data are shown to be consistent with paramagnetic Fermi liquid behaviour at all temperatures. Spin–spin relaxation data could be fitted using a combined exponential and Gaussian relaxation, but their interpretation has remained impossible.

5.4.1 Korringa ratio and electronic correlations

Phenomenology of NMR in simple metals

In a simple metal, the magnetic susceptibility is temperature-independent, with an orbital contribution due to Landau diamagnetism and a spin contribution due to Pauli paramagnetism [69, p. 315ff]. In NMR, this is reflected in the "Knight" shift [70, 2, p. 199ff].

As shown in equation 4.40, the spin–lattice relaxation rate is proportional to temperature times the dynamical magnetic susceptibility. Thus, for a simple metal, T_1^{-1} is linear in temperature.

Since both Knight shift K and spin–lattice relaxation are caused by the hyperfine coupling to conduction electrons, they are related by the "Korringa relation" [73]

$$S_{exp} = \frac{K^2}{(T_1 T)^{-1}} \tag{5.19}$$

$$S_{th} = \frac{\hbar}{4\pi k_{\mathrm{B}}} \left(\frac{g\mu_{\mathrm{B}}/\hbar}{\gamma}\right)^2 \tag{5.20}$$

where $S_{exp} = S_{th}$ in the case of non-interacting conduction electrons weakly coupled to nuclei via an on-site hyperfine interaction.

In the case of interacting electrons, the spin susceptibility and density of states are renormalised according to Fermi liquid theory, which leads to a correction factor κ [2, p. 363f]

$$S_{exp} = \kappa S_{th}. \tag{5.21}$$

The Knight shift is a measurement of the DC magnetic susceptibility at wavevector $\vec{q} = 0$ and T_1^{-1} measures the low-frequency dynamic susceptibility across all wavevectors. Therefore, a large Korringa ratio $\kappa > 1$ implies enhanced susceptibility at zero wavevector due to electron–electron interactions, i.e. ferromagnetic correlations, whereas $\kappa < 1$ implies reduced susceptibility at zero wavevector, i.e. antiferromagnetic correlations.

If NMR measurements are performed on a ligand which does not participate in the metallic bonding, i.e. if there is no on-site hyperfine interaction, then κ contains also a factor of the coordination number of the ligand [6].

Isotropic Knight shift

The ^{17}O-NMR central transition spectrum could be acquired by spin-echo measurements at fixed RF frequency. The isotropic Knight shift K_{iso} was extracted from the first moment of the central transition spectrum assuming that the chemical shift can be neglected. As shown in figure 5.11, K_{iso} has some temperature dependence and a maximum at ca. 180 K. However, the changes with temperature are relatively small, which is consistent with K_{iso} being dominated by Pauli paramagnetism. The maximum at 180 K may also be present in the magnetic susceptibility of high-quality single-crystalline $LaNiO_3$ [139]. As already discussed based on ^{139}La-NMR measurements in reference [124], the absence of an upturn at low temperatures implies that any such feature observed in the bulk magnetic susceptibility must be due to impurities. Furthermore, this behaviour is inconsistent with claims of magnetic order in $LaNiO_3$ at 157 K made in reference [49].

Spin–lattice relaxation rate

The temperature-dependence of the spin–lattice relaxation rate measured at the central transition is plotted in Figure 5.12. It shows an almost linear temperature-dependence, as expected for a paramagnetic Fermi liquid. The absence of any feature near 157 K is in stark disagreement with the assertion of an antiferromagnetic phase transition at this temperature [49].

The Korringa ratio

The temperature-dependence of the Korringa ratio $\kappa = S_{exp}/S_{th}$ is plotted in figure 5.13. While it is constant ≈ 3 at high temperatures, in the range of 90 to 130 K there is a crossover to a lower value ≈ 2.6. At very low temperature, κ seems to decrease further.

These values for κ indicate weak ferromagnetic correlations among the conduction electron spins. This is consistent with previous reports of enhanced Pauli paramagnetism in the bulk magnetic susceptibility [129, 151]. In a model where only Ni-e_g electrons participate in the metallic bonding, the reference value for non-interacting electrons is equal to the coordination

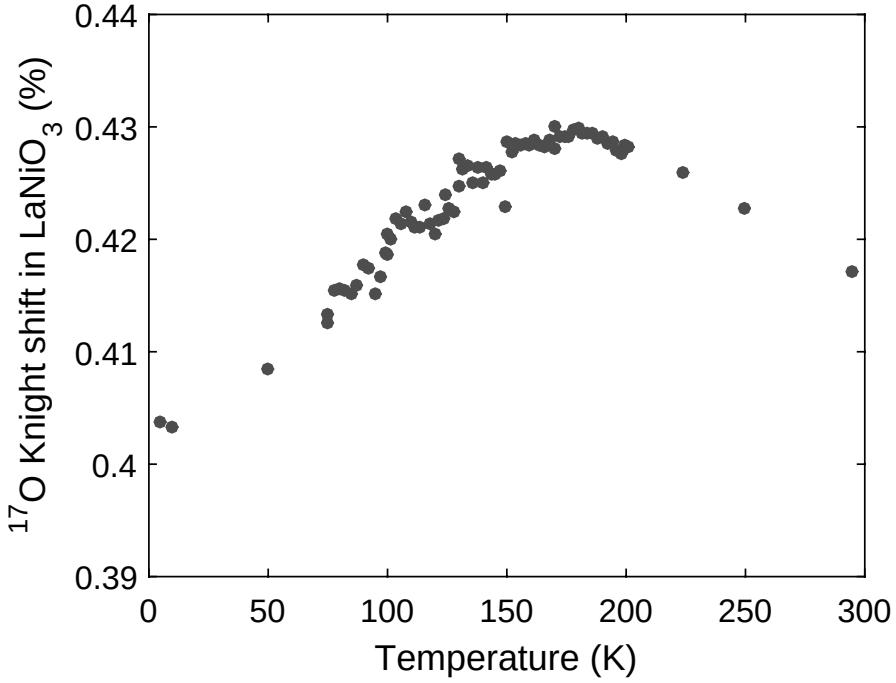

Figure 5.11: The isotropic ^{17}O Knight shift vs temperature in $LaNiO_3$ shows weak temperature dependence, with changes of less than 10 % of the total shift. This is consistent with the spin susceptibility being dominated by temperature-independent Pauli paramagnetism. There is a maximum around (180 K), which may be present also in the magnetic susceptibility of high-quality single-crystalline $LaNiO_3$ [139].

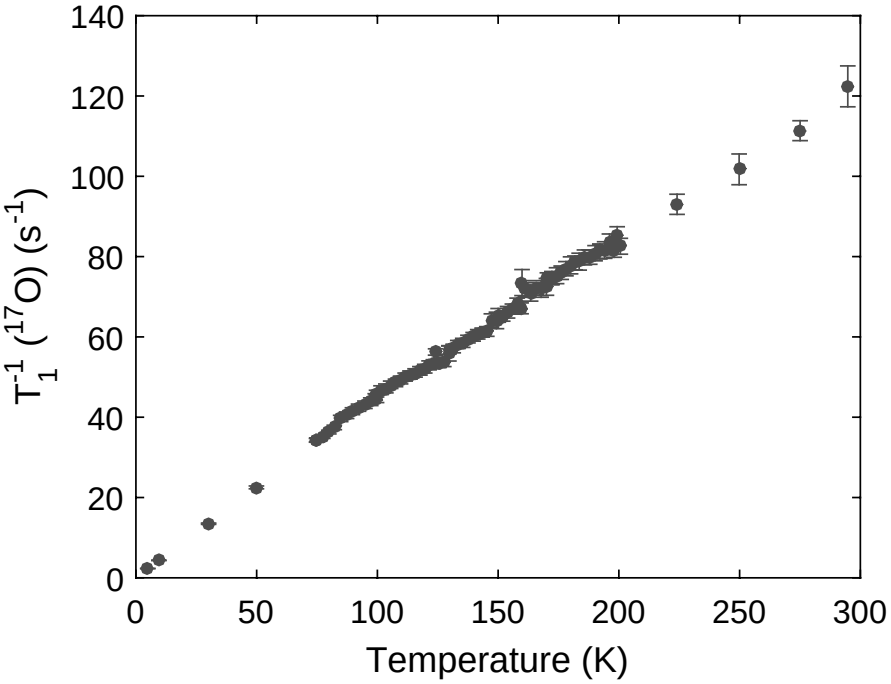

Figure 5.12: The spin–lattice relaxation rate in $LaNiO_3$ is nearly linear in temperature, which is expected for a Fermi liquid. Note the absence of any feature near the purported magnetic transition at 157 K [49].

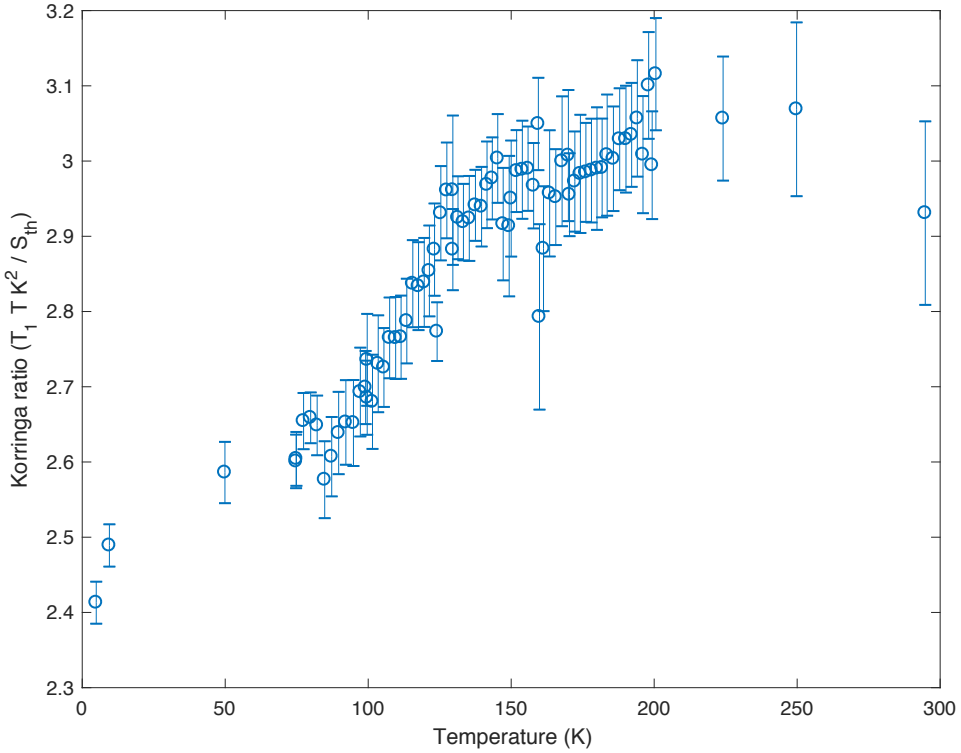

Figure 5.13: Korringa ratio $\kappa = S_{exp}/S_{th}$ of ^{17}O in $LaNiO_3$. A large ratio indicates that the K_{iso} is larger than expected from $1/T_1$, i.e. "ferromagnetic correlations".

number of oxygen by nickel: 2. If one more realistically assumes that the oxygen orbital hybridise strongly with the Ni-e_g orbitals (c.f. section 3.1), the reference value is 1. A more detailed interpretation of these experimental data will most likely have to account for the fermiology of $LaNiO_3$.

5.4.2 Spin–spin relaxation

Since the spin–lattice relaxation in $LaNiO_3$ is much slower than in all other nickelates, the spin-echo decay is affected by nuclear-spin–nuclear-spin interactions. I have been able to fit the spin-echo signal $S(2\tau)$, acquired using a Hahn echo sequence with interpulse delay τ, by the phenomenological expression

$$\begin{aligned} S(2\tau) &= A f_{SLR}(2\tau) f_{SSR}(2\tau) + c \\ &= A \exp(-9\,\frac{2\tau}{T_1}) \exp(-\frac{2\tau}{T_2'} - \frac{(2\tau)^2}{2T_{2G}^2}) + c, \end{aligned} \tag{5.22}$$

where, according to equation 4.65, $f_{SSR}(t)$ is the contribution of spin–spin relaxation and $f_{SLR}(t)$ is the contribution due to spin–lattice relaxation with

T_1 extracted from inversion recovery experiments, A is the signal strength, and c accounts for a possible background signal ($c \approx 0$ in all fits). The spin–lattice relaxation contribution was computed by assuming isotropic relaxation behaviour, which allows to make use of equation 4.108. For a phenomenological shape of $f_{SSR}(t)$, both an exponential and Gaussian contribution were necessary. Examples for the resulting fits at 294 and 10 K are shown as blue solid lines in figure 5.10. The two contributions have drastically different temperature-dependences shown in figure 5.14: $T_2'^{-1}$ is constant in temperature whereas T_{2G}^{-1} is affine linear in temperature. Error bars on $T_2'^{-1}$ and T_{2G}^{-1} contain the fit uncertainty as well as the uncertainty of T_1 from the inversion recovery fits. The error propagation of uncertain model parameters through the least-squares curve fitting procedure was performed according to the method of reference [15].

A Gaussian spin-echo decay may result from homonuclear spin–spin interactions in materials which are not isotopically pure, such that the number of neighbouring homonuclei is probabilistic [107]. Since our $LaNiO_3$ sample is only partially enriched with ^{17}O, this may explain the T_{2G} observed in our sample. Unfortunately, unlike copper, oxygen has no second isotope with nuclear spin. Therefore, it is impossible to test this hypothesis by comparisons with measurements of heteronuclear spin–spin interactions like in reference [107]. Thus, the only possible test is to measure T_{2G}^{-1} in samples of $LaNiO_3$ with varying concentrations of ^{17}O.

An exponential spin-echo decay can originate from mutual nuclear-spin-flips [107]. If the assumption of isotropic spin–lattice relaxation were incorrect, then this would also give rise to an additional exponential relaxation term, which would be linear in temperature in a Fermi liquid. Therefore, the experimental fact that $T_2'^{-1}$ is constant in temperature confirms that spin–lattice relaxation is isotropic.

5.4.3 ^{139}La-NMR results

While the focus of the experiments on $LaNiO_3$ has been on ^{17}O-NMR, I have obtained some results on ^{139}La-NMR. The ^{139}La-NMR spectrum at room temperature shown in figure 5.1, which overlaps with the ^{17}O-NMR spectrum, can be explained by an isotropic Knight shift and an axially symmetric EFG. Although an axially symmetric (Knight) shift anisotropy is allowed by the D_3 point group symmetry of La in rhombohedral $LaNiO_3$ (c.f. section 5.1), this term was not necessary to fit the experimental spectrum. The fitted values are

$$K_{iso} = 0.078\,\%, \quad C_Q = 18\,\mathrm{MHz}. \tag{5.23}$$

Like previously for ^{17}O, I have neglected the chemical shift. This approximation should work less well for ^{139}La than for ^{17}O, because for heavy elements such as lanthanum, typically chemical shifts cover a wider range,

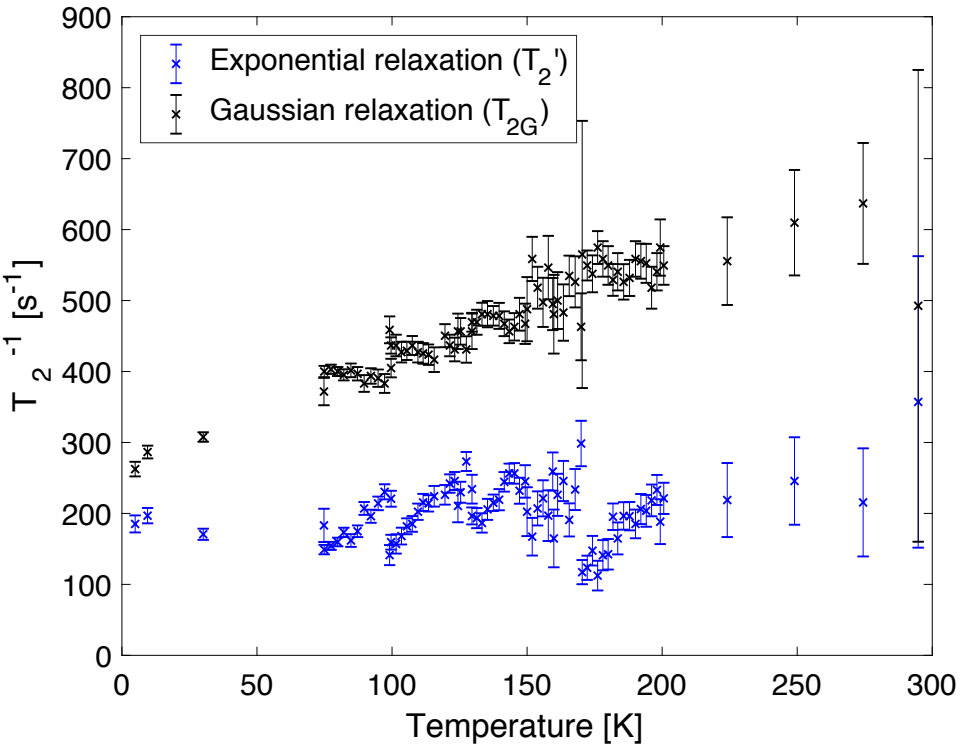

Figure 5.14: Exponential and Gaussian spin–spin relaxation rates $T_2'^{-1}$ and T_{2G}^{-1} in $LaNiO_3$, extracted from fits such as those shown in figure 5.10 after accounting for the spin–lattice contribution to the spin-echo decay. The apparent "oscillations" in the data are experimental artefacts which are correlated to the tuning of the NMR probe circuit.

and the experimental Knight shift is significantly smaller for ^{139}La than for ^{17}O

Unfortunately, reference [124] does not write out the precise numerical value of their Knight shift of ^{139}La in $LaNiO_3$. In their shift-versus-temperature plot, they graph values close to $-0.1\,\%$, which has a similar absolute value but opposite sign to our Knight shift. However, manually estimating the shift of the NMR spectrum shown in their paper shows that the Knight shift is positive. Thus, I assume that they accidentally reported Knight shift values with the wrong sign, and that my data is therefore consistent with theirs. Note that this means that parts of the discussion and interpretation in reference [124] must be disregarded, as they were reliant on the sign of the Knight shift.

An estimated "nuclear quadrupole frequency" $\nu_Q = 1.1\,\mathrm{MHz}$ has been reported based on the second-order quadrupole effect on the central transition spectrum [124]. Since my experimental data also include the satellite transitions, my estimate of the quadrupolar coupling constant can be expected to be more accurate. Converting my value of C_Q to an expected NQR frequency using equations 2.50 and 2.52 gives

$$\nu_Q = \frac{\omega_Q}{2\pi} = \frac{3C_Q}{2I(2I-1)} = 1.3\,\mathrm{MHz}, \tag{5.24}$$

which seems consistent with the reported value.

The results of temperature-dependent spin–lattice relaxation measurements of ^{139}La in $LaNiO_3$ are reported in Figure 5.15. Within the experimental error, the relaxation rate T_1^{-1} is perfectly linear in temperature, consistent with the Fermi liquid picture already obtained from ^{17}O-NMR. The numerical values are consistent with those from reference [124].

Compared to the ^{17}O-NMR data, the isotropic shift in ^{139}La is smaller by a factor ~ 5 and the spin–lattice relaxation rate T_1^{-1} is slower by a factor ~ 44. Generally, this reduction indicates that the hyperfine interaction of the conduction electrons with ^{139}La is much weaker than that with ^{17}O, implying that lanthanum orbitals contribute much less than oxygen orbitals to the states near the Fermi surface.

Based on the Korringa law, one expects T_1^{-1} to change proportionally to K^2, which does not seem to be the case here. There are two possible explanations for this discrepancy. The first is that the Korringa ratio for ^{17}O and ^{139}La may be fundamentally different. Due to the crystal structure, magnetic fluctuations at certain wavevectors which contribute strongly to the relaxation of ^{17}O may not contribute to that of ^{139}La. The possible alternative reasoning that lanthanum does not contribute many electrons to the states near the Fermi level and therefore the relaxation occurs via dipolar rather than contact hyperfine interactions does not work — in this case, the reduction of K_{iso}^2 should be larger than that of T_1^{-1}. Second is that the Knight shifts may be identified incorrectly due to the neglect of the

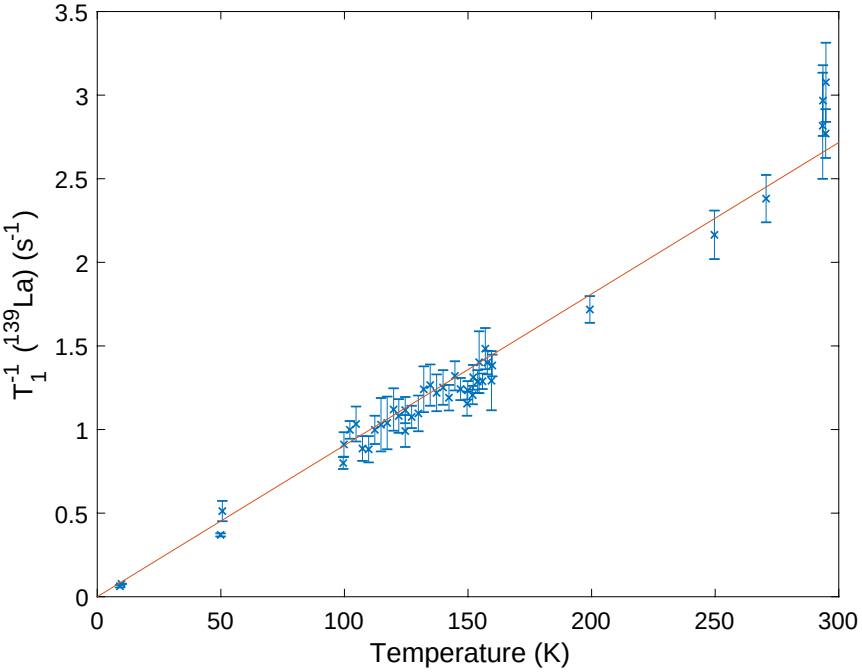

Figure 5.15: The spin–lattice relaxation rate of ^{139}La in $LaNiO_3$ is approximately linear in temperature, just like for ^{17}O. The data shown here are in agreement with previously published data [124].

chemical shift — if we assume zero chemical shift for ^{17}O, a chemical shift of only 150 ppm for ^{139}La is needed to get the same Korringa ratio for both nuclei.

5.5 Gapped magnetic excitation spectrum in $YNiO_3$

Like $LaNiO_3$, $YNiO_3$ has the advantage that its rare-earth ion does not carry a magnetic moment. While the metal–insulator transition temperature of $YNiO_3$ at $T_{MI} = 582\,\mathrm{K}$ is too high to be accessed with our NMR equipment, the antiferromagnetic transition at $T_\mathrm{N} = 152\,\mathrm{K}$ is easily accessible.

The isotropic shift of $YNiO_3$ between T_N and room temperature has been already been discussed in section 5.2.1, in order to estimate the hyperfine coupling constant in RENiO$_3$ using a Clogston–Jaccarino plot (figure 5.4).

Temperature-dependent measurements of T_1^{-1} are plotted in figure 5.16. Between ca. 154 K and room temperature, the relaxation rate is constant, as expected for a paramagnetic insulator. A sharp maximum occurs at $T_\mathrm{N} = 152\,\mathrm{K}$, with an enhanced T_1^{-1} within 2 K of the phase transition, consistent with the critical slowing-down of magnetic fluctuations at a continuous phase transition. In the antiferromagnetic phase, the temperature-dependence follows an activated behaviour, which is clearly visible in an Arrhenius plot in figure 5.17.

Spin–lattice relaxation rate measurements at 50 K and above used the inversion recovery method, while at 30 K and below I used the aperiodic saturation recovery pulse sequence discussed in section 2.1.2 in order to accelerate experiments despite the slow relaxation.

Nuclear magnetisation recovery curves above 150 K were fitted using the expression for relaxation of the central transition from equation 4.86. Below 145 K, the internal field due to magnetic order causes all transitions to overlap in the powder spectrum, and thus the magnetisation recovery must be fitted using equation 4.101 instead. Notice that the T_1^{-1} vs T graph shown in figure 5.16 is nicely continuous within the AF phase despite this change of fit function. In fact, if one erroneously keeps using the well-known expression from equation 4.86 even well below T_N, a large unphysical discontinuity appears between 145 and 150 K.

At low temperatures, the fits to the recovery curves had to be further modified to include "stretched exponential relaxation" by replacing all terms of the form

$$\exp(-\lambda t/T_1) \to \exp(-(\lambda t/T_1)^\beta) \tag{5.25}$$

in the fit function. Values for T_1^{-1} plotted in figures 5.16 and 5.17 at temperatures below 65 K were extracted by this method. Using this fit function for all relaxation curves obtained below T_N yields the temperature-dependence of β shown in figure 5.18.

The datapoint at 5 K must be considered nothing more than an upper bound on T_1^{-1}. Here, relaxation becomes so slow and stretched that it was impossible to acquire a full saturation recovery curve within a single cooldown of our flow cryostat, even when supplying it with a 100 l liquid helium tank. Thus, the large apparent deviation from the Arrhenius law at 5 K in figure 5.17 may be an experimental artefact.

Stretched exponential relaxation, with the stretching exponent $\beta \leq 1$, is a phenomenological model for processes governed by a broad distribution of relaxation times [84, 98]. In magnetism, it is commonly associated to disordered systems such as spin glasses [112]. However, in an antiferromagnetic powder, a distribution of relaxation times may occur at low temperatures, if magnetic fluctuations and spin–lattice relaxation become anisotropic when the ordered magnetic moment comes close to saturation. This may explain the temperature-dependence of β from figure 5.18, since $\beta \approx 1$ above ~ 65 K while relaxation becomes increasingly stretched towards lower temperature.

The Arrhenius law for spin–lattice relaxation in the antiferromagnetic phase

$$T_1^{-1} \propto \exp(-\frac{\Delta}{T}) \tag{5.26}$$

holds over four decades in T_1^{-1}, and strong deviations at low temperatures may be caused by the experimental issue described above. Such a stable activated behaviour is a clear signature of a gapped magnetic excitation spectrum. The magnitude of the fitted gap $\Delta = 29.7$ meV is surprisingly large in a relatively isotropic system like the rare-earth nickelates.

Resonant inelastic X-ray scattering (RIXS) on antiferromagnetic $NdNiO_3$ films have also found a gapped magnetic excitation spectrum, with the lowest experimental signal found at 17 meV [85], and analogous measurements on $PrNiO_3$ films have given similar results [36]. Therefore, the NMR relaxation results on $YNiO_3$ indicate that the magnetic excitation gap is larger in bulk nickelates with small rare-earths than in nickelate films with large rare-earths, and are in qualitative agreement with the RIXS results.

5.6 Evolution of magnetic fluctuations across T_{MI} and T_N in $SmNiO_3$

Among the stoichiometric $RENiO_3$ with $T_{MI} \neq T_N$, $SmNiO_3$ has the lowest T_{MI} of only 400 K. Its neighbour in the phase diagram (figure 3.1), $EuNiO_3$, already has $T_{MI} = 463$ K [11]. Since the highest temperatures accessible with our cryostats is 500 K, $SmNiO_3$ is the only material with $T_{MI} \neq T_N$ for which measurements well into the metallic phase are possible in our laboratory.

An additional argument for studying $SmNiO_3$ instead of $EuNiO_3$ lies in the J-multiplet and crystal-field structure of Eu^{3+} — the three states

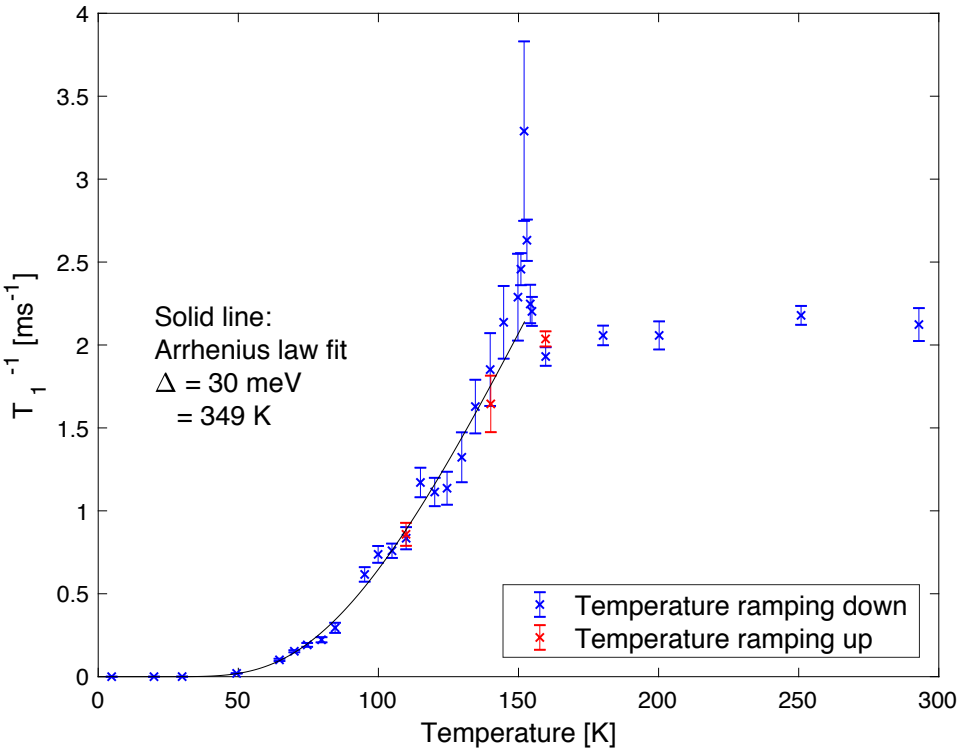

Figure 5.16: Spin–lattice relaxation rate versus temperature in $YNiO_3$. The constant behaviour in the paramagnetic phase and maximum at the magnetic phase transition is typical of magnetic insulators. In the antiferromagnetic phase, T_1^{-1} shows activated behaviour over a wide temperature range, which indicates a gapped magnetic excitation spectrum. The datapoint at 5 K is unreliable, and must be considered an upper bound to T_1^{-1} (see text for explanation).

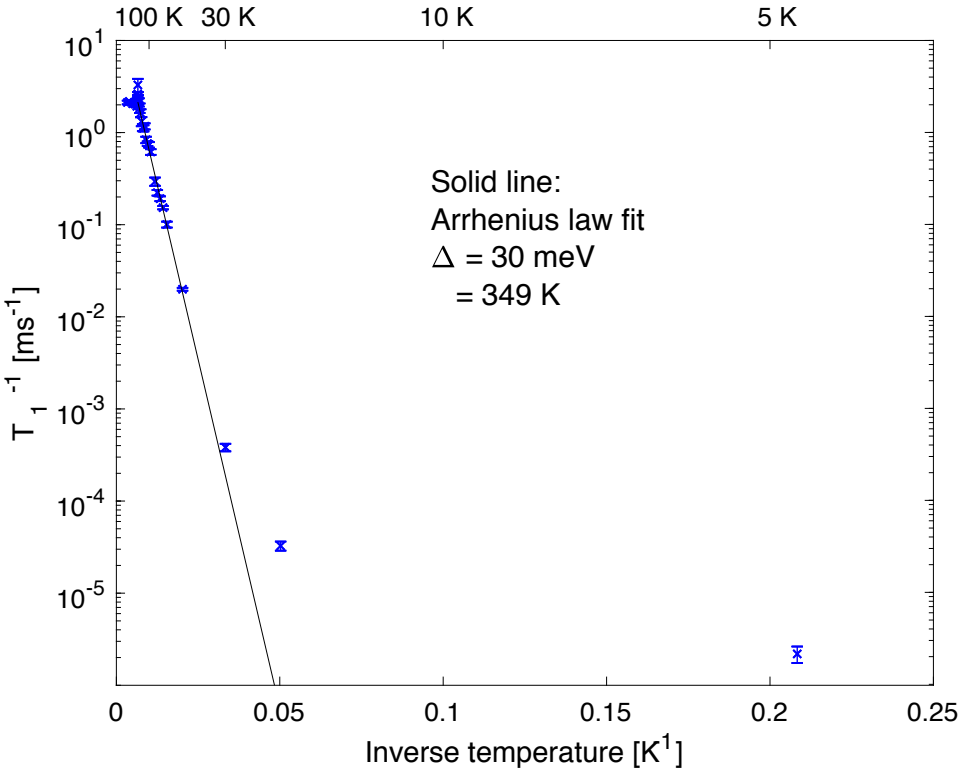

Figure 5.17: Arrhenius plot for T_1^{-1} in $YNiO_3$, clearly showing the activated temperature dependence of the spin fluctuations over several decades in T_1^{-1}. Activated behaviour of T_1 in a magnetically ordered phase is a hallmark of a gapped magnetic excitation spectrum. The datapoint at 5 K must be considered nothing more than an upper bound to T_1^{-1} (see text). The magnitude of the gap is surprisingly big for a relatively isotropic magnetic system such as $RENiO_3$, but it is in qualitative agreement with RIXS measurements on films of $NdNiO_3$ and $PrNiO_3$ [85, 36].

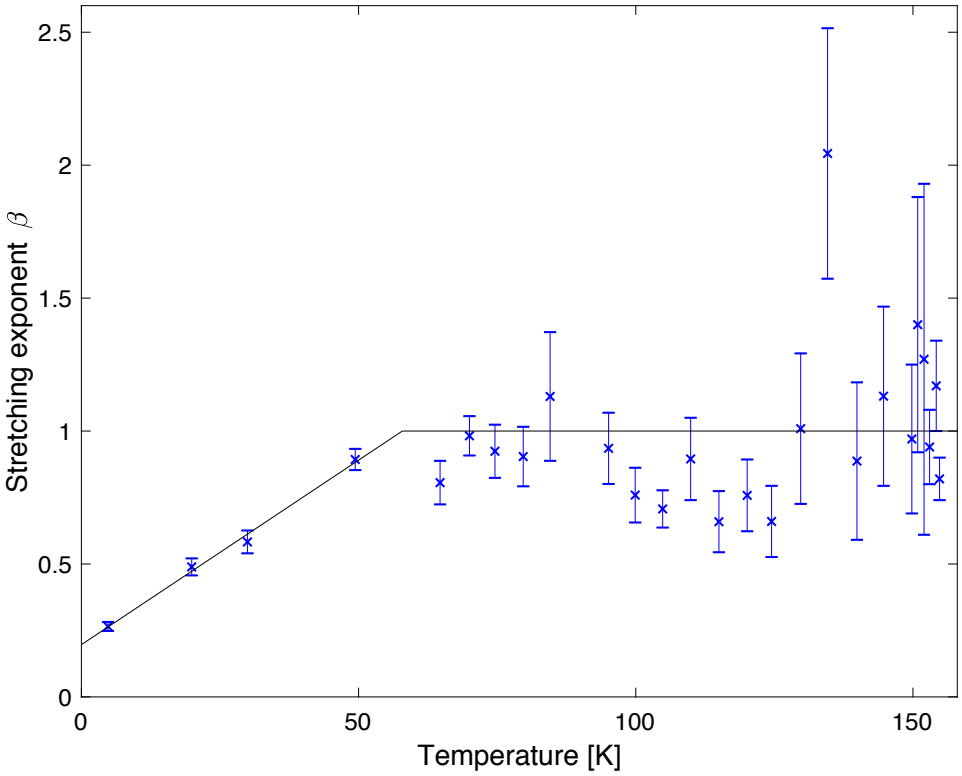

Figure 5.18: Stretching exponent β for $YNiO_3$ T_1 measurements. Values of β below 1 indicate broad distributions of the T_1 relaxation rate. In RENiO$_3$ powders, this might be caused by an anisotropic relaxation rates in the antiferromagnetic phase. Values of β larger than 1 are unphysical. The solid line is a guide to the eye. At temperatures of 65 K and higher, the values of T_1 reported above were estimated by enforcing $\beta = 1$ while fitting the inversion recovery data.

of the $J = 1$ lie only 400 K, 508 K, and 707 K above the $J = 0$ ground state [122]. Thus, in measurements between room-temperature and 500 K, a large change in the magnetic properties of the Eu^{3+} ion is expected as the $J = 1$ multiplet becomes thermally populated. This could make it difficult to assign temperature-dependent changes of the NMR shift and relaxation to the e_g-σ^* electron system or the Eu^{3+} ions. Meanwhile, $SmNiO_3$ has the advantage that near room temperature, Sm^{3+} causes the smallest isotropic contact shift of all RE^{3+} ions with partially occupied $4f$ shell, see figure 5.5 and reference [46].

As already discussed in section 2.1.8, I have built an NMR insert capable of withstanding 500 K for the high-temperature measurements in $SmNiO_3$, a photograph of which is shown in Figure 2.1. All measurements between room temperature and 500 K were performed with this high-temperature setup. Measurements between room temperature and 5 K used the same setup as all other ^{17}O-NMR measurements discussed in this chapter.

5.6.1 Isotropic shift

The isotropic shift between $T_N = 221$ K and 500 K is plotted in figure 5.19. Below T_N, the shift becomes a meaningless parameter due to the gigantic broadening of the powder spectrum due to antiferromagnetic order. Experimental data taken at 215 K, i.e. only 6 K below T_N, are shown in figure 5.20.

Note that unlike in $LaNiO_3$, the shift in the metallic phase is strongly temperature dependent. In fact, it seems to follow a similar trend as in the insulating phase. This is inconsistent with a Fermi liquid picture of the metallic state in $SmNiO_3$, and instead indicates that the magnetic behaviour of the e_g-σ^* electron system is dominated by localised moments even in the metallic phase.

This picture has already been suggested based on measurements of the bulk magnetic susceptibility contribution of the e_g-σ^* electron system in $SmNiO_3$ [110]. In this paper, the magnetic susceptibility of perovskite $SmScO_3$ was used to subtract the contribution of the Sm^{3+} sublattice in $SmNiO_3$. After this subtraction, a Curie-Weiss law was found in the paramagnetic insulating phase as expected, whereas a Curie law (i.e. a Curie-Weiss temperature of zero) with a slightly reduced magnetic moment was found in the metallic phase. Their interpretation is that even in the metallic phase of $SmNiO_3$, the e_g-σ^* electrons are partially localised, which is consistent with my NMR shift data.

5.6.2 Spin–lattice relaxation

Methods

The spin–lattice relaxation rate measured by inversion recovery between 5 and 500 K is plotted in figure 5.21. Above 213 K, all the inversion recovery

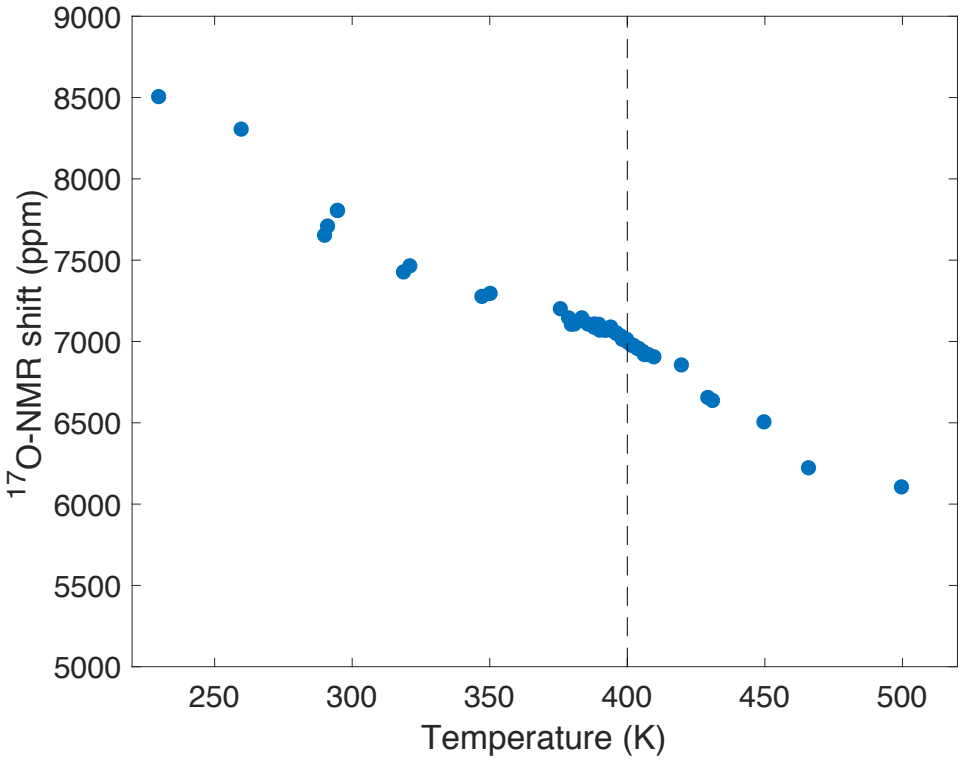

Figure 5.19: Isotropic shift vs temperature in $SmNiO_3$. The vertical dashed line indicates the metal–insulator transition. Note that even in the metallic phase, the shift is strongly temperature-dependent. This is in stark contrast to the behaviour in $LaNiO_3$, where the shift is dominated by temperature-independent Pauli paramagnetism, see figure 5.12.

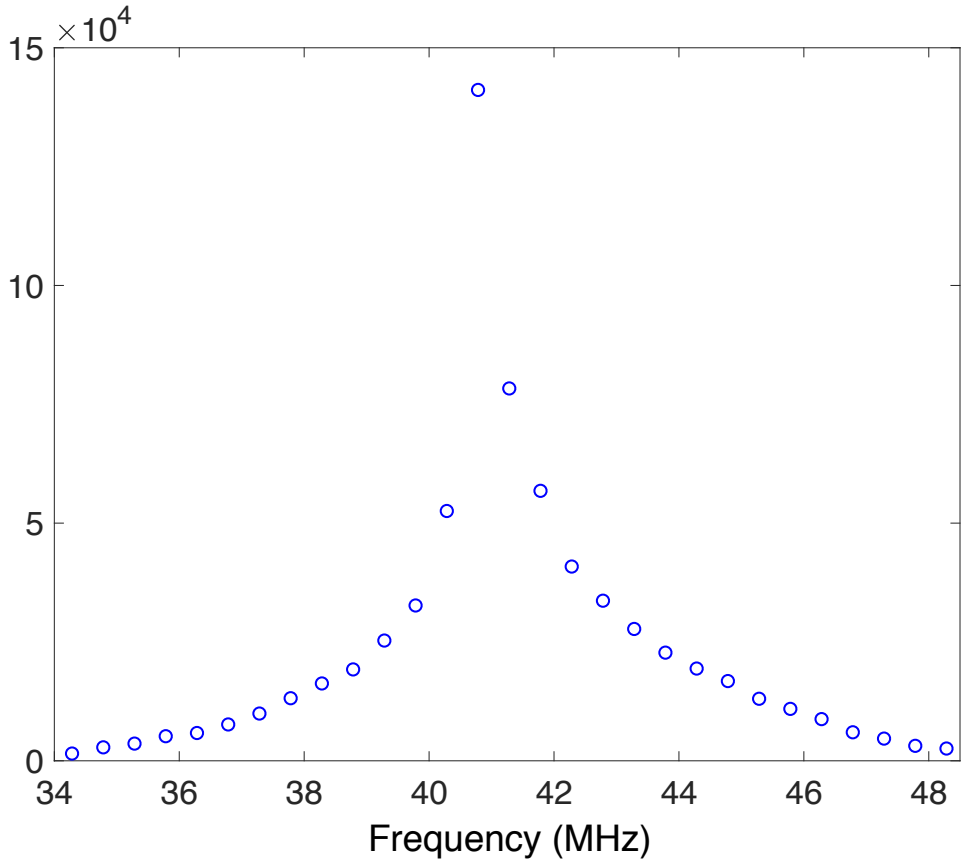

Figure 5.20: NMR spectrum of $SmNiO_3$ at 215 K, 6 K below the antiferromagnetic transition. Due to the large width and weak signal, the spectrum could not be acquired by the usual method. The amplitude shown here was calculated by integrating the Fourier-transformed spin-echo signal, acquired with different RF carrier frequencies.

curves were fitted using the expression for magnetic relaxation of the central transition from equation 4.86. At some temperatures in the paramagnetic insulating and metallic phases, measurements were also performed at the maxima of the first satellite transitions, for which equation 4.87 was used instead. As already discussed in section 5.3.1, the values for T_1 obtained from both transitions are similar or equal at all temperatures, consistent with the assumption of isotropic spin–lattice relaxation by magnetic fluctuations. Below 213 K, I used the expression for relaxation in antiferromagnetic powders in equation 4.101 instead. The threshold value of 213 K was selected because here a clear unphysical discontinuity in T_1^{-1} appears when the incorrect fit function is used, and because a threshold slightly below T_N is physically reasonable.

As seen in the room temperature spectrum in figure 5.1, there is a small impurity signal in our $SmNiO_3$ sample near zero shift. Most likely, this originates from a Sm_2O_3 impurity phase, as this compound is used as a starting material in the synthesis of $SmNiO_3$ [11] and has nearly zero ^{17}O-NMR shift [145]. In the paramagnetic phases, this is not a problem since the signal from $SmNiO_3$ is much stronger than the impurity signal. In the antiferromagnetic phase however, the $SmNiO_3$ signal is drastically broadened, such that at low temperatures the impurity signal dominates over the $SmNiO_3$ signal. Since the most likely impurity phase, Sm_2O_3, is known to remain paramagnetic down to at least 2 K [94], its NMR signal should not change qualitatively in the temperature range under study here. Therefore, all relaxation measurements below 210 K were performed at 45.8 MHz, which is far from the impurity signal. Measurements between 210 K and T_N instead used a carrier frequency of 41.13 MHz, near the central transition of the paramagnetic insulating phase. At 210 K, the values for T_1 obtained at the two different frequencies are equal within the error bar.

Results and discussion

The temperature-dependence of the spin–lattice relaxation rate in $SmNiO_3$ shown in figure 5.21 is remarkable for several reasons.

Starting from high temperatures, T_1^{-1} in the "metallic" phase is constant, rather than linear in temperature as in $LaNiO_3$ (c.f. figure 5.12). This behaviour is typically caused by localised moments in paramagnetic insulators, as seen in $YNiO_3$ in figure 5.16. If this behaviour were caused by the Sm^{3+} moments, then an additional Fermi-liquid-like component with similar magnitude as that in $LaNiO_3$ would be expected, which is clearly not present in the experimental data. Furthermore, T_1^{-1} around 100 K, where fluctuations of e_g-σ^* electrons are partially suppressed by magnetic order but Sm^{3+} ions remain paramagnetic, is lower than in the metallic phase by a factor of 2. Thus, also NMR relaxation in the metallic phase does not follow Fermi liquid behaviour but indicates the presence of localised magnetic moments in

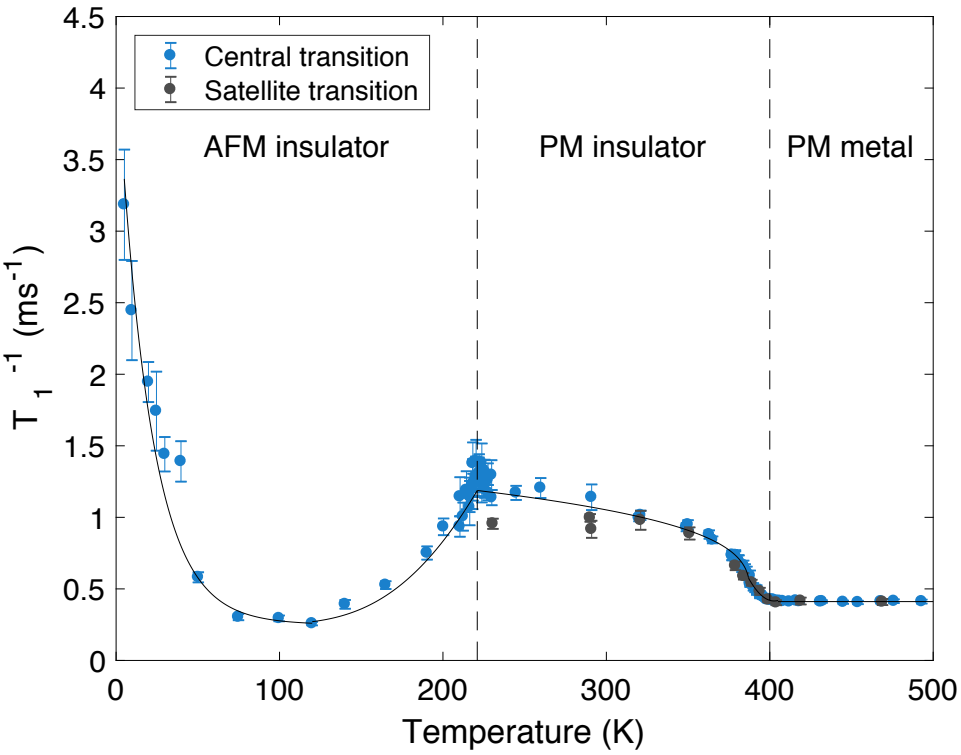

Figure 5.21: Spin–lattice relaxation rate in $SmNiO_3$, showing a highly unusual temperature dependence. Assuming a magnetic relaxation mechanism (see text), values of T_1^{-1} obtained from the central transition and the first satellite transitions are consistent in both paramagnetic phases. In the metallic phase of $SmNiO_3$, T_1^{-1} is constant in temperature, which indicates localised rather than itinerant magnetic moments. Since there is no peak at T_{MI}, the MIT cannot be driven by magnetic fluctuations — instead, the MIT is a prerequisite to the magnetic fluctuations seen in the PI phase. The upturn at low temperatures is due to the magnetic moment of Sm^{3+}.

the e_g-σ^* electron system, just like the NMR shift (see section 5.6.1) and the bulk magnetic susceptibility (see reference [110]). This picture is consistent with reports of "bad metal" behaviour in electrical transport measurements in films of $SmNiO_3$ [62].

In the paramagnetic insulating phase, a new relaxation pathway seems to appear, as seen from the clear increase in T_1^{-1} below T_{MI}. Thus, there are magnetic fluctuations which occur only in the insulating phase. This observation allows us to rule out any theoretical mechanism for the metal–insulator transition in which the transition is driven by magnetic fluctuations [79], at least for all nickelates with $T_{MI} \neq T_N$. In section 5.7, this conclusion will be extended to all RENiO$_3$ based on measurements in $PrNiO_3$. We can also draw an important conclusion regarding the antiferromagnetism at the unusual wavevector $\vec{k} = (1/2, 0, 1/2)$ (or $\vec{k}_{pc} = (1/4, 1/4, 1/4)$ in pseudocubic notation) below T_N. Remembering that magnetic order in RENiO$_3$ only occurs in the insulating state (see the phase diagram in figure 3.1), we can deduce that *the insulating phase is a prerequisite to the magnetic fluctuations* at this wavevector.

At $T_N = 221\,K$, there is a maximum in T_1^{-1}, although it is not as clear as in $YNiO_3$ (see figure 5.16). Below, T_1^{-1} decreases as the magnetic fluctuations freeze out in the antiferromagnetic phase. Far into the antiferromagnetic phase, below 100 K, there is a drastic increase in T_1^{-1} caused by fluctuations of the Sm^{3+} moments. Most likely, the Sm^{3+} moments order magnetically somewhere below 5 K. However, no further research on the possible magnetism of Sm^{3+} in $SmNiO_3$ at very low temperatures was performed as part of this thesis.

5.7 The discontinuous phase transition in $PrNiO_3$

After ^{17}O-NMR measurements in $LaNiO_3$, which remains metallic at all temperatures, and $YNiO_3$ and $SmNiO_3$, for which $T_{MI} > T_N$, the remaining case of $T_{MI} = T_N$ was covered by experiments on $PrNiO_3$.

In the metallic phase, the central transition shifts substantially towards higher frequencies as one cools from room temperature towards $T_{MI} = T_N = 130\,K$, see figure 5.22. Thus, from the perspective of the NMR shift, metallic $PrNiO_3$ acts unlike the Fermi liquid $LaNiO_3$ but similar to metallic $SmNiO_3$ where electrons are partially localised. This is consistent with resistivity measurements showing Fermi liquid behaviour in bulk $LaNiO_3$ and non-Fermi liquid behaviour in bulk $PrNiO_3$ [150].

The results of spin–lattice relaxation measurements are shown in figure 5.23. All results were obtained from inversion recovery experiments. Below the discontinuous transition, I have performed measurements at two different frequencies, in order to handle possible coexistence of antiferromagnetic and paramagnetic phases. The first frequency is 41.2 MHz, where

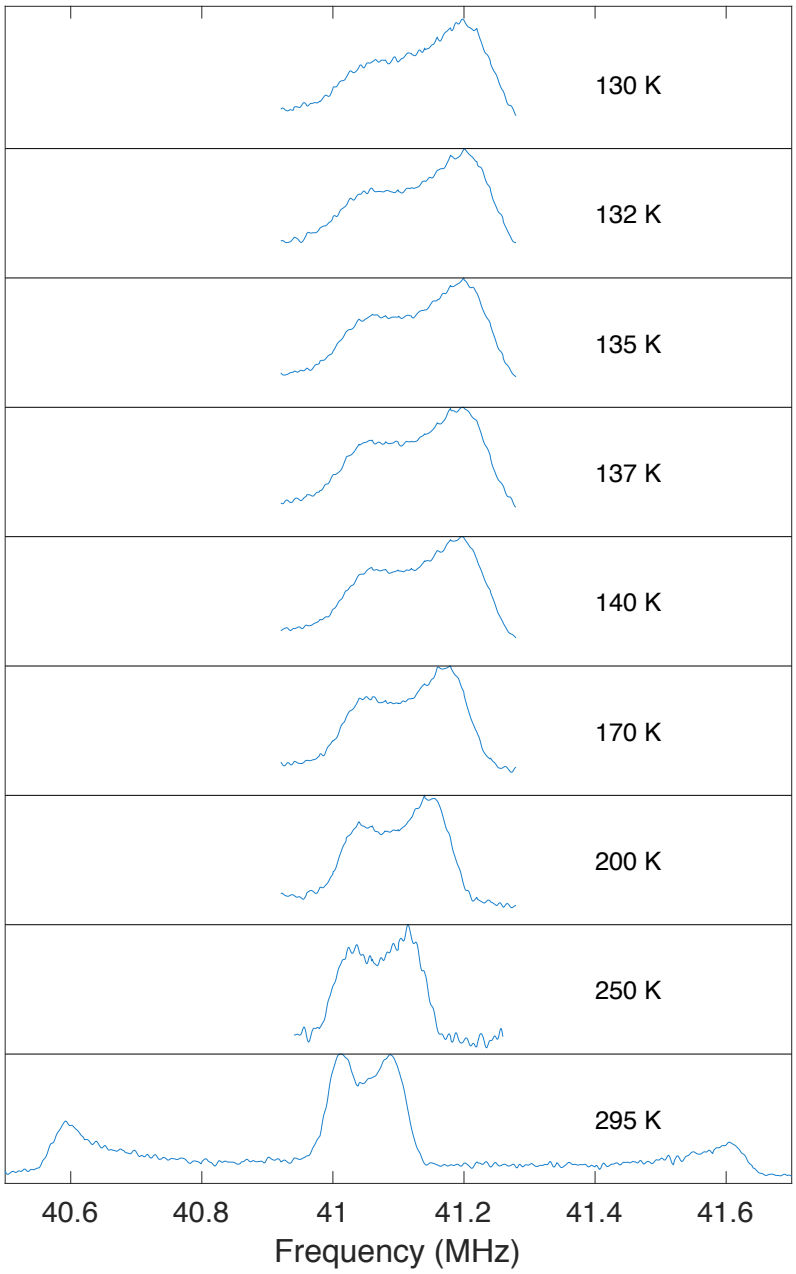

Figure 5.22: NMR spectra of $PrNiO_3$ in 7.0669 T at different temperatures in the paramagnetic metallic phase. Notice that the central transition shifts significantly towards higher frequencies for lower temperatures. Thus, the shift in metallic $PrNiO_3$ behaves like in $SmNiO_3$, where local moments persist into the metallic phase, and unlike in the Fermi liquid $LaNiO_3$.

the central transition was located in the metallic phase, and the second is 44 MHz, well outside the quadrupolar powder pattern of the metallic phase. At 41.2 MHz, inversion recovery curves were fitted using the formula for relaxation of the central transition (equation 4.86) above 104 K and using the expression for antiferromagnetic powders (equation 4.101) below 100 K. At 44 MHz, where only the antiferromagnetic phase can contribute, I have used equation 4.101 up to 130 K, where the signal at this frequency vanishes. A stretched-exponential fit as described in equation 5.25 was used at 25 K and lower temperatures. The temperature-dependence of the stretching exponent β is plotted in figure 5.24.

In the metallic phase, T_1 measurements at both maxima of the central transition spectrum yielded identical results. The two maxima originate from crystallites with different orientations with respect to the applied field, and are caused by the anisotropic shift and second-order quadrupole effect. Thus, this demonstrates that in the metallic phase, spin–lattice relaxation is isotropic. Unlike in metallic $SmNiO_3$, T_1^{-1} is temperature-dependent in $PrNiO_3$, it is however clearly not linear in temperature as in a Fermi liquid such as $LaNiO_3$. The average slope $\langle \Delta T_1^{-1}/\Delta T \rangle$ for $PrNiO_3$ is $\sim 0.5\,\mathrm{s}^{-1}/\mathrm{K}$, which is very similar to the value of $0.4\,\mathrm{s}^{-1}/\mathrm{K}$ for $LaNiO_3$. Note however that the T_1^{-1} versus T graph for $PrNiO_3$ shows a fairly strong curvature in the metallic phase, with a reduced slope at higher temperatures. Thus, from NMR relaxation measurements, it seems that the metallic state in $PrNiO_3$ is an intermediate case between the Fermi liquid state of $LaNiO_3$ and the partially localised metallic state of $SmNiO_3$.

If the simultaneous metal–insulator and antiferromagnetic transition in $PrNiO_3$ were a spin-density wave (SDW) transition as claimed in reference [79], then it would be driven by antiferromagnetic fluctuations, which should cause an increase in T_1^{-1} when cooling towards the transition. Instead, in figure 5.23 one can see that T_1^{-1} above the transition curves downwards upon cooling. This demonstrates that the phase transition in $PrNiO_3$ cannot be a SDW transition. Thus, the result from $SmNiO_3$ that magnetic fluctuations play no major role in the MIT has been extended to the case where $T_{MI} = T_\mathrm{N}$. Towards small rare-earths, the separation between T_{MI} and T_N in RENiO$_3$ increases (see figure 3.1), thus this result from large ($PrNiO_3$) and medium-sized ($SmNiO_3$) rare-earths is likely to hold across the entire phase diagram of RENiO$_3$.

Within the antiferromagnetic phase, T_1^{-1} at the centre of the spectrum decreases continuously below the transition. There is a large difference between T_1^{-1} at the centre of the spectrum and at 44 MHz across a wide temperature range, they only agree far below the transition. Above the phase transition at 130 K, the signal at 44 MHz vanishes as there are no longer any nuclei experiencing magnetic order. At both frequencies, the experimental inversion recovery curves agree well with the model functions for a unique relaxation rate, thus there is no (wide) distribution of T_1^{-1} at both

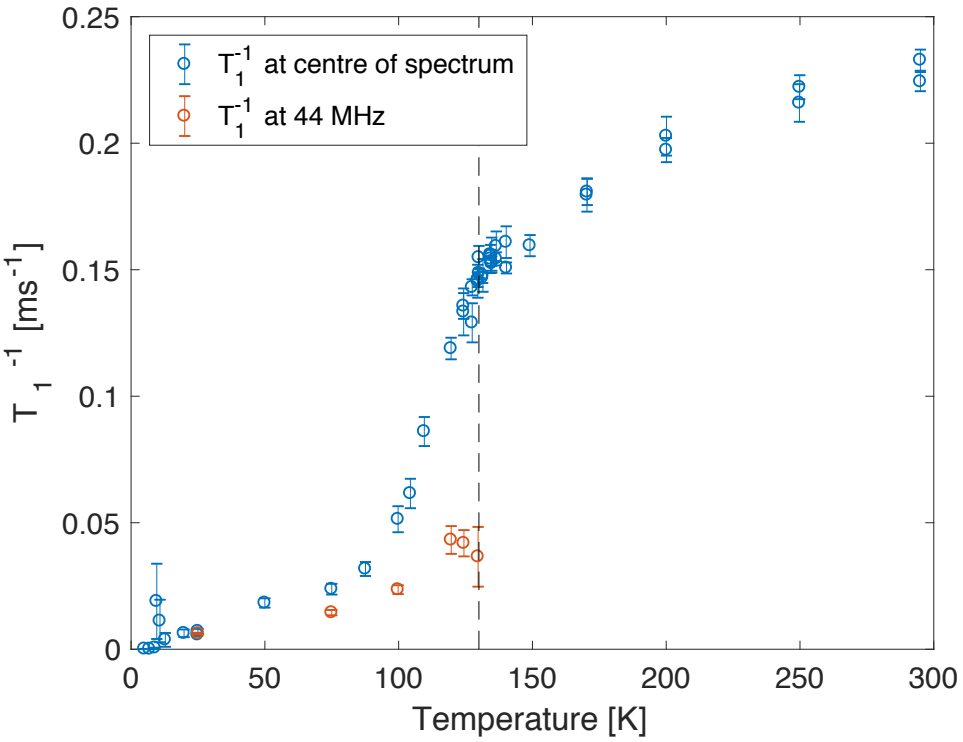

Figure 5.23: Spin–lattice relaxation rate in $PrNiO_3$, measured at both maxima of the central transition above $T_{MI} = T_N = 130\,K$, and at 41.2 and 44 MHz in the AF phase. The vertical dashed line indicates the transition temperature. No history-dependence of T_1^{-1} was observed, and thus data from heating and cooling runs have been merged. This figure shows that for nuclei, whose resonance frequency in the AF phase lies near the centre of the spectrum, T_1^{-1} is continuous across the transition, whereas for other nuclei, T_1^{-1} is discontinuous at $T_{MI} = T_N$. The peak near 10 K likely originates from the Pr^{3+} moments, since the e_g-σ^* electron system is magnetically ordered at such low temperatures.

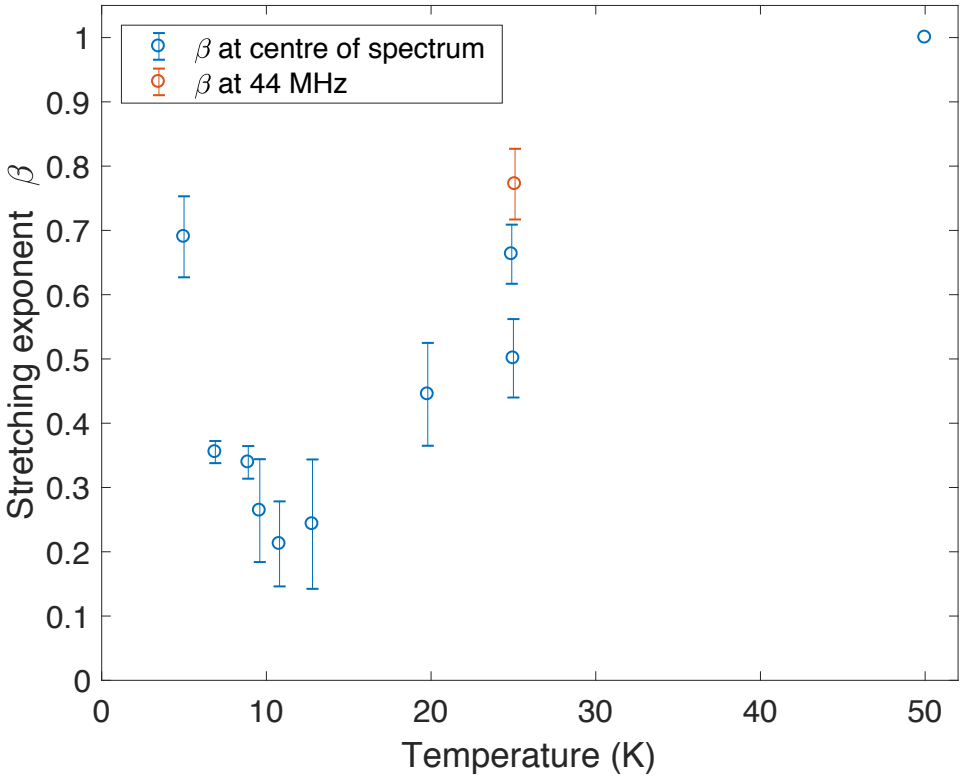

Figure 5.24: Stretching exponent β in $PrNiO_3$ at low temperatures. At 50 K and higher, a good fit to the inversion recovery curves could be obtained without any stretching, i.e. $\beta = 1$. Blue points were extracted from measurements at an RF carrier frequency of 41.2 MHz, whereas the red point was obtained at 44 MHz. Here, the anomaly in T_1^{-1} at 10 K is reflected as a dip in β, which indicates a decrease in data quality around this temperature caused by rapid relaxation at this temperature.

frequencies. There is no visible dependence on thermal history. A speculative interpretation of this phenomenology is that for nuclei experiencing a large internal field due to magnetic order, T_1^{-1} is discontinuous at the phase transition. For nuclei which couple less strongly to the magnetic order parameter, however, T_1^{-1} is continuous. At a discontinuous phase transition, there is no physical reason for T_1^{-1} to change continuously. In a recent paper on nanoscale near-field infrared measurements on epitaxial $NdNiO_3$ films, it was found that the phase transition at $T_{MI} = T_N$ globally behaves as a discontinuous transition; however, in local measurements near (most likely antiferromagnetic) domain walls, scaling behaviour which is characteristic of a continuous MIT was observed [116]. Perhaps, such a "locally continuous" behaviour could explain the behaviour of T_1^{-1} below the phase transition in $PrNiO_3$.

Near 10 K, there is a peak in T_1^{-1} and a minimum in the stretched-exponential parameter β. Since the e_g-σ^* electron system is magnetically ordered at these low temperatures, this peak might be caused by fluctuations of the magnetic moments of Pr^{3+}. Because the signal amplitude in antiferromagnetic $RENiO_3$ powders is generally low due to the large width of the spectrum, the rapid relaxation around 10 K causes a problematic decrease in signal quality, which may explain the minimum of β around this temperature. However, it must be noted that the Pr^{3+} ion has an even number of $4f$ electrons and thus, unlike Sm^{3+}, its crystal-field ground state is a singlet which is separated from the first excited crystal-field level by a gap of 6.4 meV [121]. Thus, in order to find the physical origin of the feature at 10 K, further measurements using different experimental techniques will be necessary.

5.8 Conclusion and Outlook

In this chapter, ^{17}O nuclear spin Hamiltonian in $RENiO_3$ has been decomposed in terms of a hyperfine interaction with e_g-σ^* electrons, a combination of dipolar and transferred hyperfine interaction with RE^{3+} ions, and a quadrupolar coupling term. The quadrupolar coupling constant is approximately constant across the metal–insulator transition in $RENiO_3$, which seems to be in contradiction with claims of full charge disproportionation of the nickel ions. Spin–lattice relaxation is dominated by spin fluctuations of the e_g-σ^* electrons in all $RENiO_3$ except $GdNiO_3$, where spin fluctuations of the Gd^{3+} ions dominate instead.

Temperature-dependent were performed in selected materials: in $LaNiO_3$, which remains metallic at all temperatures, in $YNiO_3$ where the antiferromagnetic phase could be studied in the absence of magnetic rare-earths, and in $SmNiO_3$ and $PrNiO_3$ where the MIT could be studied in the two cases of $T_{MI} > T_N$ and $T_{MI} = T_N$.

Paramagnetic Fermi liquid behaviour was found in $LaNiO_3$ at all temperatures, disproving recent claims of antiferromagnetic order in bulk $LaNiO_3$ [49]. A substantial gap in the magnetic excitation spectrum of the antiferromagnetic phase was found in $YNiO_3$. In $SmNiO_3$, I have found that the NMR behaviour of the metallic phase is dominated by partially localised spins in e_g-σ^* system, in stark contrast to the Fermi liquid behaviour of $LaNiO_3$. The behaviour of the metallic state of $PrNiO_3$ is intermediate between those of $SmNiO_3$ and $LaNiO_3$, as it shows neither pure Fermi liquid nor pure localised paramagnetic behaviour. I have shown that the MIT in RENiO$_3$ is *not* driven by magnetic fluctuations at the examples of $SmNiO_3$ and $PrNiO_3$. Instead, the insulating phase is prerequisite to the magnetic fluctuations in $SmNiO_3$.

This chapter has established that NMR as a local static and dynamic magnetic probe can provide unique insight into the physics of RENiO$_3$. The nature of the metallic state as a Fermi liquid in bulk $LaNiO_3$ and a non-Fermi liquid the other RENiO$_3$, which has already been concluded from transport measurements [150], has been confirmed spectroscopically by NMR. Magnetic excitations in the antiferromagnetic phase of bulk RENiO$_3$ with small RE^{3+} ions have been studied here for the first time, by NMR. NMR has also allowed for the study of magnetic fluctuations in paramagnetic phases and across the MIT, providing new insight into the relationship between the MIT and the magnetism of RENiO$_3$.

Future ^{17}O-NMR measurements at very high temperatures may provide further insight into the metallic state of RENiO$_3$. Transport, infrared, and muon spin relaxation measurements in $YNiO_3$ have shown 'normal' metallic behaviour only above $\sim 720\,\mathrm{K}$, which is far above $T_{MI} = 582\,\mathrm{K}$ [38]. If there is indeed a crossover within the metallic phase at very high temperatures, NMR measurements in RENiO$_3$ with small ($YNiO_3$), medium ($SmNiO_3$), and large ($PrNiO_3$) rare-earths should be able to provide further insight. My NMR measurements have revealed large anomalies in the relaxation rate in $SmNiO_3$ towards very low temperature and in $PrNiO_3$ at 10 K with are likely caused by the lanthanide moments, which have not been understood based on NMR alone. Experiments using thermodynamic or further magnetic techniques may be able to elucidate the nature of these anomalies.

Chapter 6

A second magnetically ordered phase in $TlNiO_3$

The perovskite $TlNiO_3$ is a close relative of the rare-earth nickelates [65, 68, 67]. Since both ^{205}Tl and ^{203}Tl are spin 1/2 nuclei with high gyromagnetic ratio and high natural abundance, $TlNiO_3$ is in principle very well suited for NMR experiments. After we were provided a sample by José-Antonio Alonso, such experiments were first started as part of my Master's thesis project [71], and later continued by Marek Pikulski and myself. During this PhD project, using both NMR and μSR measurements, a new magnetic phase transition at $T_N{}^* = 202\,K$ was found, in addition to the known antiferromagnetic transition at $T_N = 104\,K$. The results from this chapter have been published in reference [72].

6.1 $TlNiO_3$ in the context of the rare-earth nickelates

The physical and chemical properties of the perovskite $TlNiO_3$ are similar to those of rare-earth nickelates $RENiO_3$ with small RE^{3+} ions. From a chemical perspective, the radius of Tl^{3+} is similar to that of small RE^{3+}, however thallium has a higher electronegativity than the rare-earths and therefore its bonding to oxygen is more covalent. This causes a slightly different A-site cation coordination: whereas in $RENiO_3$, there are eight short and four long $RE-O$ bonds per cation, in $TlNiO_3$ there are four short, four medium, and four long $Tl-O$ bonds [66, 65]. At room temperature, $TlNiO_3$ is a paramagnetic insulator with the same monoclinic crystal structure as the bond-disproportionated insulating phase of $RENiO_3$ [68]. It orders antiferromagnetically at $T_N = 104\,K$, which is significantly lower than the T_N of the rare-earth nickelates (130 to 221 K) [66]. The antiferromagnetic order in $TlNiO_3$ has the same unusual propagation vector as that in $RENiO_3$ [68]. Although the magnetic structure of $TlNiO_3$ has not been solved, it is likely

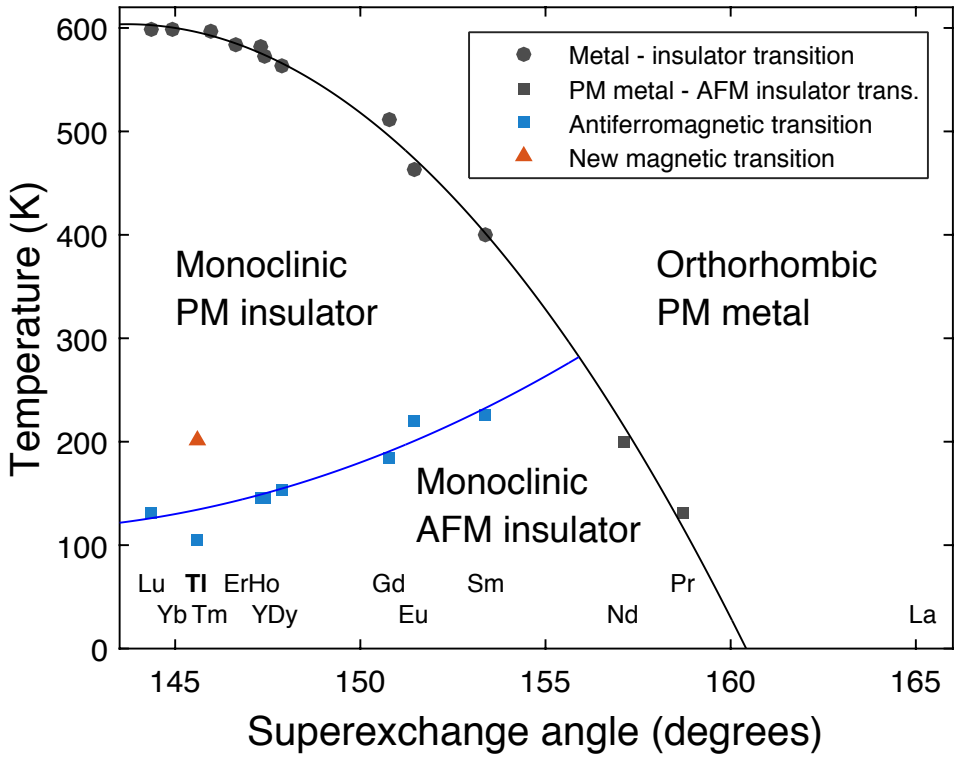

Figure 6.1: The two magnetic phase transitions in $TlNiO_3$ shown in the context of the phase diagram of $RENiO_3$, with the newly discovered transition in marked in red. Since Tl is significantly more electronegative than the rare-earth elements, the chemical bonding and thus the magnetic interactions in $TlNiO_3$ are slightly modified compared to the $RENiO_3$ series. Intuitively, this can explain a difference in T_N between $TlNiO_3$ and $RENiO_3$, but probably not the presence of a different magnetic phase transition.

the same structure as in $RENiO_3$. When the phase diagram of these nickelates is plotted as in figure 6.1 with the average Ni–O–Ni bond angle on the abscissa, the T_N of $TlNiO_3$ does not seem to follow the trend from the rare-earth nickelates. However, the T_N of $TlNiO_3$ and the $RENiO_3$ family seem to correlate better with the ratio of orthorhombic or monoclinic lattice parameters $c/(a\sqrt{2})$ [67].

In figure 6.2, the magnetic susceptibility of $TlNiO_3$ in different fields is plotted as a function of temperature. The known antiferromagnetic transition at $T_N = 104\,K$ is well visible in high applied fields. The low-temperature behaviour originates from the presence of unreacted $Ni(OH)_2$ from the synthesis [65] — $Ni(OH)_2$ is known to order magnetically at 25 K [117].

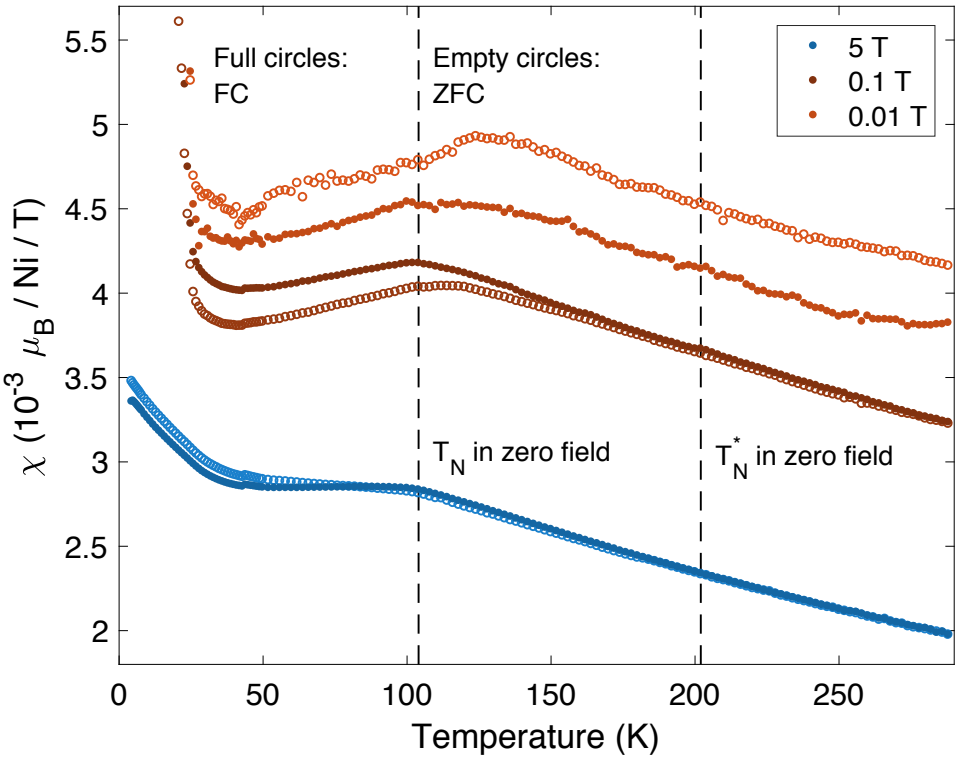

Figure 6.2: Magnetic susceptibility of $TlNiO_3$ in different magnetic fields, obtained using both field cooling (FC) and zero-field cooling (ZFC) protocols, measured by Toni Shiroka. All measurements were performed while warming, after cooling either with or without an applied field (full and empty circles). In high magnetic fields, the transition at $T_N = 104\,K$ is well visible. Unreacted $Ni(OH)_2$ from the synthesis procedure [65], which orders magnetically at 25 K [117], causes the large increase at low temperature.

6.2 ^{203}Tl- and ^{205}Tl-NMR spectra

Thallium is a unique element for NMR among the heavy metals because it has two spin-1/2 isotopes with high gyromagnetic ratio and natural abundance. The more common isotope ^{205}Tl has an abundance of 70.5 % and a magnetogyric ratio of $\gamma = 2\pi \cdot 24.5596\,\mathrm{MHz/T}$, while ^{203}Tl occurs at 29.5 % abundance and has $\gamma = 2\pi \cdot 24.3029\,\mathrm{MHz/T}$. The small difference between the two gyromagnetic ratio of ca. 1 % makes it easy to measure both isotopes with the same NMR probe circuit.

The NMR signal from both isotopes at room temperature in a field of 2 T is shown in figure 6.3 to the left. The spectra in the paramagnetic phase are relatively narrow featureless lines, at a frequency corresponding to an isotropic shift of 1.03 %.

In the antiferromagnetic phase, ^{205}Tl- and ^{203}Tl-NMR powder spectra are broadened drastically, such that the two isotopes can no longer be distinguished. Such combined NMR spectra of both isotopes will be called "Tl-NMR spectra". The Tl-NMR powder spectrum in a large applied field becomes so wide that it could not be covered completely with a single NMR probe circuit. The higher-frequency half of the spectrum is shown in the right half of figure 6.3. It has two relatively sharp edges, which are a hallmark of the presence of two Tl sites experiencing different internal fields $\vec{B}_{int}$. Their magnitude can be calculated from the frequency of the edge ν_{edge} [143]:

$$\nu_{\mathrm{edge}} = \frac{\gamma}{2\pi}(|B_0| + |B_{int}|). \tag{6.1}$$

The presence of two inequivalent positions of the A-site cation in antiferromagnetic nickelate perovskites is already known for Nd in $NdNiO_3$ [40].

6.2.1 Zero-field NMR spectra in the antiferromagnetic phase

The internal fields in the antiferromagnetic phase are so large that it is possible to perform NMR experiments in zero applied fields. Then, the zero-field NMR frequency is proportional to the (staggered) magnetisation, i.e. it is a measure of the antiferromagnetic order parameter.

The two NMR signals had to be measured using probe circuits optimised for different frequency ranges. In figure 6.4, the temperature dependence of the two NMR frequencies is shown, demonstrating that an internal magnetic field persists up to $\sim 200\,\mathrm{K}$. Thus, a new magnetic phase transition has been discovered. The inset shows example NMR spectra recorded at 5 K, which were both normalised individually because their amplitudes cannot be compared due to the use of different RF circuits.

For measurements in magnetic fields between 2 and 7 T, no trace of magnetic order could be found in the NMR spectrum between T_{N} and 200 K. Thus, this new transition occurs only in weak magnetic fields.

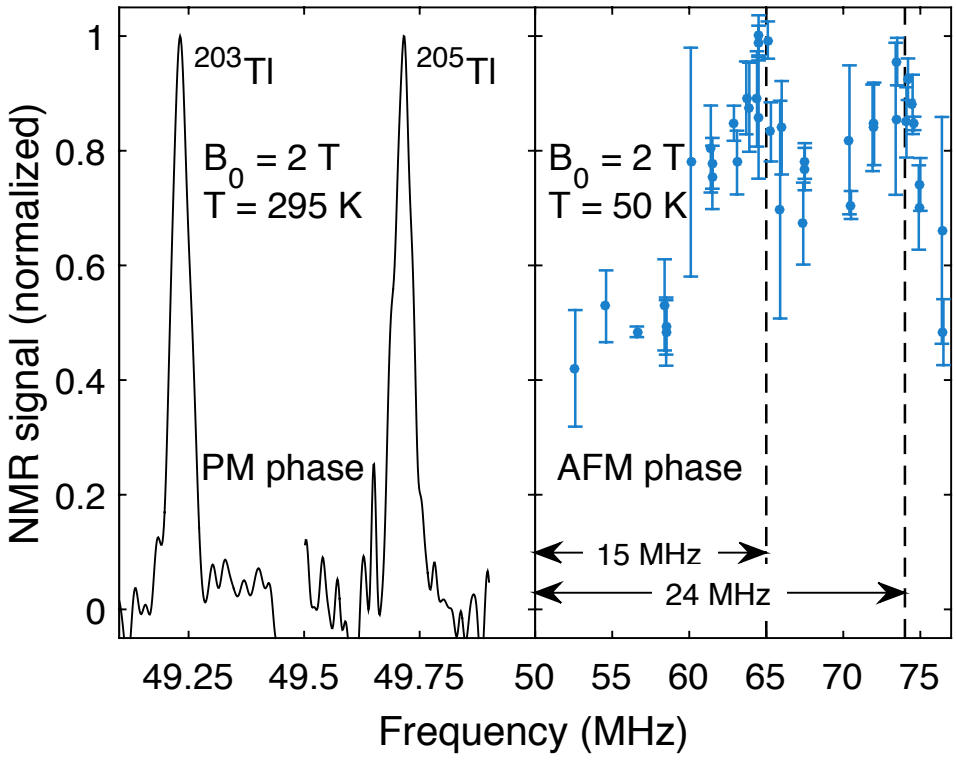

Figure 6.3: NMR spectra of both isotopes of Tl at room temperature, compared to the broad antiferromagnetic powder pattern at 50 K. Note the difference in horizontal scale between the two halves of this figure. In the antiferromagnetic phase, due to the substantial broadening of the spectrum, the two isotopes can no longer be distinguished. All three spectra (^{203}Tl at RT, ^{205}Tl at RT, AF spectrum) are normalised to the same height. At room temperature, the spectrum is consistent with a single Tl site occupied randomly by either isotope, while in the AF phase there are two sites experiencing different local fields due to the magnetic order.

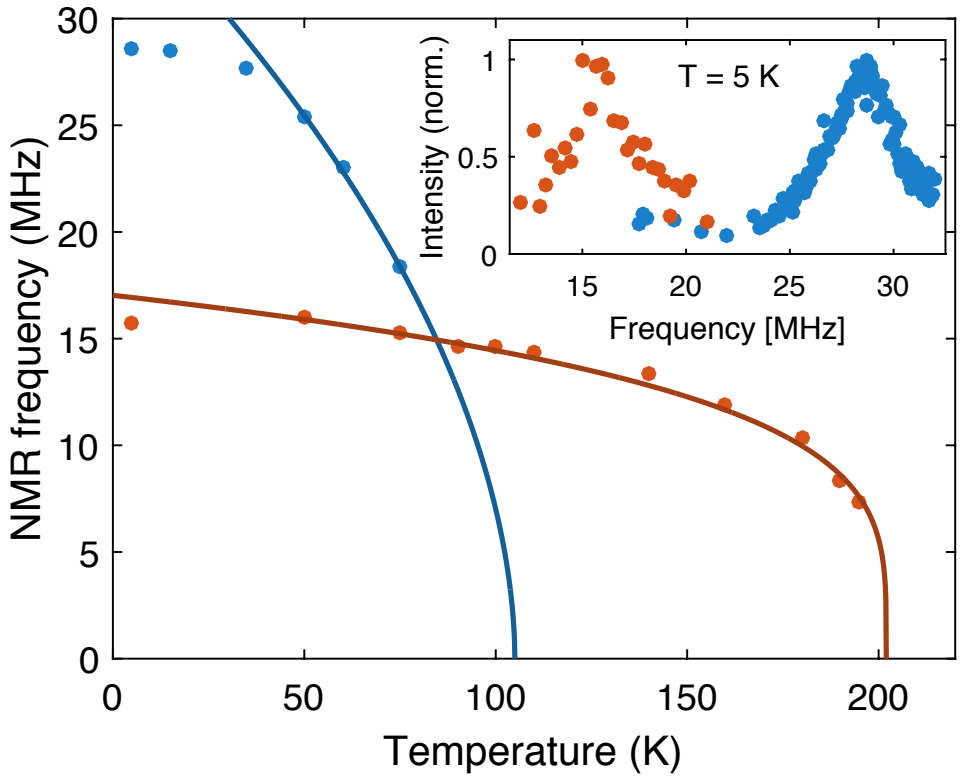

Figure 6.4: Zero-field Tl-NMR frequencies and example spectra (inset). The amplitudes of the two spectra in the inset are not comparable because the NMR probe circuit had to be optimised individually for the two signals. Solid lines are guides to the eye.

6.3 Tl-NMR relaxation

The relaxation rate due to magnetic fluctuations for different nuclei is proportional to γ^2 (see section 4.3.2). Thus, a difference of the order of 2 % is expected between the two isotopes, which is smaller than the typical error bar. Experimentally, the relaxation rates measured for both isotopes are identical, and will not be distinguished in this section.

Figure 6.5 shows the unusual temperature dependence of the transverse NMR relaxation rate T_2^{-1}, which was defined as the inverse time constant of the exponential decay of the spin-echo signal, measured in magnetic fields of several tesla. At high temperatures above 200 K, it is constant, whereas within the antiferromagnetic phase below 100 K, it follows an Arrhenius law (c.f. equation 5.26). Both are typical behaviour for a paramagnetic insulator and an antiferromagnetic phase with gapped excitation spectrum, respectively, and were already discussed for ^{17}O-NMR in $YNiO_3$ in section 5.5. The estimated magnetic excitation gap in $TlNiO_3$ is $\Delta/k_B \approx 80\,K$, which is smaller than that of $YNiO_3$ (345 K).

The anomalous part of the temperature-dependence is found at intermediate temperatures between 125 and 225 K. This corresponds approximately to the temperature range where the new phase was found in zero field. Here, T_2^{-1} strongly depends on the thermal history of the sample, as indicated by the colouring and the arrows in figure 6.5.[1]

It is unclear how to explain the hysteretic relaxation rate theoretically, however these data remain valuable. Since the spin-echo decay retains a single-exponential form at all temperatures, the value plotted in figure 6.5 represents the unique T_2^{-1} of *all* Tl nuclei in the entire sample. Thus, while the zero-field NMR spectra could have been interpreted as the presence of two spatially separated phases with different magnetic phase transition temperatures, this interpretation is inconsistent with the hysteretic relaxation data. Therefore, using NMR relaxation data, it could be established that the new phase transition affects the entire sample homogeneously.

6.4 Zero-field muon spin rotation

Seeing that the new magnetic phase exists only in zero or small applied magnetic field, further experiments in zero field are necessary to determine the transition temperature. As already discussed in section 2.2, for zero-field measurements near a magnetic phase transition, muon spin rotation (μSR) is a much more powerful technique than NMR because there is no loss of signal near the transition. Muon spin rotation measurements were performed on $TlNiO_3$ powder using the General Purpose Spectrometer (GPS) at the Swiss Muon Source (SμS) at the Paul Scherrer Institut.

[1] The history-dependence of T_2^{-1} was first noticed by Marek Pikulski.

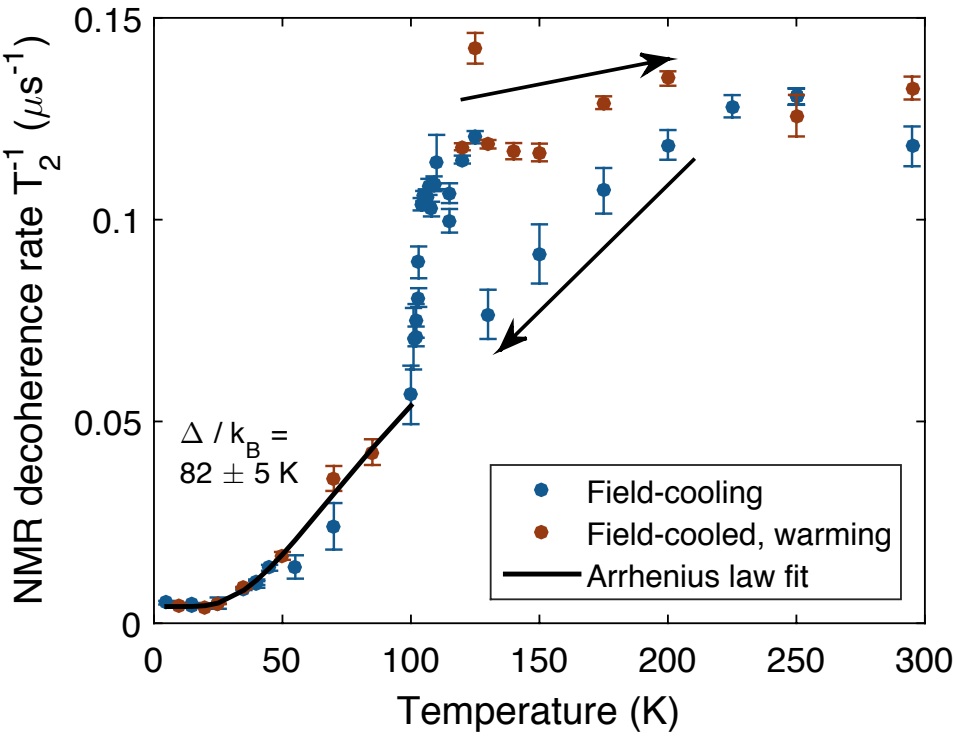

Figure 6.5: Transverse relaxation rate in Tl-NMR in $TlNiO_3$ as a function of temperature. A strong thermal history-dependence is found in the temperature range 125 to 225 K. In the antiferromagnetic phase, a clear activated behaviour is observed, indicating a gapped magnetic excitations. The data used to create this figure was acquired partially during my Master's thesis project [71] and partially by Marek Pikulski.

Muon data analysis

The histogram of the j'th positron detector is given by

$$S_j(t) = N_j \left(1 + \mathrm{Re}(A(t)\,\mathrm{e}^{i\varphi_j})\right) \mathrm{e}^{-\frac{t}{\tau_\mu}} + B_j, \tag{6.2}$$

where $A(t)$ is the μSR asymmetry signal, N_j are the normalised count rates, φ_j are the detector phases, B_j are the background count rates, and $\tau_\mu = 2.197\,\mu\mathrm{s}$ is the muon lifetime [146].

The phases φ_j are obtained from a calibration measurement in the paramagnetic phase at 250 K in a transverse applied field of 3 mT. The N_j and B_j are fitted for each dataset assuming $A(t)$ to be constant, which is appropriate except at very short times $t < 0.3\,\mu\mathrm{s}$. Then, the asymmetry $A(t)$ is fitted by the expressions detailed below, by means of a global maximum-likelihood estimation (MLE) using all detector histograms. For the MLE, the positron counts of each detector and each time bin are assumed to follow a Poisson distribution. The MLE was performed in Python (version 2.7.11) using the iminuit package [1], which uses the Minos algorithm [61] for estimating fit parameters and their error bars.

In the new phase above $T_\mathrm{N} = 104\,\mathrm{K}$, the asymmetry is fitted by the expression

$$A(t) = A\left(\frac{2}{3}\cos(2\pi\nu^{(1)}t)\mathrm{e}^{-\lambda_x^{(1)}t} + \frac{1}{3}\mathrm{e}^{-\lambda_z t}\right] + B\,\mathrm{e}^{-\lambda_\mathrm{DC}t} + C, \tag{6.3}$$

which assumes two muon stopping sites: one with a non-zero local magnetic field and one with zero local field, and exponential relaxation for both sites [30, 146].

Below T_N, four different μSR frequencies are found, and thus the fit function for the asymmetry was chosen as

$$A(t) = a^{(0)}\mathrm{e}^{-\lambda_z t} + \sum_{j=1}^{4} a^{(j)}\cos(2\pi\nu^{(j)}t)\mathrm{e}^{-\lambda_x^{(j)}t} + C. \tag{6.4}$$

At 100 K and at 5 and 15 K, only two and three frequencies could be identified, respectively.

Some example asymmetry data and their fit function are shown in figure 6.6. The presence of a single oscillation frequency above T_N and multiple frequencies below is well visible.

The oscillation frequencies $\nu^{(j)}$ are plotted as a function of temperature in figure 6.7. Both magnetic phase transitions are clearly visible, such that the temperature of the new magnetic phase transition can be identified as $T_\mathrm{N}{}^* = 202\,\mathrm{K}$. From this figure, it is clear why not all frequencies could be extracted from the data at 5, 15, and 100 K. The difference between some frequencies becomes as small as a few MHz. However, the μSR signal

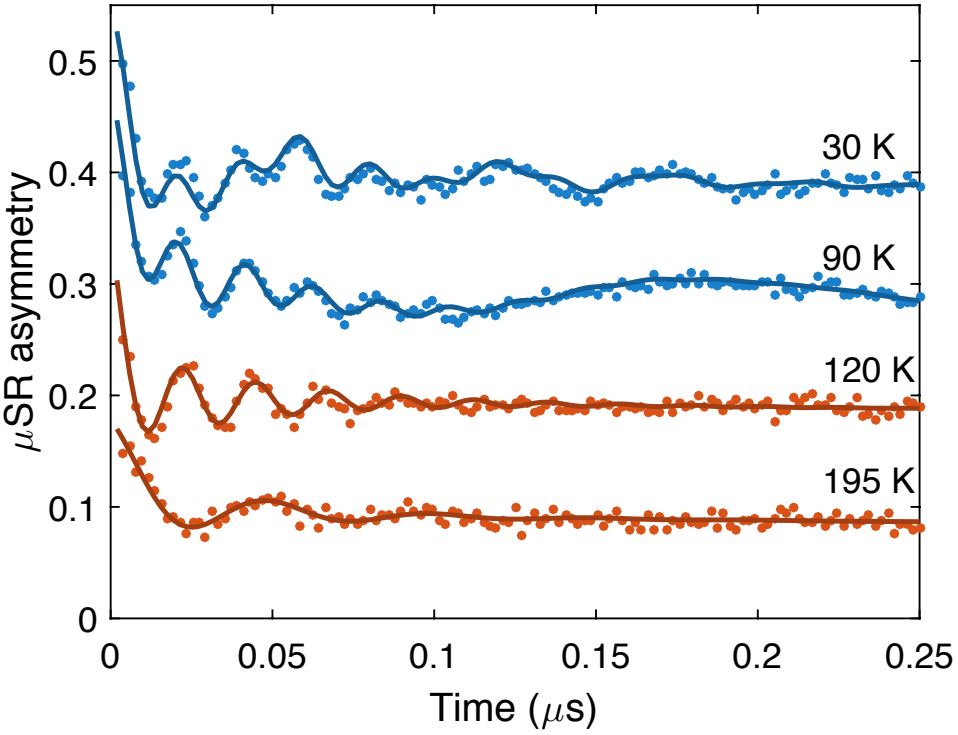

Figure 6.6: Some examples for zero-field μSR time-domain asymmetries in $TlNiO_3$ at different temperatures. Solid lines are fits to the data using equations 6.3 and 6.4 above and below $T_N = 104\,K$, respectively. Different datasets are offset vertically for clarity. Above T_N, only a single oscillation frequency is present, whereas multiple different frequencies appear at lower temperature.

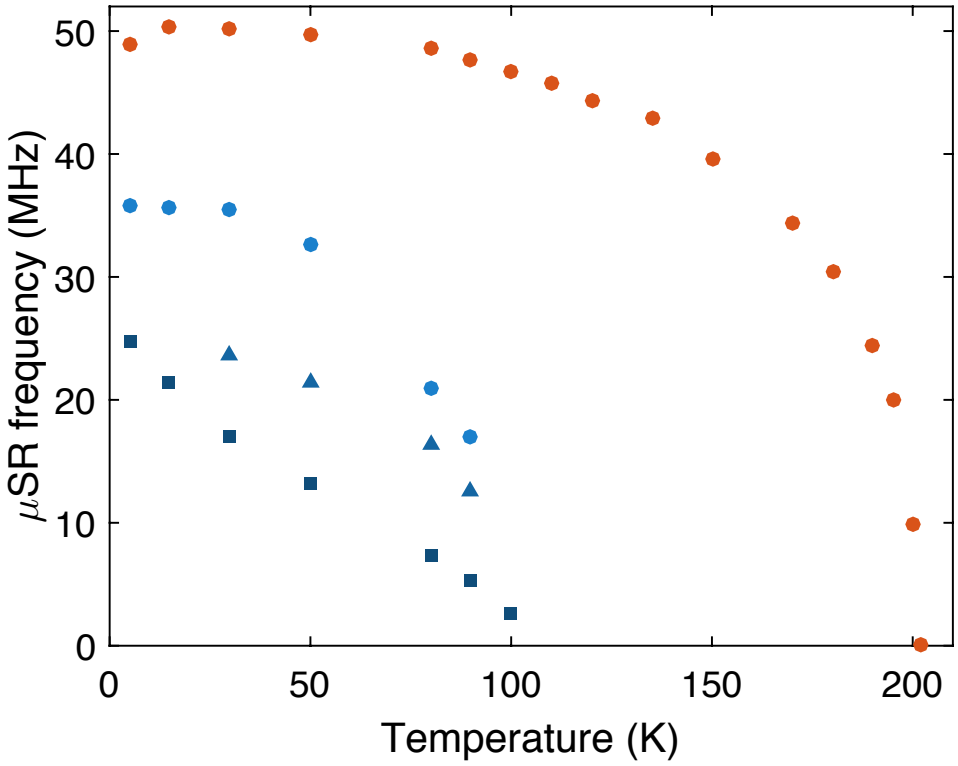

Figure 6.7: Temperature-dependence of the muon precession frequencies extracted from fits such as those shown in Figure 6.6. No error bars are shown because their size is similar to or smaller than that of the the markers. While the three frequencies shown in blue vanish at the previously known $T_N = 104\,K$, the red frequency reveals the second magnetic transition temperature 202 K.

dephases within ca. 0.2 µs (c.f. figure 6.6), and thus it becomes impossible to resolve such small frequency differences.

The presence of many different μSR frequencies could probably be explained by the presence of several inequivalent muon sites. In transition metal oxides, the muon typically bonds with an oxygen atom [52]. The fact that apparently, different muon sites are affected by only one of the two magnetic phase transitions appears odd if both transitions occur homogeneously throughout the sample, as claimed from the NMR data. However, in $Nd_{0.7}La_{0.3}NiO_3$ it was found that only half of the muons were affected by the magnetic order below T_N [37], which may be consistent with our findings for $TlNiO_3$. The unusual, almost linear temperature dependence of the lowest frequency below T_N in figure 6.7 remains unexplained.

6.5 Conclusion and outlook

As a close relative of the rare-earth nickelates, $TlNiO_3$ is known to share many physical properties with the $RENiO_3$ family, including an antiferromagnetic phase transition with $T_N = 104\,K$. Using ^{205}Tl- and ^{203}Tl-NMR as well as μSR measurements, a second magnetic phase transition has been discovered at $T_N^* = 202\,K$ in zero applied field. This new phase transition is suppressed by a magnetic field of a few tesla, however its vestige remains visible in the hysteresis of the transverse NMR relaxation rate T_2^{-1}.

I have attempted to perform NMR above room temperature up to 500 K in order to search for the metal–insulator transition. However, heating the sample has resulted in a change of its physical properties, perhaps due to the loss of oxygen. Thermogravimetric measurements have shown weight loss starting at temperatures as low as 270 °C ≈ 460 K, even in an oxygen atmosphere [65]. In subsequent measurements of the magnetic susceptibility by Toni Shiroka, a magnetic transition at T_N^* is very well visible, while the feature at T_N is no longer seen. Thus, it seems that the unintentional thermal treatment of the sample has affected or enhanced the new phase transition. Unfortunately, only a small amount $TlNiO_3$ powder has been available to me, and therefore all of it had to be used for the high-temperature experiments in order to achieve a decent NMR signal. Thus, no further experiments were performed in this project due to the suspected sample degradation.

It remains unclear how the NMR and μSR results can be reconciled with the observations on the "degraded" sample. Since all $RENiO_3$ samples are slightly oxygen-deficient [139], our "$TlNiO_3$" sample was originally most likely a homogeneous powder with stoichiometry $TlNiO_{3-x}$. In the case of $LaNiO_3$, there are two known phases with fully ordered oxygen-vacancy structure, $LaNiO_{2.5}$ and $LaNiO_{2.75}$, which both have a magnetic phase transition [139]. If the analogous thallium compounds exist, then perhaps T_N^* corresponds to one of their magnetic transitions. However, within this in-

terpretation, it is not clear why both transitions at T_N and $T_N{}^*$ seems to occur *homogeneously* across the entire sample in NMR.

Chapter 7

A ^{175}Lu-NQR signal in $LuNiO_3$

7.1 Advantages of ^{175}Lu-NQR

The ^{175}Lu nucleus has one of the highest electric quadrupole moments found in the periodic table, and the Lu^{3+} ion is diamagnetic. This combination makes $LuNiO_3$ a unique material for the study of $RENiO_3$ by nuclear spin spectroscopy. For paramagnetic rare-earths, the strong on-site hyperfine coupling of $4f$ electrons causes very rapid relaxation of the nuclear spins, often making their observation impossible. Magnetic resonance experiments on rare-earth nuclei are therefore restricted to using compounds with diamagnetic rare-earths, i.e. $LaNiO_3$, $YNiO_3$, or $LuNiO_3$.

For the case of $LaNiO_3$, some ^{139}La-NMR data is reported in section 5.4 — some poor quality data has already been reported in the literature [124]. There, the ^{139}La-NMR data are consistent with the ^{17}O-NMR. However, $LaNiO_3$ is the simplest of the $RENiO_3$ materials, showing Fermi liquid behaviour across the entire temperature range under study.

In contrast, $YNiO_3$ and $LuNiO_3$ are both in the bond-disproportionated insulating phase at room temperature. The two relevant rare-earth nuclei, ^{89}Y and ^{175}Lu, have completely different physical properties.

On one hand, ^{89}Y is a spin-1/2 nucleus with low gyromagnetic ratio (c.f. Table 2.1), and would allow one to probe the magnetic fluctuations at the rare-earth site rather than the oxygen site. Due to the low gyromagnetic ratio, the signal-to-noise ratio in ^{89}Y-NMR should be low. One can therefore expect ^{89}Y-NMR on $YNiO_3$ to be experimentally challenging and unlikely to yield any new information compared to ^{17}O-NMR.

On the other hand, ^{175}Lu is a spin-7/2 nucleus with an extremely large quadrupole moment (c.f. Table 2.1). This means that ^{175}Lu-NQR experiments in zero applied field are feasible. The NQR frequencies could be more sensitive to charge redistribution due to either charge- or bond-

disproportionation than the ^{17}O-NMR powder spectrum for two reasons. First, the nuclear quadrupole moment of ^{175}Lu is more than two orders of magnitude larger than that of ^{17}O. Second, in zero field, there is no anisotropic magnetic shift that can interfere with the extraction of the EFG.

7.2 Seeking the NQR signal

7.2.1 Preliminary considerations and previous attempts

While an NMR signal can be reasonably expected to be found near zero shift in most experimentally relevant cases, there is no strong restriction on NQR frequencies. Experimental ^{175}Lu-NQR frequencies in different inorganic compounds cover a huge range from 37 to 470 MHz [127]. Restricting to the lowest resonance frequency of each material still gives a very wide frequency band from 37 to 159 MHz. Finding a potentially less than 100 kHz broad signal in such a wide search space would require an unreasonably large experimental effort. Therefore, either the spectrum must be broadened by applying a static field to a powder sample, or the resonance frequencies in $LuNiO_3$ must be estimated from electronic structure calculations.

The former approach was first attempted during the semester thesis project of Dominik Schildknecht in our lab [126]. However, due to the high applied fields (5.5 and 7 T), the spectra became so broad that poor signal-to-noise ratio became a problem. The interpretation of the spectra was further complicated by the fact that the Zeeman and quadrupolar splitting were of the same order of magnitude, thus they could not be compared to any perturbative calculation. Most of these measurements were performed in the antiferromagnetic phase, where in addition to the applied field and the EFG, there is an internal magnetic field, which makes the interpretation of powder spectra even more difficult. Finally, the experiment was plagued by technical difficulties such as RF crosstalk and significant sample heating by the RF pulses. Unfortunately, all of these problems meant that the recorded signals were not useful by themselves in the quest for the ^{175}Lu-NQR frequencies of $LuNiO_3$.

The T_1 relaxation rate will originate from magnetic fluctuations, which were shown in section 5.3 to vary continuously across the $RENiO_3$ series. Unlike the NQR frequency, the T_1 should therefore be predictable from the T_1 of the A-site nuclei in other compounds. In chapter 6, the T_1 relaxation time of ^{205}Tl in $TlNiO_3$ at room temperature is reported to be $44.9 \pm 2.6\,\mu s$. For two different nuclei experiencing identical magnetic fluctuations, T_1^{-1} scales as the square of the magnetogyric ratio. Therefore, we expect the relaxation time of ^{175}Lu in $LuNiO_3$ to be slower by a factor of $\gamma(^{205}\mathrm{Tl})^2/\gamma(^{175}\mathrm{Lu})^2 = 25.5$, corresponding to $T_1 \approx 1.1$ ms. However, since Tl is more electronegative than the rare-earths, the chemical and physical properties of their compounds are not identical, and hence their magnetic

fluctuations will differ somewhat. Thus, the above prediction of T_1 must be regarded as an order-of-magnitude estimate.

7.2.2 Theoretical calculations

Oleg Peil has used three different density-functional-theory methods to compute the EFG tensor at the Lu-site in $LuNiO_3$. The first two calculations were performed using the Vienna ab-initio simulation package (VASP) [76] using the Perdew–Burke–Ernzerhof exchange-correlation functional [108, 109], with an added on-site electron–electron repulsion U [14], treating the full $4f$ shell either as core or valence electrons. The third calculation used the all-electron simulation software package WIEN2k [18]. The latter two methods are expected to yield more accurate results due to their full treatment of $4f$ electrons. All three methods gave agreeing values for the EFG asymmetry parameter $\eta_Q = 0.31$, but three different values for C_Q, -1101, -1445, and $-1481\,\mathrm{MHz}$ [106]. After plugging η_Q and the three different C_Q's into the NQR Hamiltonian (Eq. 2.49) and diagonalising it, the three "single-quantum" transition frequencies are predicted to be 102.1, 150.8, and 233.6 MHz, 134.0, 197.9, and 306.6 MHz, or 137.4, 202.8, and 314.3 MHz, respectively.

7.2.3 Experimental hunt

Since our RF pulse amplifiers work only up to ca. 180 MHz, I searched for the lowest NQR frequency. First, the RF pulse amplitude at 150 MHz was calibrated using the ^{1}H-NMR signal in tap water in 3.5 T. Second, in order to reduce the number of required sampling frequencies to find a signal with unknown linewidth, I applied a moderate magnetic field in order to broaden the powder spectrum. This field must not be too large, as otherwise the spectral density and thus the signal amplitude becomes too low to be detectable. I used a field of $B_0 \approx 0.5\,\mathrm{T}$, which corresponds to $\omega_0 \approx -2\pi \cdot 2.4\,\mathrm{MHz}$, in order to spread the signal over a few MHz. The resulting spin echo amplitude sampled at different frequencies is plotted in Figure 7.1. A weak signal is visible in the range of 117 to 132 MHz.

During this scan, measurements near 125 MHz were impossible because of strong RF crosstalk at that frequency. However, it was clear that NQR measurements near 125 MHz are necessary, and therefore the crosstalk must be eliminated. I have discovered that the source of the strong crosstalk is the data acquisition board which we use to digitise the demodulated NMR or NQR signal. The board emits radio waves at odd harmonics of the sampling rate, which can be received by the spectrometer. In our usual mode of operation, data are acquired at a rate of 25 MS/s, and therefore the fifth harmonic causes interference at 125 MHz. Changing the sampling rate to 20 MS/s solved the problem and allowed the discovery of the NQR signal.

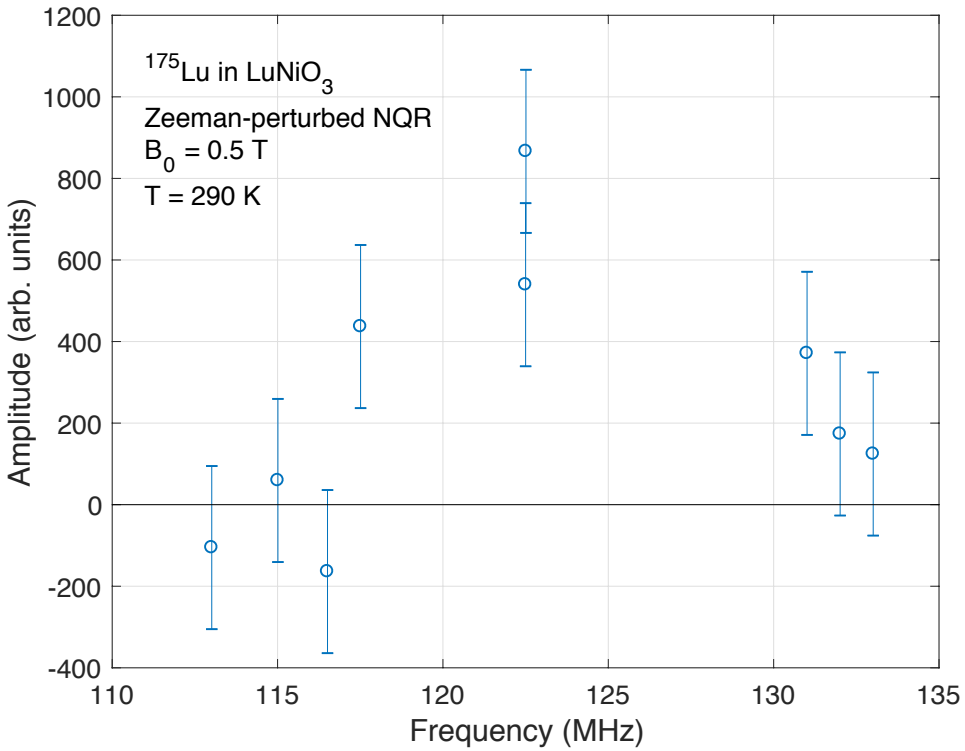

Figure 7.1: Spin echo amplitudes of ^{175}Lu in $LuNiO_3$ powder in a field of approx. 0.5 T at a few different radio frequencies. Error bars are estimated from signal-to-noise ratio. Between ca. 117 and 132 MHz, a weak signal is visible.

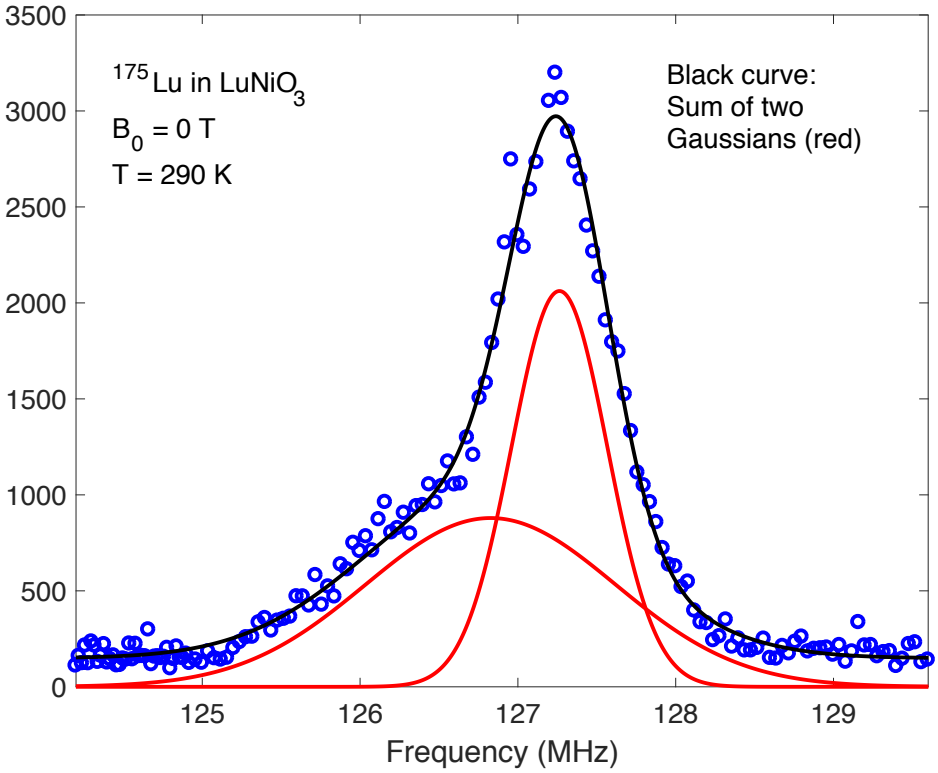

Figure 7.2: ^{175}Lu-NQR spectrum obtained from $LuNiO_3$ at 290 K in zero field, by integrating the absolute value of the Fourier transform of the spin echo signal for each carrier frequency. The spectrum can be fitted very well with a superposition of two Gaussians, which have equal area within the error bar. This suggests the presence of two inequivalent Lu-sites in $LuNiO_3$. Unfortunately, the poor sample quality does not allow to draw any meaningful conclusions without a comparison to a different sample of $LuNiO_3$.

7.3 The NQR spectrum

After having found restrictions on the zero-field resonance frequency from both theoretical and experimental methods, I scanned the frequency range from 123 to 130 MHz and found the NQR signal shown in figure 7.2. Surprisingly, the signal could be fitted as a superposition of two Gaussians. The narrower peak is centred at $127\,263 \pm 11$ kHz and has a full width at half maximum (FWHM) of 715 ± 35 kHz. The wider peak is centred at $126\,827 \pm 63$ kHz and has a FWHM of 1863 ± 111 kHz. The area of the two peaks is equal to within the error bar of the fit.

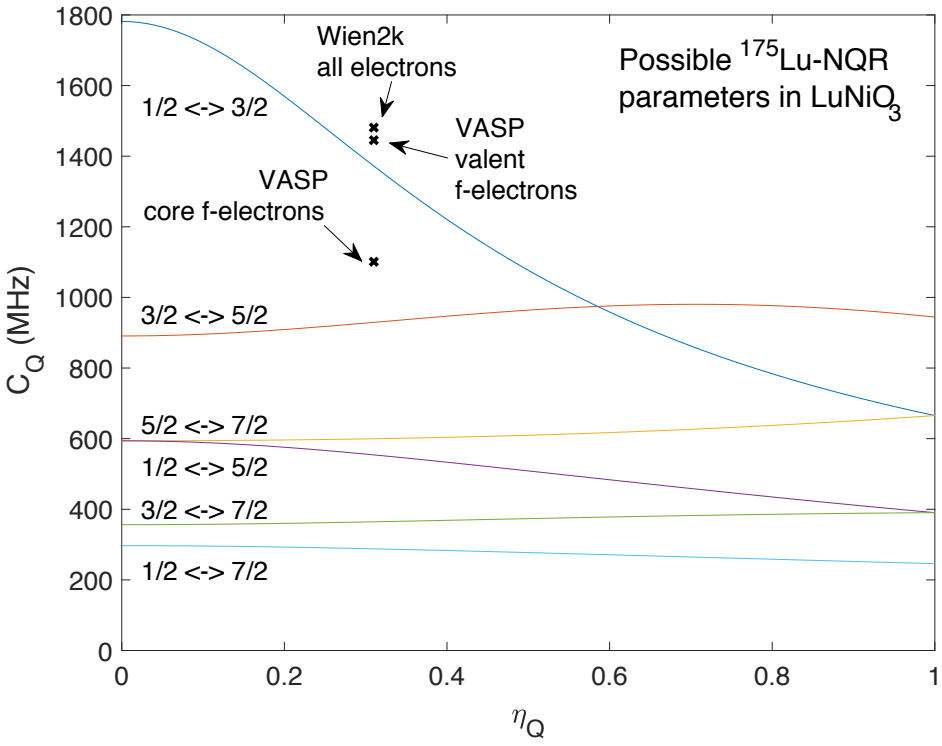

Figure 7.3: Only one NQR frequency was found, and it is not known which transition it belongs to. Therefore, the experimentally allowed values of C_Q and η_Q fall on a set of curves, which are plotted here. Crosses: theoretical predictions by Oleg Peil obtained using different DFT methods.

7.3.1 Possible values of NQR parameters

As the NQR Hamiltonian 2.49 has two parameters, C_Q and η_Q, it cannot be fully determined by observing a single resonance frequency in zero magnetic field. Due to the very different linewidths of the two signals, it is highly unlikely that both originate from two different transitions in equivalent nuclei. Since it is a priori unknown which transition has been observed, the set of possible values of C_Q and η_Q fall on lines, corresponding to the different transitions. If $\eta_Q \neq 0$, not only the 'single-quantum' transitions but all overtone transitions are allowed in NQR. Therefore, for a spin 7/2 nucleus, the set of candidate values for C_Q and η_Q fall on six lines, as shown in Fig. 7.3. Comparison with the theoretical predictions discussed in section 7.2.2 shows that the experimental signal likely corresponds to the $1/2 \leftrightarrow 3/2$ transition. Assuming that the theoretical prediction that $\eta_Q = 0.31$ is correct then implies $C_Q = 1372\,\mathrm{MHz}$. In this case, the other two "single-quantum" transitions should lie at 187.9 and 291.1 MHz, which cannot be accessed with our RF power amplifiers.

7.3.2 Interpretation of the spectrum

There are four possible interpretations for two peaks with equal areas.

First, both signals could come from the different transitions in the same nuclei. This is possible if the value η_Q is such that two different transitions have the same frequency. One can read off all possible values of η_Q from the crossing points of any two lines in Figure 7.3. Numerical simulations using QUEST [111] show that the only crossing point at which both signals have similar intensities is that of the $1/2 \leftrightarrow 3/2$ and $3/2 \leftrightarrow 5/2$ transitions at $\eta_Q \approx 0.585$. However, it is hard to explain the very different widths of the two peaks with this model. This possibility can be eliminated if a second NQR signal is found, which will fix the values of C_Q and η_Q.

Second, given the poor sample quality, it is possible that one signal comes from $LuNiO_3$ whereas the other signal comes from some impurity phase. However, since the NQR frequency is highly sensitive to the chemical environment, having two frequencies so close together would be an unlikely coincidence. This model can be ruled out by studying a higher-quality sample, and by measuring the temperature-dependences of the resonance frequency and relaxation rate, especially near the magnetic phase transition of $LuNiO_3$.

Third, both signals could come from impurity phases. This would be an unfortunate coincidence, and could also be ruled out by studying a higher-quality sample.

Finally, both signals could come from pristine $LuNiO_3$, from nuclei in very slightly different environments. This would imply the existence of two inequivalent Lu-positions in the BDI phase of $LuNiO_3$. Since both peaks have equal areas, the two inequivalent species should occur in a ratio of $1:1$. All previous crystallographic studies of any paramagnetic insulating $RENiO_3$ have found only one inequivalent rare-earth position. In the antiferromagnetic phase, however, two (pairs of) inequivalent rare-earths in a $1:1$ ratio are known to occur: the $B^{\pm}$ and B^0 sites in reference [40].

If these two sites are inequivalent already in the BDI phase of the rare-earth nickelates, this would change the physical picture of their phase diagram significantly. The $B^{\pm}$ and B^0 sites are related by the screw axis and the inversion symmetry of the $P2_1/n$ structure. Breaking these two symmetries gives the monoclinic space group Pc, which allows for ferroelectricity. As the spectrum was obtained from a low-quality sample, unfortunately, I will abstain from further speculation.

7.4 NQR relaxation at room temperature

7.4.1 Theoretical inversion recovery curve

In NQR, the functional form of the inversion recovery curve depends on the relaxation mechanism, which transition is observed, and the value of η_Q. Since both ^{17}O-NMR and Tl-NMR in other perovskite nickelates showed rapid relaxation via isotropic hyperfine fields (see previous chapters), it is reasonable to assume that the same mechanism drives the relaxation of ^{175}Lu in $LuNiO_3$. In section 7.3.1, it was argued that most likely the $1/2 \leftrightarrow 3/2$ transition is observed. Finally, as discussed in section 7.2.2, DFT simulations showed that likely $\eta_Q \approx 0.31$.

Under these assumptions, we can use the theoretical results of section 4.9 in order to derive the form of the inversion recovery curve. First, diagonalise the NQR Hamiltonian for spin 7/2 and $\eta_Q = 0.31$ numerically. Then, calculate the relaxation matrix numerically using equation 4.124 and diagonalise it. The master equation 4.55 is then solved by a sum of exponential functions whose decay rates are the eigenvalues of the Redfield matrix and whose weights are determined by the projections of the initial state onto the eigenvectors. In our particular case, this procedure yields the expression

$$\begin{aligned} f(t) =& 0.0389 \exp(-3\frac{t}{T_1}) + 0.3880 \exp(-9.1739\frac{t}{T_1}) \\ &+ 0.5731 \exp(-18.0841\frac{t}{T_1}), \end{aligned} \tag{7.1}$$

which is used to fit the experimental signal $S(t)$ as

$$S(t) = a - bf(t), \tag{7.2}$$

with the two auxiliary fit parameters a and b.

7.4.2 Experimental data

The experimental data shown in Figure 7.4 show poor inversion, most likely due to poor pulse width calibration. To good approximation, this does not affect the shape of the recovery curve though, because any off-diagonal density matrix elements created by the inversion pulse decay more rapidly than the diagonal elements. Then, due to the linearity of the master equation, the shape of the recovery curve remains the same if a transition is only partially inverted.

Fitting the experimental longitudinal relaxation data with the expression obtained in the previous section gives $T_1 = 2.5 \pm 0.6\,\text{ms}$. This value is to be compared with the estimate of 1.1 ms obtained in section 7.2.1 by rescaling the T_1 of ^{205}Tl in $TlNiO_3$ by the square of the gyromagnetic ratio. The fact that the experimental relaxation rate of ^{175}Lu in $LuNiO_3$ is slower might

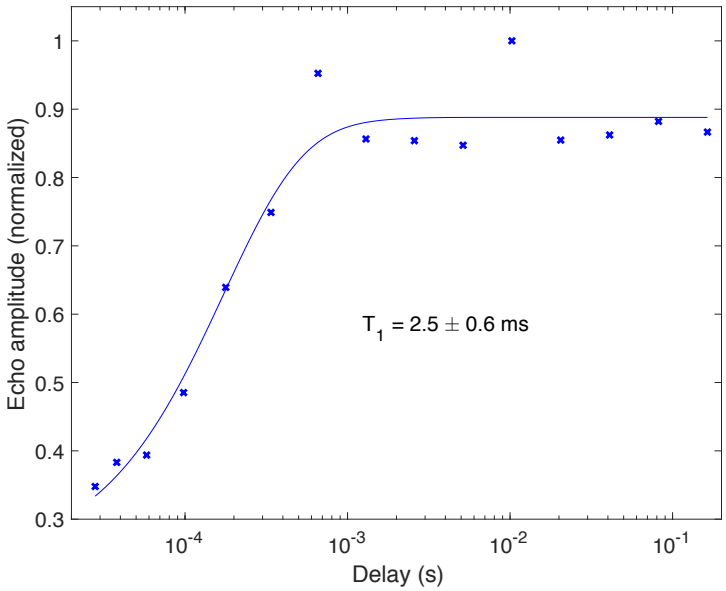

Figure 7.4: Experimental inversion recovery for ^{175}Lu-NQR in $LuNiO_3$ in zero applied field, measured at 127.25 MHz. The fit function assumes isotropic magnetic relaxation, $\eta_Q = 0.31$, and that I observed the $1/2 \leftrightarrow 3/2$ transition. Poor inversion due to inaccurate pulse lengths does not affect the functional form of the inversion recovery curve to good approximation, therefore the fit remains valid.

be explained by the fact that the rare-earths have a lower electronegativity than Tl, and therefore the Lu−O bond is less covalent than the Tl−O bond. The different distortions of the TlO_{12} and REO_{12} coordination polyhedra in $TlNiO_3$ and the $RENiO_3$ family (which is caused by the already mentioned difference in electronegativity) [65] may also affect the nuclear spin relaxation.

7.5 Conclusion and outlook

After considerable experimental and theoretical effort, a good candidate ^{175}Lu-NQR signal in $LuNiO_3$ has been found at room temperature. The candidate signal is a superposition of two peaks, which suggests the existence of two inequivalent rare-earth sites in the paramagnetic insulating phase of $LuNiO_3$. This would have considerable implications on our understanding of the phase diagram of the rare-earth nickelates, as the symmetry-breaking pattern at the phase transitions changes. Consequently, the paramagnetic insulating phase would likely be ferroelectric.

As only one peak was found in the ^{205}Tl- and ^{203}Tl-NMR spectra in $TlNiO_3$, this effect may be poorly visible in the magnetic shift, or it may be

absent in $TlNiO_3$, or the second site relaxes too rapidly to be observed by NMR. A comparison with ^{89}Y-NMR in $YNiO_3$ at room temperature would be useful for two reasons. First, this material is a more typical representative of the $RENiO_3$ series than $TlNiO_3$, and second, the relaxation of ^{89}Y will be much slower than that of ^{205}Tl or ^{203}Tl due to its small gyromagnetic ratio.

The most direct test of the hypothesis of two inequivalent rare-earth sites will be a ^{175}Lu-NQR experiment on a $LuNiO_3$ sample of higher quality. If there are still two peaks with equal area, temperature-dependent NQR experiments would be the natural next step. Detailed relaxation measurements from room temperature down to the Néel temperature may reveal a difference in behaviour of the two sites, which could allow the assignment of the slowly relaxing B^0 and rapidly relaxing $B^{\pm}$ sites (in the notation of reference [40]). High-temperature measurements around the metal-insulator transition at 600 K would reveal whether the splitting originates at this phase transition, or whether it is already present in the metallic phase. Thus, when higher-quality samples of $LuNiO_3$ become available, ^{175}Lu-NQR spectroscopy experiments will either rule out the hypothesis put forward in this chapter or provide completely new insights into the physics of the rare-earth nickelates.

Acknowledgements

First of all, I want to thank my advisor, Prof. Dr. Joël Mesot, not only for allowing me to work on such a fascinating topic but also for our many wonderful interactions over the years. Despite his other obligations, at first as Director of the Paul Scherrer Institute and later as President of ETH Zürich, he has always remained closely involved in my research and was always available whenever I needed his help or advice. I have always enjoyed our discussions about the nickelates, physics in general, and other topics. It has been a great pleasure to work with you.

I have been incredibly fortunate to work with one of the most experienced scientists in the world of solid state physics and strongly correlated electrons. I would like to thank the brilliant Prof. em. Dr. Hans-Rudolf Ott for his wise advice and inspiring supervision. He and Prof. Mesot gave me the freedom to seek my own scientific questions, while providing guidance whenever it was needed.

I want to thank Dr. Toni Shiroka for his dedication to proper science and to our laboratory. He taught me every step in performing a successful μSR experiment, from mounting the sample to analysing and interpreting the data. His measurements of the magnetic susceptibility of nickelate samples were necessary for estimating their quality, which has historically been an issue in these materials, before starting a time-consuming NMR experiment.

I want to thank my fellow PhD students in our laboratory, Dr. Marek Pikulski and Dr. Nicolò Barbero. Marek supervised me during my Master's project, and taught me how to perform an NMR experiment during this time. Our first work on $TlNiO_3$ is the seed of inspiration from which my PhD project has grown. His sharp scientific mind and great technical skills were crucial to the early stages of the rare-earth nickelates project. His preliminary ^{17}O-NMR measurement in $PrNiO_3$ provided the proof-of-principle for the experiments which have occupied me for a few years. Working with Marek and Nicolò in the lab has always been enjoyable and productive, and together with Toni and the advice of Prof. Ott we were able to solve (almost) any technical problem. Our scientific and technical discussions in the lab, and our conversations about life in the lab and the hypothetical existence of a life outside the lab at our 'group beers' have been fantastic.

I was lucky to work closely with Dr. Marisa Medarde, who may be great-

est expert on the rare-earth nickelates in the world. Our frequent discussions, especially in the early stages of my PhD project, were crucial to identifying the questions which I could address by NMR. I want to thank Marisa, not only for our inspiring discussions on the nickelates, but also for our great collaborations at various synchrotron beamtimes.

Of course, there are many other people without whom this project would not have been possible. The ground-breaking work in the preparation of high-quality $RE\mathrm{NiO_3}$ materials by Dr. Dariusz Gawryluk was required for the success of my NMR experiments on compounds with small rare-earths such as $\mathrm{ErNiO_3}$. I want to thank Dariusz for his preparation and isotopic enrichment of most ^{17}O-NMR samples. I would like to thank Prof. José-Antonio Alonso for providing the $\mathrm{TlNiO_3}$, $\mathrm{PrNiO_3}$, and $\mathrm{SmNiO_3}$ samples for my project, and Prof. Kazimierz Conder for the isotopic enrichment of the $\mathrm{PrNiO_3}$ and $\mathrm{SmNiO_3}$ samples with ^{17}O for my NMR experiments. I want to thank Dr. Oleg Peil for his theoretical support over many years, especially his calculations of electric field gradients in $RE\mathrm{NiO_3}$. His calculations helped to understand to ^{17}O-NMR signals and were invaluable in finding the ^{175}Lu-NQR signal in $\mathrm{LuNiO_3}$. I would like to thank Dr. Mladen Horvatić for our discussion of obscure issues in NMR relaxation.

I want to thank Dr. Laura Piveteau for our collaboration on NQR in inorganic lead halide perovskites. It was a great experience to see the differences and similarities between how chemists and physicists think about solid-state magnetic resonance.

I want to thank Dr. Daniel Mazzone, Dr. Ayman Said, Dr. Stephan Rosenkranz, and Dr. Marisa Medarde for teaching me how to use the powerful technique of inelastic X-ray scattering of single-crystalline materials. Our beamtime at Argonne National Laboratory was one of the most educational weeks of my PhD.

I thank our group secretaries, Gaby Strahm and Claudia Vinzens, for handling all the administrative issues related to my work.

I would like to thank Profs. Werner Wegscheider and Andrey Zheludev for kindly allowing me to use a desk in their group offices during times of office space shortage. I want to thank all PhD students and postdocs of the groups of Profs. Andrey Zheludev and Leonardo Degiorgi for our countless solid-state physics lunches and coffee breaks, and all of our conversations about any topic within and outside the realm of physics.

Last, but most certainly not least, I thank all of my family and friends for supporting me over these last years.

Bibliography

[1] iminuit – MINUIT from Python (version 1.2). `http://github.com/iminuit/iminuit`.

[2] A. Abragam. *The Principles of Nuclear Magnetism*. Clarendon Press, 1961.

[3] A. Abragam and M. H. L. Pryce. Theory of the nuclear hyperfine structure of paramagnetic resonance spectra in crystals. *Proc. Royal Soc. Lond. A*, 205(1080):135–153, 1951.

[4] D. W. Alderman, M. S. Solum, and D. M. Grant. Methods for analyzing spectroscopic line shapes. NMR solid powder patterns. *J. Chem. Phys.*, 84(7):3717–3725, 1986.

[5] J. W. Allen and R. M. Martin. Kondo volume collapse and the $\gamma \rightarrow \alpha$ transition in cerium. *Phys. Rev. Lett.*, 49(15):1106–1110, 1982.

[6] H. Alloul, T. Ohno, and P. Mendels. ^{89}Y NMR evidence for a Fermi-liquid behavior in $YBa_2Cu_3O_{6+x}$. *Phys. Rev. Lett.*, 63(16):1700–1703, 1989.

[7] J. A. Alonso, M. J. Martínez-Lope, M. T. Casais, M. A. G. Aranda, and M. T. Fernández-Díaz. Metal–insulator transitions, structural and microstructural evolution of $RNiO_3$ (R = Sm, Eu, Gd, Dy, Ho, Y) perovskites: Evidence for room-temperature charge disproportionation in monoclinic $HoNiO_3$ and $YNiO_3$. *J. Am. Chem. Soc.*, 121(20):4754–4762, 1999.

[8] J. A. Alonso, M. J. Martínez-Lope, M. T. Casais, J. L. García-Muñoz, M. T. Fernández-Díaz, and M. A. G. Aranda. High-temperature structural evolution of $RNiO_3$ (R=Ho, Y, Er, Lu) perovskites: Charge disproportionation and electronic localization. *Phys. Rev. B*, 64(9):094102, 2001.

[9] J. A. Alonso, M. J. Martínez-Lope, M. T. Casais, J. L. Martínez, G. Demazeau, A. Largeteau, J. L. García-Muñoz, A. Muñoz, and M. T. Fernández-Díaz. High-pressure preparation, crystal structure,

magnetic properties, and phase transitions in $GdNiO_3$ and $DyNiO_3$ perovskites. *Chem. Mater.*, 11(9):2463–2469, 1999.

[10] J. A. Alonso, M. J. Martínez-Lope, I. A. Presniakov, A. V. Sobolev, V. S. Rusakov, A. M. Gapochka, G. Demazeau, and M. T. Fernández-Díaz. Charge disproportionation in $RNiO_3$ (R=Tm, Yb) perovskites observed in situ by neutron diffraction and ^{57}Fe probe Mössbauer spectroscopy. *Phys. Rev. B*, 87(18):184111, 2013.

[11] J. A. Alonso, M. J. Martínez-Lope, and I. Rasines. Preparation, crystal structure, and metal-to-insulator transition of $EuNiO_3$. *J. Solid State Chem.*, 120(1):170–174, 1995.

[12] K. Andres, J. E. Graebner, and H. R. Ott. $4f$-virtual-bound-state formation in $CeAl_3$ at low temperatures. *Phys. Rev. Lett.*, 35(26):1779–1782, 1975.

[13] E. R. Andrew, W. S. Hinshaw, and R. S. Tiffen. More precise determination of the Knight shift of aluminium. *Phys. Lett. A*, 46:57–58, 1973.

[14] V. I. Anisimov, J. Zaanen, and O. K. Andersen. Band theory and Mott insulators: Hubbard U instead of Stoner I. *Phys. Rev. B*, 44(3):943–954, 1991.

[15] Y. Bard. *Nonlinear Parameter Estimation.* Academic Press, 1974.

[16] T. Barth. Die Kristallstruktur von Perowskit und verwandten Verbindungen. *Norsk Geol. Tidssk.*, 8:201–216, 1925.

[17] J. G. Bednorz and K. A. Müller. Possible high T_c superconductivity in the Ba–La–Cu–O system. *Z. Phys. B*, 64(2):189–193, 1986.

[18] P. Blaha, K. Schwarz, G. K. H. Madsen, D. Kvasnicka, J. Luitz, R. Laskowski, F. Tran, and L. D. Marks. *WIEN2k, An Augmented Plane Wave + Local Orbitals Program for Calculating Crystal Properties.* Technische Universität Wien, 2018.

[19] B. Bleaney, K. D. Bowers, and M. H. L. Pryce. Paramagnetic resonance in diluted copper salts III. Theory, and evaluation of the nuclear electric quadrupole moments of ^{63}Cu and ^{65}Cu. *Proc. Royal Soc. Lond. A*, 228(1173):166–174, 1955.

[20] F. Bloch. Dynamical theory of nuclear induction. II. *Phys. Rev.*, 102(1):104–135, 1956.

[21] F. Bloch. Generalized theory of relaxation. *Phys. Rev.*, 105(4):1206–1222, 1957.

[22] P. W. Bridgman. The compressibility and pressure coefficient of resistance of ten elements. *Proc. Am. Acad. Arts Sci.*, 62(8):207, 1927.

[23] Bruker Corporation. *Almanac*, 2012.

[24] H. A. Buckmaster, R. Chatterjee, and Y. H. Shing. The application of tensor operators in the analysis of EPR and ENDOR spectra. *Physica Status Solidi A*, 13(1):9–50, 1972.

[25] G. Catalan. Progress in perovskite nickelate research. *Phase Transitions*, 81(7-8):729–749, 2008.

[26] S. Catalano, M. Gibert, J. Fowlie, J. Íñiguez, J. M. Triscone, and J. Kreisel. Rare-earth nickelates $RNiO_3$: thin films and heterostructures. *Rep. Prog. Phys.*, 81(4):046501, 2018.

[27] M. T. Causa, R. D. Sánchez, M. Tovar, J. A. Alonso, and M. J. Martínez-Lope. Charge disproportionation in $YNiO_3$: ESR and susceptibility study. *Phys. Rev. B*, 68(2):024429, 2003.

[28] S.-W. Cheong and M. Mostovoy. Multiferroics: a magnetic twist for ferroelectricity. *Nat. Mater.*, 6(1):13–20, 2007.

[29] A. M. Clogston and V. Jaccarino. Susceptibilities and negative Knight shifts of intermetallic compounds. *Phys. Rev.*, 121(5):1357–1362, 1961.

[30] P. Dalmas de Réotier and A. Yaouanc. Muon spin rotation and relaxation in magnetic materials. *J. Phys.: Condens. Matter*, 9(43):9113–9166, 1997.

[31] G. Demazeau, A. Marbeuf, M. Pouchard, and P. Hagenmuller. Sur une série de composés oxygènes du nickel trivalent derivés de la perovskite. *J. Solid State Chem.*, 3(4):582–589, 1971.

[32] R. Eguchi, A. Chainani, M. Taguchi, M. Matsunami, Y. Ishida, K. Horiba, Y. Senba, H. Ohashi, and S. Shin. Fermi surfaces, electron-hole asymmetry, and correlation kink in a three-dimensional Fermi liquid $LaNiO_3$. *Phys. Rev. B*, 79(11):115122, 2009.

[33] R. R. Ernst, G. Bodenhausen, and A. Wokaun. *Principles of Nuclear Magnetic Resonance in One and Two Dimensions*. Clarendon Press, paperback edition, 1990.

[34] E. Fermi. Über die magnetischen Momente der Atomkerne. *Z. Phys.*, 60(5-6):320–333, 1930.

[35] E. Fukushima and S. B. W. Roeder. *Experimental Pulse NMR: A Nuts and Bolts Approach*. Addison-Wesley Publishing Company, 1981.

[36] K. Fürsich, Y. Lu, D. Betto, M. Bluschke, J. Porras, E. Schierle, R. Ortiz, H. Suzuki, G. Cristiani, G. Logvenov, N. B. Brookes, M. W. Haverkort, M. L. Tacon, E. Benckiser, M. Minola, and B. Keimer. Resonant inelastic x-ray scattering study of bond order and spin excitations in nickelate thin-film structures. *Phys. Rev. B*, 99(16):165124, 2019.

[37] J. L. García-Muñoz, P. Lacorre, and R. Cywinski. Muon-spin-relaxation study of magnetic order in $RNiO_3$ (R=rare earth) below the metal–insulator transition. *Phys. Rev. B*, 51(21):15197–15202, 1995.

[38] J. L. García-Muñoz, R. Mortimer, A. Llobet, J. A. Alonso, M. J. Martínez-Lope, and S. P. Cottrell. μSR study of short-range charge order in $YNiO_3$ above the monoclinic–orthorhombic transition. *Physica B*, 374-375:87–90, 2006.

[39] J. L. García-Muñoz, J. Rodríguez-Carvajal, and P. Lacorre. Sudden appearance of an unusual spin density wave at the metal–insulator transition in the perovskites $RNiO_3$ (R = Pr, Nd). *Europhys. Lett.*, 20(3):241–247, 1992.

[40] J. L. García-Muñoz, J. Rodríguez-Carvajal, and P. Lacorre. Neutron-diffraction study of the magnetic ordering in the insulating regime of the perovskites $RNiO_3$ (R = Pr and Nd). *Phys. Rev. B*, 50(2):978–992, 1994.

[41] J. L. García-Muñoz, J. Rodríguez-Carvajal, P. Lacorre, and J. B. Torrance. Neutron-diffraction study of $RNiO_3$ (R=La, Pr, Nd, Sm): Electronically induced structural changes across the metal–insulator transition. *Phys. Rev. B*, 46(8):4414–4425, 1992.

[42] D. Gawryluk. Private communication.

[43] A. Georges, G. Kotliar, W. Krauth, and M. J. Rozenberg. Dynamical mean-field theory of strongly correlated fermion systems and the limit of infinite dimensions. *Rev. Mod. Phys.*, 68(1):13–125, 1996.

[44] G. Giovannetti, S. Kumar, D. Khomskii, S. Picozzi, and J. van den Brink. Multiferroicity in rare-earth nickelates $RNiO_3$. *Phys. Rev. Lett.*, 103(15):156401, 2009.

[45] A. M. Glazer. The classification of tilted octahedra in perovskites. *Acta Crystallogr. B*, 28(11):3384–3392, 1972.

[46] R. M. Golding and M. P. Halton. A theoretical study of the ^{14}N and ^{17}O N.M.R. shifts in lanthanide complexes. *Aust. J. Chem.*, 25(12):2577, 1972.

[47] V. M. Goldschmidt. Die Gesetze der Krystallochemie. *Die Naturwissenschaften*, 14(21):477–485, 1926.

[48] J. B. Goodenough and P. M. Raccah. Complex vs band formation in perovskite oxides. *J. Appl. Phys.*, 36(3):1031–1032, 1965.

[49] H. Guo, Z. W. Li, L. Zhao, Z. Hu, C. F. Chang, C.-Y. Kuo, W. Schmidt, A. Piovano, T. W. Pi, O. Sobolev, D. I. Khomskii, L. H. Tjeng, and A. C. Komarek. Antiferromagnetic correlations in the metallic strongly correlated transition metal oxide $LaNiO_3$. *Nat. Commun.*, 9(1):43, 2018.

[50] N. Hamada. Electronic band structure of $LaNiO_3$. *J. Phys. Chem. Solids*, 54(10):1157–1160, 1993.

[51] V. Heine. Hyperfine structure of paramagnetic ions. *Phys. Rev.*, 107(4):1002–1003, 1957.

[52] E. Holzschuh, A. B. Denison, W. Kündig, P. F. Meier, and B. D. Patterson. Muon-spin-rotation experiments in orthoferrites. *Phys. Rev. B*, 27(9):5294–5307, 1983.

[53] M. Horvatic. Magnetic nuclear spin-lattice relaxation in NMR of orthorhombic crystals in the presence of strong quadrupole coupling. *J. Phys.: Condens. Matter*, 4(26):5811–5824, 1992.

[54] F.-C. Hsu, J.-Y. Luo, K.-W. Yeh, T.-K. Chen, T.-W. Huang, P. M. Wu, Y.-C. Lee, Y.-L. Huang, Y.-Y. Chu, D.-C. Yan, and M.-K. Wu. Superconductivity in the PbO-type structure α-FeSe. *Proc. Natl. Acad. Sci. U.S.A.*, 105(38):14262–14264, 2008.

[55] T. C. Huang, W. Parrish, H. Toraya, P. Lacorre, and J. B. Torrance. High-temperature crystal structures of orthorhombic and rhombohedral $PrNiO_3$. *Mater. Res. Bull.*, 25(9):1091–1098, 1990.

[56] T. C. Huang, W. Parrish, J. B. Torrance, and P. Lacorre. Analysis of x-ray powder diffraction patterns of perovskite-like $PrNiO_3$. *Powder Diffr.*, 6(01):36–39, 1991.

[57] J. Hubbard. Electron correlations in narrow energy bands. *Proc. Royal Soc. Lond. A*, 276(1365):238–257, 1963.

[58] T. Imai, C. P. Slichter, A. P. Paulikas, and B. Veal. Measurement of the q-dependent static spin susceptibility $\chi'(q)$ in $YBa_2Cu_3O_{6.9}$. *Phys. Rev. B*, 47(14):9158–9161, 1993.

[59] J. D. Jackson. *Classical Electrodynamics*. Wiley, 3rd edition, 1999.

[60] H. A. Jahn and E. Teller. Stability of polyatomic molecules in degenerate electronic states I—Orbital degeneracy. *Proceedings of the Royal Society of London. Series A - Mathematical and Physical Sciences*, 161(905):220–235, 1937.

[61] F. James and M. Roos. Minuit — a system for function minimization and analysis of the parameter errors and correlations. *Comput. Phys. Commun.*, 10(6):343–367, 1975.

[62] R. Jaramillo, S. D. Ha, D. M. Silevitch, and S. Ramanathan. Origins of bad-metal conductivity and the insulator–metal transition in the rare-earth nickelates. *Nat. Phys.*, 10(4):304–307, 2014.

[63] Y. Kamihara, H. Hiramatsu, M. Hirano, R. Kawamura, H. Yanagi, T. Kamiya, and H. Hosono. Iron-based layered superconductor: LaOFeP. *J. Am. Chem. Soc.*, 128(31):10012–10013, 2006.

[64] Y. Kamihara, T. Watanabe, M. Hirano, and H. Hosono. Iron-based layered superconductor $La[O_{1-x}F_x]FeAs$ ($x = 0.05$–0.12) with $T_c = 26\,K$. *J. Am. Chem. Soc.*, 130(11):3296–3297, 2008.

[65] S.-J. Kim, G. Demazeau, J. A. Alonso, and J.-H. Choy. High pressure synthesis and crystal structure of a new Ni(III) perovskite: $TlNiO_3$. *J. Mater. Chem.*, 11(2):487–492, 2001.

[66] S. J. Kim, G. Demazeau, J. A. Alonso, A. Largeteau, J. M. Martinez-Lope, I. Presniakov, and J.-H. Choy. The Ni(III) perovskites: synthesis under high oxygen pressures and physico-chemical properties. *Solid State Commun.*, 117(2):113–115, 2000.

[67] S. J. Kim, G. Demazeau, and I. Presniakov. The stabilization of the highest oxidation states of transition metals under oxygen pressures: $TlNiO_3$, a new Ni(III) perovskite—comparison of the electronic properties with those of $TNiO_3$ (T = rare earth and Y). *J. Phys.: Condens. Matter*, 14(44):10741–10745, 2002.

[68] S. J. Kim, M. J. Martinez-Lope, M. T. Fernandez-Diaz, J. A. Alonso, I. Presniakov, and G. Demazeau. Evidence of Ni(III) disproportionation in the $TlNiO_3$ perovskite lattice through neutron powder diffraction and mössbauer spectroscopy. *Chem. Mater.*, 14(12):4926–4932, 2002.

[69] C. Kittel. *Introduction to Solid State Physics*. Wiley, 8th edition, 2005.

[70] W. D. Knight. Nuclear magnetic resonance shift in metals. *Phys. Rev.*, 76(8):1259–1260, 1949.

[71] L. Korosec. Development and testing of a new NMR spectrometer; first NMR studies on $RNiO_3$ perovskites. Master's thesis, ETH Zurich, 2014.

[72] L. Korosec, M. Pikulski, T. Shiroka, M. Medarde, H. Luetkens, J. A. Alonso, H. R. Ott, and J. Mesot. New magnetic phase in the nickelate perovskite $TlNiO_3$. *Phys. Rev. B*, 95(6):060411(R), 2017.

[73] J. Korringa. Nuclear magnetic relaxation and resonance line shift in metals. *Physica*, 16(7-8):601–610, 1950.

[74] G. Kotliar, S. Y. Savrasov, K. Haule, V. S. Oudovenko, O. Parcollet, and C. A. Marianetti. Electronic structure calculations with dynamical mean-field theory. *Rev. Mod. Phys.*, 78(3):865–951, 2006.

[75] H. Kramers. Théorie générale de la rotation paramagnétique dans les cristaux. *Proc. Amsterdam Acad.*, 33:959–972, 1930.

[76] G. Kresse and J. Furthmüller. Efficient iterative schemes for ab initio total-energy calculations using a plane-wave basis set. *Phys. Rev. B*, 54(16):11169–11186, 1996.

[77] R. Kubo. A stochastic theory of line-shape and relaxation. In D. T. Haar, editor, *Fluctuation, relaxation and resonance in magnetic systems*, Scottish Universities' Summer School 1961, pages 23–68. Oliver and Boyd, 1962.

[78] P. Lacorre, J. B. Torrance, J. Pannetier, A. I. Nazzal, P. W. Wang, and T. C. Huang. Synthesis, crystal structure, and properties of metallic $PrNiO_3$: Comparison with metallic $NdNiO_3$ and semiconducting $SmNiO_3$. *J. Solid State Chem.*, 91(2):225–237, 1991.

[79] S. Lee, R. Chen, and L. Balents. Landau theory of charge and spin ordering in the nickelates. *Phys. Rev. Lett.*, 106(1):016405, 2011.

[80] M. H. Levitt. The signs of frequencies and phases in NMR. *J. Magn. Reson.*, 126(2):164–182, 1997.

[81] M. H. Levitt. *Spin Dynamics: Basics of Nuclear Magnetic Resonance*. Wiley, 2nd edition, 2008.

[82] W. B. Lewis, J. A. Jackson, J. F. Lemons, and H. Taube. Oxygen-17 NMR shifts in aqueous solutions of rare-earth ions. *J. Chem. Phys.*, 36(3):694–701, 1962.

[83] S. Li, Y. Kobayashi, M. Itoh, D. Hirai, and H. Takagi. Metal-insulator transition and magnetic fluctuations in polycrystalline $Ru_{1-x}Rh_xP$ investigated by ^{31}P NMR. *Phys. Rev. B*, 95(15):155137, 2017.

[84] C. P. Lindsey and G. D. Patterson. Detailed comparison of the Williams–Watts and Cole–Davidson functions. *J. Chem. Phys.*, 73(7):3348–3357, 1980.

[85] Y. Lu, D. Betto, K. Fürsich, H. Suzuki, H.-H. Kim, G. Cristiani, G. Logvenov, N. Brookes, E. Benckiser, M. Haverkort, G. Khaliullin, M. L. Tacon, M. Minola, and B. Keimer. Site-selective probe of magnetic excitations in rare-earth nickelates using resonant inelastic x-ray scattering. *Phys. Rev. X*, 8(3):031014, 2018.

[86] M. W. Lufaso and P. M. Woodward. Prediction of the crystal structures of perovskites using the software program SPuDS. *Acta Crystallogr. B*, 57(6):725–738, 2001.

[87] I. I. Mazin, D. I. Khomskii, R. Lengsdorf, J. A. Alonso, W. G. Marshall, R. M. Ibberson, A. Podlesnyak, M. J. Martínez-Lope, and M. M. Abd-Elmeguid. Charge ordering as alternative to Jahn–Teller distortion. *Phys. Rev. Lett.*, 98(17):176406, 2007.

[88] H. M. McConnell and D. B. Chesnut. Theory of isotropic hyperfine interactions in π-electron radicals. *J. Chem. Phys.*, 28(1):107–117, 1958.

[89] M. Medarde, P. Lacorre, K. Conder, F. Fauth, and A. Furrer. Giant ^{16}O–^{18}O isotope effect on the metal-insulator transition of $RNiO_3$ perovskites (R=rare earth). *Phys. Rev. Lett.*, 80(11):2397–2400, 1998.

[90] M. L. Medarde. Structural, magnetic and electronic properties of $RNiO_3$ perovskites (R = rare earth). *J. Phys.: Condens. Matter*, 9(8):1679–1707, 1997.

[91] A. Mercy, J. Bieder, J. Íñiguez, and P. Ghosez. Structurally triggered metal-insulator transition in rare-earth nickelates. *Nat. Commun.*, 8(1):1677, 2017.

[92] S. Middey, J. Chakhalian, P. Mahadevan, J. W. Freeland, A. J. Millis, and D. D. Sarma. Physics of ultrathin films and heterostructures of rare-earth nickelates. *Annu. Rev. Mater. Res.*, 46(1):305–334, 2016.

[93] E. Mikheev, A. J. Hauser, B. Himmetoglu, N. E. Moreno, A. Janotti, C. G. V. de Walle, and S. Stemmer. Tuning bad metal and non-Fermi liquid behavior in a Mott material: Rare-earth nickelate thin films. *Science Advances*, 1(10):e1500797, 2015.

[94] M. Mitric, J. Blanusa, T. Barudzija, Z. Jaglicic, V. Kusigerski, and V. Spasojevic. Magnetic properties of trivalent Sm ions in $Sm_xY_{2-x}O_3$. *J. Alloys Compd.*, 485(1-2):473–477, 2009.

[95] T. Mizokawa, A. Fujimori, H. Namatame, K. Akeyama, and N. Kosugi. Electronic structure of the local-singlet insulator $NaCuO_2$. *Phys. Rev. B*, 49(11):7193–7204, 1994.

[96] T. Mizokawa, H. Namatame, A. Fujimori, K. Akeyama, H. Kondoh, H. Kuroda, and N. Kosugi. Origin of the band gap in the negative charge-transfer-energy compound $NaCuO_2$. *Phys. Rev. Lett.*, 67(12):1638–1641, 1991.

[97] K. Momma and F. Izumi. VESTA 3 for three-dimensional visualization of crystal, volumetric and morphology data. *J. Appl. Crystallogr.*, 44(6):1272–1276, 2011.

[98] E. W. Montroll and J. T. Bendler. On Lévy (or stable) distributions and the Williams-Watts model of dielectric relaxation. *J. Stat. Phys.*, 34(1-2):129–162, 1984.

[99] F. J. Morin. Oxides which show a metal–to–insulator transition at the Néel temperature. *Phys. Rev. Lett.*, 3(1):34–36, 1959.

[100] T. Moriya. Nuclear magnetic relaxation in antiferromagnetics. *Prog. Theor. Phys.*, 16(1):23–44, 1956.

[101] A. Muñoz, J. A. Alonso, M. J. Martínez-Lope, and M. T. Fernández-Díaz. On the magnetic structure of $DyNiO_3$. *J. Solid State Chem.*, 182(7):1982–1989, 2009.

[102] H. Niki, H. Okuda, Y. Okada, K. Higa, M. Oshiro, N. Fukuyoshi, R. Mahoe, M. Yogi, T. Nakama, K. Yagasaki, S. Ebisu, and S. Nagata. NMR studies of metal-insulator transition in the spinel-type $Cu(Ir_{1-x}V_x)_2S_4$. *J. Phys. Conf. Ser.*, 273:012139, 2011.

[103] H. Obayashi and T. Kudo. Some crystallographic, electric and thermochemical properties of the perovskite-type $La_{1-x}M_xNiO_3$(M: Ca, Sr and Ba). *Jpn. J. Appl. Phys.*, 14(3):330–335, 1975.

[104] H. Park, A. J. Millis, and C. A. Marianetti. Site-selective Mott transition in rare-earth-element nickelates. *Phys. Rev. Lett.*, 109(15):156402, 2012.

[105] A. Paul and T. Birol. Applications of DFT + DMFT in materials science. *Annu. Rev. Mater. Res.*, 49(1), 2019.

[106] O. Peil. Private communication.

[107] C. H. Pennington, D. J. Durand, C. P. Slichter, J. P. Rice, E. D. Bukowski, and D. M. Ginsberg. NMR measurement of the exchange coupling between Cu(2) atoms in $YBa_2Cu_3O_{7-\delta}$ ($T_c = 90K$). *Phys. Rev. B*, 39(1):274–277, 1989.

[108] J. P. Perdew, K. Burke, and M. Ernzerhof. Generalized gradient approximation made simple. *Phys. Rev. Lett.*, 77(18):3865–3868, 1996.

[109] J. P. Perdew, K. Burke, and M. Ernzerhof. Generalized gradient approximation made simple: Erratum. *Phys. Rev. Lett.*, 78(7):1396, 1997.

[110] J. Pérez-Cacho, J. Blasco, J. García, M. Castro, and J. Stankiewicz. Study of the phase transitions in $SmNiO_3$. *J. Phys.: Condens. Matter*, 11(2):405–415, 1999.

[111] F. A. Perras, C. M. Widdifield, and D. L. Bryce. QUEST—QUadrupolar Exact SofTware: A fast graphical program for the exact simulation of NMR and NQR spectra for quadrupolar nuclei. *Solid State Nucl. Magn. Reson.*, 45-46:36–44, 2012.

[112] J. C. Phillips. Stretched exponential relaxation in molecular and electronic glasses. *Rep. Prog. Phys.*, 59(9):1133–1207, 1996.

[113] M. Pikulski. *Powder-averaging using MATLAB*, 2015. Internal communication.

[114] M. Pikulski. *Field-induced chirality in a frustrated quantum spin ladder.* PhD thesis, ETH Zurich, 2017.

[115] M. Pikulski, T. Shiroka, F. Casola, A. P. Reyes, P. L. Kuhns, S. Wang, H. R. Ott, and J. Mesot. Two coupled chains are simpler than one: Field-induced chirality in a frustrated quantum spin ladder. Submitted to npj Quantum Materials.

[116] K. W. Post, A. S. McLeod, M. Hepting, M. Bluschke, Y. Wang, G. Cristiani, G. Logvenov, A. Charnukha, G. X. Ni, P. Radhakrishnan, M. Minola, A. Pasupathy, A. V. Boris, E. Benckiser, K. A. Dahmen, E. W. Carlson, B. Keimer, and D. N. Basov. Coexisting first- and second-order electronic phase transitions in a correlated oxide. *Nat. Phys.*, 2018.

[117] J. D. Rall, M. S. Seehra, N. Shah, and G. P. Huffman. Comparison of the nature of magnetism in α-$Ni(OH)_2$ and β-$Ni(OH)_2$. *J. Appl. Phys.*, 107(9):09B511, 2010.

[118] A. G. Redfield. On the theory of relaxation processes. *IBM Journal of Research and Development*, 1(1):19–31, 1957.

[119] J. Rodríguez-Carvajal, S. Rosenkranz, M. Medarde, P. Lacorre, M. T. Fernandez-Díaz, F. Fauth, and V. Trounov. Neutron-diffraction study of the magnetic and orbital ordering in $^{154}SmNiO_3$ and $^{153}EuNiO_3$. *Phys. Rev. B*, 57(1):456–464, 1998.

[120] S. Rosenkranz. *Neutronendiffraktion und Neutronenspektroskopie an Seltenen Erd-Nickelaten $RNiO_3$ (R = Seltene Erde).* PhD thesis, ETH Zürich, 1996.

[121] S. Rosenkranz, M. Medarde, F. Fauth, J. Mesot, M. Zolliker, A. Furrer, U. Staub, P. Lacorre, R. Osborn, R. S. Eccleston, and V. Trounov. Crystalline electric field of the rare-earth nickelates $RNiO_3$ (R = Pr, Nd, Sm, Eu, and $Pr_{1-x}La_x$, $0 \leq x \leq 0.7$) determined by inelastic neutron scattering. *Phys. Rev. B*, 60(21):14857–14867, 1999.

[122] S. Rosenkranz, U. Staub, A. Furrer, R. Osborn, P. Lacorre, and V. Trounov. Intermultiplet crystal field transitions in $EuNiO_3$. *J. Alloys Compd.*, 250(1-2):577–580, 1997.

[123] M. Rotter, M. Tegel, and D. Johrendt. Superconductivity at 38 K in the iron arsenide $(Ba_{1-x}K_x)Fe_2As_2$. *Phys. Rev. Lett.*, 101(10):107006, 2008.

[124] A. Sakai, G. Zheng, and Y. Kitaoka. Strongly correlated metallic state of $LaNiO_3$: ^{139}La NMR study. *J. Phys. Soc. Jpn.*, 71(Suppl):166–168, 2002.

[125] J. J. Sakurai. *Modern Quantum Mechanics.* Pearson, revised edition, 1994.

[126] D. Schildknecht. Semester thesis: Nickelates. Semester thesis, ETH Zürich, 2015.

[127] G. K. Semin and A. M. Raevskii. Nuclear quadrupole and hexadecapole interactions in crystals of lutetium compounds. *JETP Lett.*, 44(10):593, 1986.

[128] C. P. Slichter. *Principles of Magnetic Resonance.* Springer Series in Solid-State Sciences. Springer, 3rd edition, 1990.

[129] K. Sreedhar, J. M. Honig, M. Darwin, M. McElfresh, P. M. Shand, J. Xu, B. C. Crooker, and J. Spalek. Electronic properties of the metallic perovskite $LaNiO_3$: Correlated behavior of $3d$ electrons. *Phys. Rev. B*, 46(10):6382–6386, 1992.

[130] U. Staub, M. García-Fernández, A. M. Mulders, Y. Bodenthin, M. J. Martínez-Lope, and J. A. Alonso. Soft x-ray resonant magnetic powder diffraction on $PrNiO_3$. *J. Phys.: Condens. Matter*, 19(9):092201, 2007.

[131] F. Steglich, J. Aarts, C. D. Bredl, W. Lieke, D. Meschede, W. Franz, and H. Schäfer. Superconductivity in the presence of strong Pauli paramagnetism: $CeCu_2Si_2$. *Phys. Rev. Lett.*, 43(25):1892–1896, 1979.

[132] R. Sternheimer. On nuclear quadrupole moments. *Phys. Rev.*, 84(2):244–253, 1951.

[133] R. M. Sternheimer. Quadrupole antishielding factors of ions. *Phys. Rev.*, 132(4):1637–1639, 1963.

[134] R. M. Sternheimer. Shielding and antishielding effects for various ions and atomic systems. *Phys. Rev.*, 146(1):140–160, 1966.

[135] A. Subedi, O. E. Peil, and A. Georges. Low-energy description of the metal-insulator transition in the rare-earth nickelates. *Phys. Rev. B*, 91(7):075128, 2015.

[136] A. Suter, M. Mali, J. Roos, and D. Brinkmann. Mixed magnetic and quadrupolar relaxation in the presence of a dominant static Zeeman hamiltonian. *J. Phys.: Condens. Matter*, 10(26):5977–5994, 1998.

[137] S. Vasala and M. Karppinen. $A_2B'B''O_6$ perovskites: A review. *Prog. Solid State Chem.*, 43(1-2):1–36, 2015.

[138] R. E. Walstedt. *The NMR Probe of High-Tc Materials*. Springer-Verlag GmbH Germany, 2nd edition, 2018.

[139] B.-X. Wang, S. Rosenkranz, X. Rui, J. Zhang, F. Ye, H. Zheng, R. F. Klie, J. F. Mitchell, and D. Phelan. Antiferromagnetic defect structure in $LaNiO_{3-\delta}$ single crystals. *Phys. Rev. Mater.*, 2(6):064404, 2018.

[140] R. K. Wangsness and F. Bloch. The dynamical theory of nuclear induction. *Phys. Rev.*, 89(4):728–739, 1953.

[141] M. Weller. *NMR/NQR studies at very low temperatures and high pressures in strongly correlated electron systems*. PhD thesis, ETH Zurich, 2007.

[142] A. Wold, B. Post, and E. Banks. Rare earth nickel oxides. *J. Am. Chem. Soc.*, 79(18):4911–4913, 1957.

[143] Y. Yamada and A. Sakata. An analysis method of antiferromagnetic powder patterns in spin-echo NMR under external fields. *J. Phys. Soc. Jpn.*, 55(5):1751–1758, 1986.

[144] S. Yamamoto and T. Fujiwara. Charge and spin order in $RNiO_3$(R=Nd, Y) by LSDA+U method. *J. Phys. Soc. Jpn.*, 71(5):1226–1229, 2002.

[145] S. Yang, J. Shore, and E. Oldfield. Oxygen-17 nuclear magnetic resonance spectroscopic study of the lanthanide oxides. *J. Magn. Reson.*, 99(2):408–412, 1992.

[146] A. Yaouanc and P. Dalmas de Réotier. *Muon Spin Rotation, Relaxation, and Resonance*. Oxford University Press, New York, 2011.

[147] J. Zaanen, G. A. Sawatzky, and J. W. Allen. Band gaps and electronic structure of transition-metal compounds. *Phys. Rev. Lett.*, 55(4):418–421, 1985.

[148] J. Zhang, H. Zheng, Y. Ren, and J. F. Mitchell. High-pressure floating-zone growth of perovskite nickelate $LaNiO_3$ single crystals. *Cryst. Growth Des.*, 17(5):2730–2735, 2017.

[149] J.-S. Zhou and J. B. Goodenough. Universal octahedral-site distortion in orthorhombic perovskite oxides. *Phys. Rev. Lett.*, 94(6):065501, 2005.

[150] J.-S. Zhou, J. B. Goodenough, and B. Dabrowski. Pressure-induced non-fermi-liquid behavior of $PrNiO_3$. *Phys. Rev. Lett.*, 94(22):226602, 2005.

[151] J.-S. Zhou, L. G. Marshall, and J. B. Goodenough. Mass enhancement versus Stoner enhancement in strongly correlated metallic perovskites: $LaNiO_3$ and $LaCuO_3$. *Phys. Rev. B*, 89(24):245138, 2014.